

The Pennsylvania State University  
The Graduate School

DEVELOPMENT AND EVALUATION OF A SHORTWAVE  
FULL-SPECTRUM CORRELATED *K*-DISTRIBUTION  
RADIATIVE TRANSFER ALGORITHM FOR  
NUMERICAL WEATHER PREDICTION

A Thesis in  
Meteorology  
by  
Daniel T. Pawlak

© 2004 Daniel T. Pawlak

Submitted in Partial Fulfillment  
of the Requirements  
for the Degree of

Doctor of Philosophy

December 2004

# Report Documentation Page

*Form Approved  
OMB No. 0704-0188*

Public reporting burden for the collection of information is estimated to average 1 hour per response, including the time for reviewing instructions, searching existing data sources, gathering and maintaining the data needed, and completing and reviewing the collection of information. Send comments regarding this burden estimate or any other aspect of this collection of information, including suggestions for reducing this burden, to Washington Headquarters Services, Directorate for Information Operations and Reports, 1215 Jefferson Davis Highway, Suite 1204, Arlington VA 22202-4302. Respondents should be aware that notwithstanding any other provision of law, no person shall be subject to a penalty for failing to comply with a collection of information if it does not display a currently valid OMB control number.

1. REPORT DATE <b>00 DEC 2004</b>	2. REPORT TYPE <b>N/A</b>	3. DATES COVERED <b>-</b>	
4. TITLE AND SUBTITLE <b>Development And Evaluation Of A Shortwave Full-Spectrum Correlated K-Distribution Radiative Transfer Algorithm For Numerical Weather Prediction</b>		5a. CONTRACT NUMBER	
		5b. GRANT NUMBER	
		5c. PROGRAM ELEMENT NUMBER	
6. AUTHOR(S)		5d. PROJECT NUMBER	
		5e. TASK NUMBER	
		5f. WORK UNIT NUMBER	
7. PERFORMING ORGANIZATION NAME(S) AND ADDRESS(ES) <b>The Pennsylvania State University</b>		8. PERFORMING ORGANIZATION REPORT NUMBER	
9. SPONSORING/MONITORING AGENCY NAME(S) AND ADDRESS(ES)		10. SPONSOR/MONITOR'S ACRONYM(S)	
		11. SPONSOR/MONITOR'S REPORT NUMBER(S)	
12. DISTRIBUTION/AVAILABILITY STATEMENT <b>Approved for public release, distribution unlimited</b>			
13. SUPPLEMENTARY NOTES <b>The original document contains color images.</b>			
14. ABSTRACT			
15. SUBJECT TERMS			
16. SECURITY CLASSIFICATION OF:			17. LIMITATION OF ABSTRACT
a. REPORT <b>unclassified</b>	b. ABSTRACT <b>unclassified</b>	c. THIS PAGE <b>unclassified</b>	<b>UU</b>
			18. NUMBER OF PAGES <b>151</b>
			19a. NAME OF RESPONSIBLE PERSON

The thesis of Daniel T. Pawlak was reviewed and approved\* by the following:

Eugene E. Clothiaux  
Assistant Professor of Meteorology  
Thesis Advisor, Chair of Committee

David R. Stauffer  
Associate Professor of Meteorology

Jerry Y. Harrington  
Assistant Professor of Meteorology

Michael F. Modest  
Professor of Mechanical Engineering

William H. Brune  
Professor of Meteorology  
Head of the Department of Meteorology

\*Signatures are on file in the Graduate School.

# Abstract

The Full Spectrum Correlated  $k$ -distribution (FSCK) method, originally developed for applications in combustion systems, is adapted for use in shortwave atmospheric radiative transfer. By weighting  $k$ -distributions by the solar source function, the FSCK method eliminates the requirement that the Planck function be constant over a spectral interval. Consequently, integration may be carried out across the full spectrum as long as the assumption of correlation from one atmospheric level to the next remains valid. Errors resulting from the lack of correlation across the full spectrum are removed by partitioning the spectrum at a wavelength of  $0.68\ \mu\text{m}$  into two bands. The resulting two-band approach in the FSCK formalism requires only 15 quadrature points per atmospheric layer. This represents a 40–90% reduction in computation time relative to existing correlated  $k$ -distribution models.

The two-band FSCK approach is developed for general atmospheric conditions through the use of tabulated gas  $k$ -values, with nongray cloud absorption coefficients added on-the-fly. A two-part evaluation of the FSCK calculations is pre-

sented. First, the two-band FSCK results are compared with line-by-line (LBL) benchmarks alongside results from an earlier radiative transfer model intercomparison study. The median of 24 1-D models included in the intercomparison has a clear-sky mean bias error of  $-0.27$  K/day relative to LBL benchmark heating rates, while the operational FSCK model has a mean bias error of  $+0.04$  K/day. In a second set of calculations, two-band FSCK results are compared with those from six popular state-of-the-art operational and research radiative transfer models. The clear-sky RMS heating rate errors for three empirically-based models range from  $0.78$  to  $6.28$  K/day, while RMS errors for three correlated  $k$ -distribution models range from  $0.85$  to  $2.83$  K/day. For the same clear-sky case the FSCK RMS error is  $0.57$  K/day. Cloudy-sky cases show that the correlated  $k$ -distribution models overestimate in-cloud heating, while the FSCK approach with nongray cloud absorption is closer to the benchmark.

# Table of Contents

<b>List of Figures</b>	<b>vii</b>
<b>List of Tables</b>	<b>x</b>
<b>Acknowledgments</b>	<b>xi</b>
<b>1 Introduction</b>	<b>1</b>
1.1 A General Description of Radiative Transfer Models . . . . .	1
1.2 Motivation to Develop a New Shortwave Spectroscopic Model . . . . .	5
1.3 Outline of this Work . . . . .	8
<b>2 The FSCK Algorithm</b>	<b>11</b>
2.1 Model Background . . . . .	11
2.1.1 Correlated $k$ -distributions . . . . .	12
2.1.2 Full-Spectrum Correlated $k$ -distributions for Longwave Radiative Transfer . . . . .	14
2.1.3 Full-Spectrum Correlated $k$ -distributions for Shortwave Radiative Transfer . . . . .	21
2.1.4 Sorting . . . . .	26
2.2 Fixed Atmosphere Case Studies . . . . .	28
2.2.1 Case Study Atmospheres, Gases, and Clouds . . . . .	28
2.2.2 Clear-Sky Calculations . . . . .	33
2.2.3 Cloudy Sky Calculations . . . . .	38
2.2.4 Case Study Observations . . . . .	45
<b>3 Model Development for General Atmospheres</b>	<b>48</b>
3.1 Design Considerations . . . . .	48
3.2 Precombined Gases with Gray Cloud Absorption . . . . .	52

3.3	Gases Combined On-the-Fly with Nongray Cloud Absorption . . . .	60
3.3.1	Constituents Combined Simultaneously . . . . .	63
3.3.2	Constituents Combined Serially . . . . .	69
3.4	The Way Forward . . . . .	71
<b>4</b>	<b>Evaluation versus Operational and Research Models</b>	<b>76</b>
4.1	Comparison to ICRCM-III Models . . . . .	78
4.2	State-of-the-Art Operational and Research Models . . . . .	88
4.2.1	Dudhia Shortwave Scheme . . . . .	91
4.2.2	GFDL-Eta Scheme . . . . .	93
4.2.3	CAM2 and CAM3 Schemes . . . . .	97
4.2.4	Fu and Liou Scheme . . . . .	100
4.2.5	Kato Scheme . . . . .	102
4.2.6	RRTM SW Scheme . . . . .	102
4.3	Comparison to State-of-the-Art Operational and Research Models .	105
<b>5</b>	<b>Discussion</b>	<b>120</b>
5.1	Summary and Conclusions . . . . .	120
5.2	Future Work . . . . .	130
	<b>Bibliography</b>	<b>134</b>

# List of Figures

2.1	Absorption and scattering coefficients for liquid cloud drops. . . . .	15
2.2	Combined absorption coefficients of water vapor, carbon dioxide, ozone, nitrous oxide, carbon monoxide, methane, and oxygen, with and without cloud absorption. . . . .	25
2.3	Solar Source Function (SSF), combined absorption coefficients of water vapor, carbon dioxide, ozone, nitrous oxide, carbon monoxide, methane, and oxygen, SSF-weighted $k$ -distribution, and SSF-weighted cumulative $k$ -distribution. . . . .	27
2.4	Gas mixing ratio and temperature profiles for the mid-latitude winter atmosphere of McClatchey et al. (1972). . . . .	30
2.5	Gas mixing ratio and temperature profiles for the subarctic winter atmosphere of McClatchey et al. (1972). . . . .	31
2.6	Gas mixing ratio and temperature profiles for the tropical atmosphere of McClatchey et al. (1972). . . . .	32
2.7	Upward and downward fluxes, heating rates for all 29 layers, and heating rates for the lowest 14 layers for the full shortwave spectrum treated as a single band, band 1, band 2, and the full shortwave spectrum treated by adding bands 1 and 2 for the LBL solution, the 8192 quadrature point solution, and the 15 quadrature point solution. . . . .	34
2.8	Upward and downward fluxes, heating rates for all 29 layers, and heating rates for the lowest 14 layers for clear sky, a liquid cloud with nongray absorption and gray scattering, an ice cloud with nongray absorption and gray scattering, and both clouds with nongray absorption and gray scattering for the LBL solution, the 8192 quadrature point solution, and the 15 quadrature point solution. . . . .	39

2.9	Upward and downward fluxes, heating rates for all 29 layers, and heating rates for the lowest 14 layers for a liquid cloud with gray absorption and gray scattering, an ice cloud with gray absorption and gray scattering, and both clouds with gray absorption and gray scattering for the LBL solution, the 8192 quadrature point solution, and the 15 quadrature point solution. . . . .	43
3.1	Broadband heating rates for the FSCK 15-point hardwired solution and FSCK calculations using precombined gases with gray cloud absorption for the CLEAR, CLOUD A, and CLOUD B cases of Barker et al. (2003). . . . .	59
3.2	Broadband heating rates for the FSCK 15-point hardwired solution and FSCK calculations using gases and nongray cloud absorption combined on-the-fly simultaneously for the CLEAR, CLOUD A, and CLOUD B cases of Barker et al. (2003). . . . .	68
3.3	Broadband heating rates for the FSCK 15-point hardwired solution and FSCK calculations using gases and nongray cloud absorption combined on-the-fly serially for the CLEAR, CLOUD A, and CLOUD B cases of Barker et al. (2003). . . . .	71
3.4	Near infrared (wavelengths 1.0 $\mu\text{m}$ and 3.0 $\mu\text{m}$ ) absorption optical depths for a lognormal distribution of liquid-water cloud drops with effective radius of 10 $\mu\text{m}$ as a function of cloud-drop number concentration. Broadband near infrared transmission for a non-scattering layer consisting of a clear-sky gas mixture, a lognormal distribution of liquid-water cloud drops with effective radius of 10 $\mu\text{m}$ , a mixed gas-cloud layer, and the product of the gas-mixture and cloud broadband transmissions as a function of cloud-drop number concentration. The percent error of the product of the clear-sky gas mixture and cloud broadband transmissions relative to the broadband transmission for the mixed gas-cloud layer as a function of cloud-drop number concentration. . . . .	74
3.5	Broadband heating rates for the FSCK 15-point hardwired solution and FSCK calculations using precombined gases with nongray cloud absorption combined on-the-fly serially for the CLEAR, CLOUD A, and CLOUD B cases of Barker et al. (2003). . . . .	75

4.1	Top-of-atmosphere albedo, surface absorptance, atmospheric absorptance, and heating rate profiles for the CLEAR case as a function of cosine of solar zenith angle $\mu_0$ . ICRCCM-III 1-D model median values, and upper and lower quartiles are plotted vs. $\mu_0$ . LBL calculations and FSCK calculations are plotted for $\mu_0=0.5$ . . .	81
4.2	Top-of-atmosphere albedo, surface absorptance, atmospheric absorptance, and heating rate profiles for the CLOUD A case as a function of cosine of solar zenith angle $\mu_0$ . ICRCCM-III 1-D model median values, and upper and lower quartiles are plotted vs. $\mu_0$ . LBL calculations and FSCK calculations are plotted for $\mu_0=0.5$ . . .	84
4.3	Top-of-atmosphere albedo, surface absorptance, atmospheric absorptance, and heating rate profiles for the CLOUD B case as a function of cosine of solar zenith angle $\mu_0$ . ICRCCM-III 1-D model median values, and upper and lower quartiles are plotted vs. $\mu_0$ . LBL calculations and FSCK calculations are plotted for $\mu_0=0.5$ . . .	85
4.4	Schematic diagram of spectral bands for six popular operational and research shortwave radiative transfer models and the FSCK model. Diagonal lines indicate spectral regions not included by the model. .	90
4.5	Broadband heating rates calculated by LBL, the FSCK approach, the Dudhia scheme, the GFDL-Eta scheme, the CAM3 scheme, the Fu and Liou scheme, the Kato scheme, and the RRTM SW scheme, for the CLEAR case of Barker et al. (2003). . . . .	106
4.6	Percent error in model downward flux absorbed at the surface relative to LBL calculations ( $483.72 \text{ Wm}^{-2}$ ). . . . .	108
4.7	Processing time in seconds on a single 1.7 GHz processor for 100,000 iterative model calculations without inputs and outputs to hard disk. The time spent on creating the optical properties is represented by the lightly shaded region, while the time spent on the solver is the darkly shaded region. . . . .	109
4.8	Broadband heating rates calculated by LBL, the FSCK approach, the Dudhia scheme, the CAM3 scheme, the Fu and Liou scheme, the Kato scheme, and the RRTM SW scheme, for the CLOUD A case and the CLOUD B case of Barker et al. (2003). . . . .	114
4.9	Broadband heating rates for LBL calculations, the FSCK 8192-point hardwired solution, the FSCK 15-point hardwired solution, the FSCK solution from the current implementation, and the CAM3 scheme solution, for the CLEAR case of Barker et al. (2003). . . . .	117

# List of Tables

2.1	Trapezoidal quadrature abscissas and weights for band 1 and shifted Gauss-Chebyshev II quadrature abscissas and weights for band 2 before and after transformation. . . . .	37
2.2	Asymmetry parameters, single-scattering albedos, and extinction cross sections, for a lognormal distribution of liquid water spheres of radius $5 \mu\text{m}$ and ice spheres of radius $75 \mu\text{m}$ for band 1 and band 2, nongray absorption and gray scattering, and gray absorption and gray scattering. . . . .	41
3.1	Atmospheric state variables, combinations of which are used to calculate tabulated $k$ -values. Also shown are effective radii of a lognormal distribution of liquid- and ice-cloud drops used to calculate gray cloud scattering properties and gray or nongray cloud absorption.	55

# Acknowledgments

This work was supported by the Department of Energy Atmospheric Radiation Measurement program (under grant DE-FG02-90ER61071) and the Air Force Institute of Technology Civilian Institutions program. The views expressed in this thesis are those of the author and do not reflect the official policy or position of the United States Air Force, Department of Defense, or the U.S. Government. I would like to thank Anthony Clough, Eli Mlawer, and Jennifer Delamere for their support and comments as I used their monochromatic radiative transfer code LBLRTM, and Seiji Kato and Howard Barker for many discussions on correlated  $k$ -distribution issues in atmospheric science research. I thank Anquan Wang for his assistance with the quadrature and combination schemes, Frank Evans and Sally McFarlane for help with the RRTM and Fu and Liou codes, Jimy Dudhia for assistance with his shortwave model, Bill Briegleb and William Collins for details of the CAM2 and CAM3 schemes, and Yu-Tai Hou, Tom Black, and Kenneth Campana for information regarding the GFDL-Eta model. I would also like to thank the following class participants in the Pennsylvania State University seminar METEO

597A for compiling the profiles of atmospheric gases used in Figs. 2.4-2.6: Matt Boehm, Jason Cole, Brian Etherton, Laura Hinkleman, Urszula Jambor, Mike Jensen, Ricardo Munoz, Chuck Pavloski, and Manajit Sengupta. I also thank Dave Stauffer, Ken Davis, and Jerry Harrington for their helpful comments and suggestions. I am deeply grateful to Michael Modest, Eugene Clothiaux, and Jason Cole, for consistently helping me through this work. Finally, I thank my family for the support they have given me throughout my studies.

# Chapter 1

## Introduction

### 1.1 A General Description of Radiative Transfer

#### Models

The sun is the external source of energy that drives atmospheric motions. As solar-emitted energy encounters the Earth atmosphere, some of the energy is absorbed by atmospheric gases, some is absorbed by cloud-liquid, cloud-ice, or aerosol particles, some is absorbed by the Earth surface, and the rest is scattered back into space.

If we want Numerical Weather Prediction (NWP) models or General Circulation Models (GCMs) to predict accurately a thunderstorm this afternoon, a drought next summer, or the average surface temperature 100 years from now, these models must accurately account for the heating that results from absorption of solar energy by gases, clouds, aerosols, and the surface. The models must

also accurately represent the spatial and temporal distribution of the heating in the atmosphere and on the surface. To calculate heating due to absorption of solar energy and the spatial and temporal distribution of that heating, NWP models and GCMs use radiative transfer parameterizations which have two essential components: a solver and a spectroscopic model.

A solver, as its name implies, numerically solves the radiative transfer equation. Within a NWP model or GCM the continuous vertical structure of the atmosphere is typically approximated by discrete layers, and the horizontal domain is subdivided into discrete columns. There are a variety of approaches to solving the radiative transfer equation, so, naturally, there are a variety of solvers available for use in radiative transfer parameterizations with varying degrees of complexity and accuracy. In general, a solver for solar energy entering the Earth atmosphere attenuates, layer-by-layer, the incoming solar energy in a wavelength-dependent manner. Attenuation occurs as the result of either absorption of energy in a layer or scattering of energy to a different vertical layer. In a three-dimensional solver one can also have scattering that produces horizontal transport of radiation into, or through, neighboring model columns. To determine the amount of absorption and scattering in a layer, as well as the directionality of the scattering, the solver requires optical properties for the constituents in each atmospheric layer.

A spectroscopic model provides optical properties for the solver for each layer based on NWP model- or GCM-calculated pressure and temperature, as well as

gas, aerosol-, and cloud-particle concentrations for each layer. The solver requires absorption and scattering properties, including the directional dependence of scattering, for each constituent in each atmospheric layer.

Gases in the atmosphere of Earth have absorption coefficients that vary rapidly as a function of wavelength,  $\lambda$ , changing by several orders of magnitude across the electromagnetic spectrum. As a result, the most accurate way to perform broadband radiative transfer calculations is to divide the full spectrum into nearly monochromatic wavelength intervals ( $\delta\lambda \approx 10^{-8}$ – $10^{-6}$   $\mu\text{m}$ ) and to calculate atmospheric fluxes and heating rates for each of these intervals. Integrating the results over all intervals across the spectrum leads to broadband fluxes and heating rates. This approach is called line-by-line (LBL) radiative transfer. Because of the strong variability of the gas absorption coefficients across the spectrum, the LBL approach requires millions of calculations to obtain a solution for the full shortwave, or long-wave, spectrum, which makes this method impractical for use in NWP models or GCMs.

For over twenty years the  $k$ -distribution technique has been used successfully as a close approximation to integrated broadband LBL calculations (e.g., Goody and Yung 1989; Lacis and Oinas 1991; Fu and Liou 1992). In the  $k$ -distribution technique, gas absorption coefficients,  $k$ , across a portion of the spectrum are sorted in magnitude to create a  $k$ -distribution function. The  $k$ -distribution is then transformed into a cumulative  $k$ -distribution,  $g$ , which is a smooth monotonic

function representing an equivalent nondimensional wavelength. Both the  $k$ - and cumulative  $k$ -distributions contain essentially the same information for integrated radiative transfer calculations as the rapidly varying absorption coefficients versus wavelength (e.g., Liou 2002) because the integration is independent of the ordering of the absorption coefficients. However, instead of requiring hundreds of thousands of calculations to cover the relevant portion of the spectrum in flux and heating rate calculations, the cumulative  $k$ -distribution can be integrated with only a few quadrature points because of its smoothness.

The  $k$ -distribution method is exact for absorbing non- and gray-scattering homogeneous atmospheric layers as long as internal and external emission is approximately constant over the spectral region for which the  $k$ -distribution is constructed. To account for the vertical inhomogeneity of the atmosphere, in the *correlated*  $k$ -distribution method it is assumed that the absorption coefficients at different pressures and temperatures are correlated (e.g., Liou 2002). Essentially, this means that the absorption coefficient in a spectral interval,  $\delta\lambda$ , at one atmospheric level has the same relative position in the cumulative  $k$ -distribution as the absorption coefficients in that spectral interval at every other level, ensuring that the relative sorting of absorption coefficients from  $\lambda$ -space to  $g$ -space is consistent from level to level. Conditions that cause the relative sorting to change between atmospheric levels result in a breakdown of correlation and introduce error into the integration in  $g$ -space.

A limitation of the correlated  $k$ -distribution technique is that the source function, i.e., the Planck function for internal emission or the solar source function for external emission, must be nearly constant over the spectral interval of interest (e.g., Goody and Yung 1989). Although the Planck function varies smoothly, it covers a range of several orders of magnitude across the solar spectrum. Thus, in broadband radiative transfer calculations, cumulative  $k$ -distributions are typically constructed for a number of spectral bands ( $\Delta\lambda \approx 10^{-2}$ – $10^0 \mu\text{m}$ ) over which the Planck function or solar source function may be assumed to be approximately constant (e.g., Fu and Liou 1992; Mlawer and Clough 1997; Mlawer and Clough 1998; Kato et al. 1999). Since integration of each cumulative  $k$ -distribution requires a few quadrature points, integration of the full spectrum requires about 40–150 quadrature points per layer depending on the particular model (e.g., Fu and Liou 1992; Mlawer and Clough 1997; Mlawer and Clough 1998; Kato et al. 1999), which is still a considerable computational savings over LBL calculations.

## **1.2 Motivation to Develop a New Shortwave Spectroscopic Model**

Even considering the computational efficiency of the correlated  $k$ -distribution technique, 40–150 radiation calculations is too computationally expensive for NWP models and GCMs. That is, even as few as 40–150 radiation calculations in NWP

models and GCMs require substantial computational time relative to all other physical and dynamical calculations. As a result, radiation subroutines in operational models are usually invoked less often than the timescale on which cloud dynamics and microphysics evolve in the models. If the number of calculations could be further reduced without sacrificing accuracy, the savings in computational time could be used in both GCMs and NWP models to call the radiation subroutines on a timescale that would allow a more realistic interaction between radiation and clouds. In current model practices, computationally fast scaled  $k$ -distributions or empirical formulations are used in the radiation parameterization, generally at the expense of accuracy.

In contrast to the correlated  $k$ -distribution approach, in a scaled  $k$ -distribution approach a cumulative  $k$ -distribution is constructed for a single reference level. Absorption coefficients for other levels are derived simply by scaling the quadrature values of the reference cumulative  $k$ -distribution as a function of pressure, temperature, and absorber amount. In addition to scaled  $k$ -distribution schemes there are also a variety of empirical methods, ranging from gray absorption parameters tuned to narrow-band LBL calculations, to empirical methods that create functions that behave like  $k$ -distributions through exponential sum fitting. Each of these methods are intended to provide accuracy, while reducing computational cost as much as possible.

The problem of computational efficiency of radiative transfer calculations is

not restricted to atmospheric applications. The Full Spectrum Correlated  $k$ -Distribution (FSCK) method was developed to address the problem of radiative heat transfer for combustion systems (Modest and Zhang 2002; Modest 2003). The FSCK method eliminates the need for a constant source function across each spectral region to be considered in a radiative transfer calculation. In the FSCK method the cumulative  $k$ -distribution,  $g$ , is no longer equivalent to a non-dimensional wavelength. Instead, by weighting the  $k$ -distribution by the source function,  $g$  becomes equivalent to a fractional source function. This modification permits sorting of  $k$ -coefficients across bands as large as the full spectrum as long as the condition of correlation between vertical atmospheric levels is still met. By eliminating the necessity for multiple spectral bands, the total number of calculations can be reduced substantially without losing significant accuracy relative to broadband LBL calculations.

In the case of a purely external source of radiation, such as solar radiation interacting with the atmosphere of Earth, the method is simplified because the only emission is at the top boundary. However, the sun does not radiate precisely as a blackbody; that is, the radiation from the sun interacting with the Earth atmosphere is not precisely represented by a Planck function evaluated at the effective surface temperature of the sun. Since estimates of solar irradiance are available (Kurucz 1992), the solar source function can be used as a weighting function for the  $k$ -distribution rather than the Planck function. Because traditional

$k$ -distribution models assume a constant Planck function over each spectral interval to be integrated, by explicitly accounting for the spectral variability of the solar source function the FSCK method has the potential to improve the accuracy of calculations as well.

### 1.3 Outline of this Work

In Chapter 2 we develop the FSCK method for atmospheric applications and simplify the equations for the solar radiation case. We present a series of standard nonhomogeneous atmospheres, which are the basis for the initial tests of the FSCK algorithm, in section 2.2. The first cases presented include only the effects of gaseous absorption with zero surface albedo. Later, we present cases with nonzero surface albedo, molecular (“Rayleigh”) scattering and low- and high-altitude clouds in three different atmospheres, including two different treatments of cloud absorption, i.e., nongray and gray. In each of the cases, we compare FSCK broadband shortwave fluxes and heating rates to LBL calculations. Chapter 2 also includes a discussion of our preliminary conclusions regarding the suitability of the FSCK method for further development as an atmospheric radiative transfer parameterization.

In Chapter 3 we advance the FSCK method from a model that can be applied to an atmosphere with pre-specified pressures, temperatures, mixing ratios, and cloud properties, as in Chapter 2, to an operational model that calculates fluxes

and heating rates given any input atmospheric conditions. We discuss some of the considerations affecting our choice of pressures, temperatures, and mixing ratios used to calculate tabulated absorption coefficients, as well as our choice of major and minor gas constituents. Later, we describe our method of interpolating from tabulated absorption coefficients to  $k$ -values appropriate for the atmosphere of interest. In sections 3.2–3.4 we describe and test several different approaches for combining constituents, either during the model development process or on-the-fly during model runtime. We also assess the relative accuracy of treating absorption by cloud particles as either gray or nongray in the context of the two-band FSCK approach.

In Chapter 4 we evaluate the performance of the two-band FSCK model relative both to LBL calculations, and to the performance of other operational and research radiative transfer parameterizations. The evaluation is carried out in two stages. First, in section 4.1 we compare the FSCK calculations to the calculations of 24 one-dimensional radiative transfer models that were included in a recent model intercomparison (Barker et al. 2003). Second, we compare FSCK calculations to those of six specific state-of-the-art operational and research models. In section 4.2 we describe, in detail, the methods used by each of the six models to generate optical properties. In this evaluation, we embed the optical properties from the FSCK model, the LBL model, and most of the seven operational and research models into the two-stream solver of Zdunkowski et al. (1982), thus permitting us

to make a direct evaluation of heating rate differences due to treatments of optical properties. Chapter 4 concludes with a presentation of the results of the evaluation of the FSCK model relative to the LBL and seven operational and research model calculations.

We summarize the results in Chapter 5 and discuss a number of suggestions to develop further the FSCK method for applications in atmospheric radiative transfer.

# Chapter 2

## The FSCK Algorithm

### 2.1 Model Background

The correlated  $k$ -distribution and FSCK methods are similar. In both methods the strongly variable absorption coefficients,  $k$ , are sorted into smooth, monotonically increasing cumulative  $k$ -distributions, which can be integrated with a few calculations. In the correlated  $k$ -distribution method, however, the spectral range of the absorption coefficients to be sorted is limited by the fact that the emission source function must be constant over that range, while in the FSCK method there is no restriction on the spectral range to be sorted. To demonstrate the difference between the correlated  $k$ -distribution and FSCK approaches, derivations of the two methods by Modest (2003), with slight changes in the notation to make it more consistent with atmospheric radiation nomenclature, are reproduced here for

convenience.

### 2.1.1 Correlated $k$ -distributions

The differential form of the radiative transfer equation for an absorbing, emitting, and scattering medium is, after Modest (2003),

$$\begin{aligned} \frac{dI(s, \underline{\Omega}, \lambda)}{ds} = & -[k_a(\underline{\varphi}(s), \lambda) + k_s(\underline{\varphi}(s), \lambda)]I(s, \underline{\Omega}, \lambda) \\ & + k_a(\underline{\varphi}(s), \lambda)B(T(s), \lambda) \\ & + \frac{k_s(\underline{\varphi}(s), \lambda)}{4\pi} \int_{4\pi} I(s, \underline{\Omega}', \lambda) p(\underline{\varphi}(s), \underline{\Omega}', \underline{\Omega}, \lambda) d\underline{\Omega}', \end{aligned} \quad (2.1)$$

where  $s$  is position,  $I$  is monochromatic radiance,  $B$  is the Planck function,  $T$  is temperature,  $k_a$  and  $k_s$  are absorption and scattering coefficients,  $p$  is the scattering phase function,  $\underline{\varphi}$  is an array of state variables, including pressure, temperature, and mixing ratio,  $\underline{\Omega}$  and  $\underline{\Omega}'$  are solid angles, and  $\lambda$  is wavelength. Assuming that the absorption coefficients are correlated across states  $\underline{\varphi}$ , the set of wavelengths  $\lambda$  for which  $k_a(\underline{\varphi}_0, \lambda)$  equals some value  $k$ , where  $\underline{\varphi}_0$  is an arbitrary reference state, must also be the set of wavelengths  $\lambda$  for which  $k_a(\underline{\varphi}, \lambda)$  equals some value  $k^*$ , where  $\underline{\varphi}$  is any arbitrary set of state variables. Since the mapping to  $k^*$  depends upon both  $\underline{\varphi}$  and  $\lambda$ , or alternatively  $k$ , we write  $k^*$  as a function  $k_a^* = k_a^*(\underline{\varphi}, k)$ .

This mapping is represented mathematically by multiplying equation (2.1) by the Dirac delta function,  $\delta(k - k_a(\underline{\varphi}_0, \lambda))$ , and integrating over a spectral interval  $\Delta\lambda$  sufficiently narrow that the Planck function, scattering coefficient, and scat-

tering phase function are approximately constant across the interval. The result is

$$\begin{aligned} \frac{dI_k(s, \underline{\Omega})}{ds} = & -[k_a^*(\underline{\varphi}(s), k) + k_s(\underline{\varphi}(s))]I_k(s, \underline{\Omega}) \\ & + k_a^*(\underline{\varphi}(s), k)f(\underline{\varphi}_0, k)B(T(s)) \\ & + \frac{k_s(\underline{\varphi}(s))}{4\pi} \int_{4\pi} I_k(s, \underline{\Omega}')p(\underline{\varphi}(s), \underline{\Omega}', \underline{\Omega})d\underline{\Omega}', \end{aligned} \quad (2.2)$$

where

$$f(\underline{\varphi}_0, k) = \frac{1}{\Delta\lambda} \int_{\Delta\lambda} \delta(k - k_a(\underline{\varphi}_0, \lambda))d\lambda \quad (2.3)$$

is the  $k$ -distribution function evaluated at the reference state  $\underline{\varphi}_0$ ,

$$I_k(s, \underline{\Omega}) = \frac{1}{\Delta\lambda} \int_{\Delta\lambda} I(s, \underline{\Omega}, \lambda)\delta(k - k_a(\underline{\varphi}_0, \lambda))d\lambda = I(s, \underline{\Omega}, k)f(\underline{\varphi}_0, k) \quad (2.4)$$

is the probability of occurrence-weighted radiance  $I(s, \underline{\Omega}, k)$  across the interval  $\Delta\lambda$ , and the wavelength dependencies for the scattering coefficient, phase function and Planck function have been dropped as they are constant across  $\Delta\lambda$ . The cumulative  $k$ -distribution function evaluated at the reference state, i.e.,

$$g(\underline{\varphi}_0, k) = \int_0^k f(\underline{\varphi}_0, k')dk', \quad (2.5)$$

is equivalent to a non-dimensional wavelength. Dividing Eq. (2.2) by  $f(\underline{\varphi}_0, k)$

transforms the variable of integration from  $k$  to  $g$ , and we obtain

$$\begin{aligned} \frac{dI_g(s, \underline{\Omega})}{ds} = & -[k_a^*(\underline{\varphi}(s), g) + k_s(\underline{\varphi}(s))]I_g(s, \underline{\Omega}) \\ & + k_a^*(\underline{\varphi}(s), g)B(T(s)) \\ & + \frac{k_s(\underline{\varphi}(s))}{4\pi} \int_{4\pi} I_g(s, \underline{\Omega}')p(\underline{\varphi}(s), \underline{\Omega}', \underline{\Omega})d\underline{\Omega}', \end{aligned} \quad (2.6)$$

where  $I_g = I_k/f(\underline{\varphi}_0, k)$ . This operation is possible since  $f(\underline{\varphi}_0, k)$  has no dependence on location  $s$ . The total radiance over  $\Delta\lambda$  is now the integral of Eq. (2.6) over  $g$  from 0 to 1. Because the  $k_a^*(\underline{\varphi}(s), g)$  vary smoothly with  $g$ , results from Eq. (2.6) can be integrated with very few quadrature points.

### 2.1.2 Full-Spectrum Correlated $k$ -distributions for Longwave Radiative Transfer

The FSCK method extends the correlated  $k$ -distribution approach by relaxing the constraint that  $B(T(s), \lambda)$  be constant across the interval  $\Delta\lambda$ . As a result, in the FSCK approach  $\Delta\lambda$  can now be arbitrarily large, even the full spectrum, as long as the scattering coefficients and phase functions are reasonably treated as constants across  $\Delta\lambda$ . This is a significant enhancement to the correlated  $k$ -distribution approach, especially for spectral regions in which the scattering coefficients do not vary strongly with wavelength (e.g., Fig. 2.1a), while cloud absorption coefficients do (e.g., Fig. 2.1b).

Although the focus of this work is an algorithm for shortwave radiative transfer,

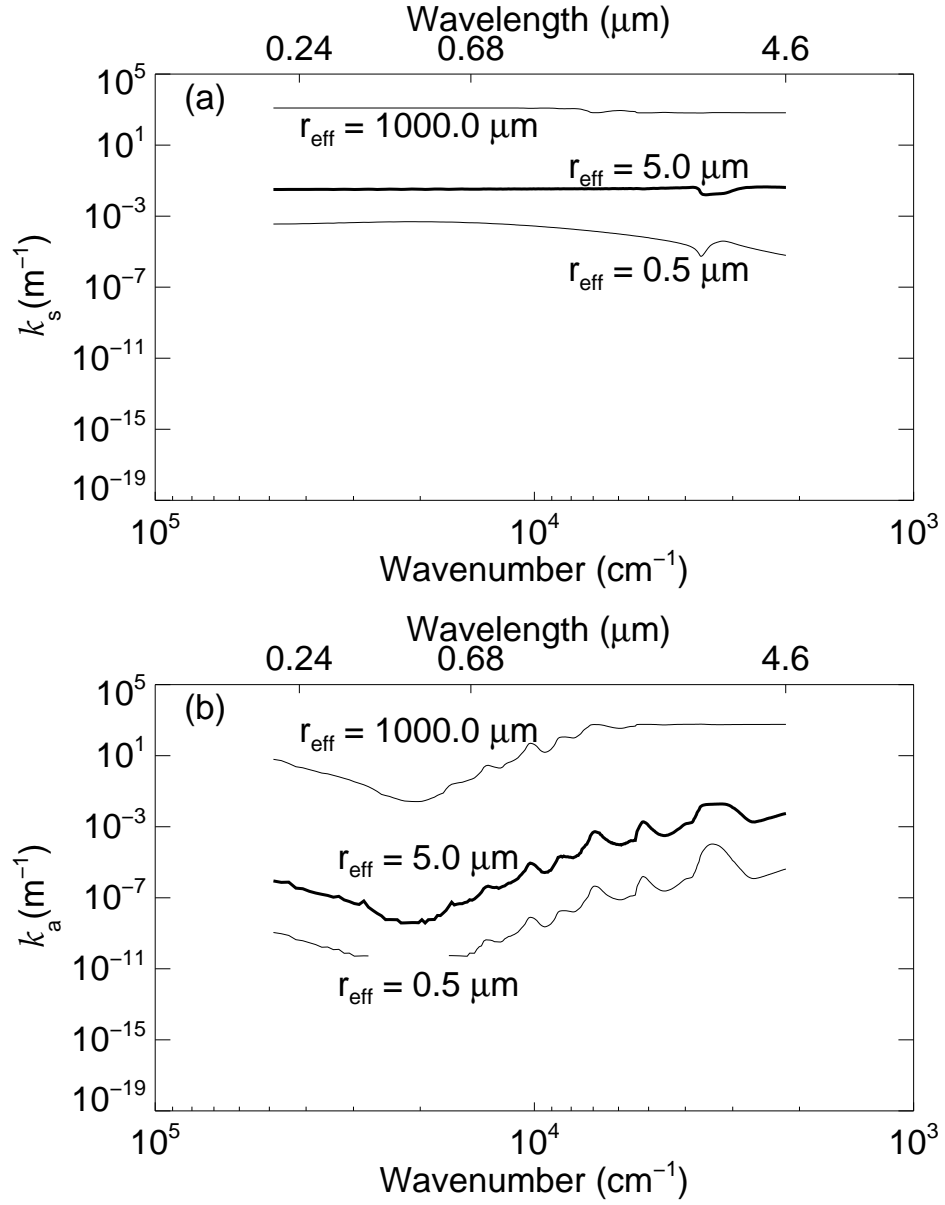


**Figure 2.1.** Absorption and scattering coefficients for three different effective radii,  $r_{\text{eff}}$ , of a lognormal distribution of liquid water drops with a number concentration of  $300 \text{ cm}^{-3}$ . (a) Scattering coefficients. (b) Absorption coefficients.

we begin by developing the case for longwave radiative transfer, since the shortwave case is essentially a simplification of the longwave case. The starting point for the FSCK model for longwave radiative transfer, as in the case of combustion applications or atmospheric emission, is again the transformation of Eq. (2.1) using the Dirac delta function,  $\delta(k - k_a(\underline{\varphi}_0, \lambda))$ , but the emission term is treated in a manner that allows it to vary spectrally. Multiplying Eq. (2.1) by  $\delta(k - k_a(\underline{\varphi}_0, \lambda))$  and integrating over  $\Delta\lambda$ , we now have

$$\begin{aligned} \frac{dI_k(s, \underline{\Omega})}{ds} = & -[k_a^*(\underline{\varphi}(s), k) + k_s(\underline{\varphi}(s))]I_k(s, \underline{\Omega}) \\ & + k_a^*(\underline{\varphi}(s), k)f(T(s), \underline{\varphi}_0, k)B_{\Delta\lambda}(T(s)) \\ & + \frac{k_s(\underline{\varphi}(s))}{4\pi} \int_{4\pi} I_k(s, \underline{\Omega}')p(\underline{\varphi}(s), \underline{\Omega}', \underline{\Omega})d\underline{\Omega}', \end{aligned} \quad (2.7)$$

where  $B_{\Delta\lambda}(T(s))$  is the Planck function integrated over the spectral interval  $\Delta\lambda$ ,

$$I_k(s, \underline{\Omega}) = \int_{\Delta\lambda} I(s, \underline{\Omega}, \lambda)\delta(k - k_a(\underline{\varphi}_0, \lambda))d\lambda, \quad (2.8)$$

with no advantage of defining  $I_k(s, \underline{\Omega})$  in terms of  $f(\underline{\varphi}_0, k)$ , and

$$f(T(s), \underline{\varphi}_0, k) = \frac{1}{B_{\Delta\lambda}(T(s))} \int_{\Delta\lambda} B(T(s), \lambda)\delta(k - k_a(\underline{\varphi}_0, \lambda))d\lambda. \quad (2.9)$$

Note that to eliminate the requirement that the Planck function must be constant over the spectral interval being sorted, the  $k$ -distribution is redefined using the Planck function as a weighting function; that is, the  $k$ -distribution has gained

temperature dependence through the Planck function.

In terms of the temperature-dependent  $k$ -distribution the cumulative  $k$ -distribution function becomes

$$\begin{aligned}
 g(T(s), \underline{\varphi}_0, k) &= \int_0^k f(T(s), \underline{\varphi}_0, k') dk' \\
 &= \int_0^{k^*} f(T(s), \underline{\varphi}, k^{*'}) dk^{*'} \\
 &= g(T(s), \underline{\varphi}, k^*).
 \end{aligned} \tag{2.10}$$

The temperature dependence of the  $k$ -distribution in Eq. (2.9) is problematic, as it introduces a dependence on location  $s$  into the  $k$ -distribution. If we were to transform from  $k$  to  $g$  in Eq. (2.7), we would no longer be able to define  $I_g = I_k/f(T(s), \underline{\varphi}_0, k)$  as the dependence of  $f$  on  $s$  precludes us from bringing  $f$  inside the derivative on the left hand side of the equation. To circumvent this problem Modest and Zhang (2002) use an arbitrary reference temperature  $T_{\text{ref}}$  to create a reference cumulative  $k$ -distribution function:

$$\begin{aligned}
 g(T_{\text{ref}}, \underline{\varphi}_0, k) &= \int_0^k f(T_{\text{ref}}, \underline{\varphi}_0, k') dk' \\
 &= \int_0^{k^*} f(T_{\text{ref}}, \underline{\varphi}, k^{*'}) dk^{*'} \\
 &= g(T_{\text{ref}}, \underline{\varphi}, k^*),
 \end{aligned} \tag{2.11}$$

where  $T_{\text{ref}}$  refers to the temperature at which the Planck function is evaluated in Eq. (2.9).

It must be noted that there can be many sources of emission (e.g.,  $B(T(s))$ ,  $B(T(0))$ ,  $I_{\text{sun}}$ ) that can be used to define the emission-weighted  $k$ -distribution. However, only one source may be used to define  $I_g$  and  $g_{\text{ref}}$  in a given problem. The case of a solar source of emission will be discussed in Section 2.1.3, but here we continue the development for the case of longwave emission.

Dividing Eq. (2.7) by Eq. (2.9) with the temperature  $T$  evaluated at  $T_{\text{ref}}$ , we obtain

$$\begin{aligned} \frac{dI_{g_{\text{ref}}}(s, \underline{\Omega})}{ds} &= -[k_{\text{a}}^*(\underline{\varphi}(s), g_{\text{ref}}) + k_{\text{s}}(\underline{\varphi}(s))]I_{g_{\text{ref}}}(s, \underline{\Omega}) \\ &\quad + k_{\text{a}}^*(\underline{\varphi}(s), g_{\text{ref}})a(T(s), T_{\text{ref}}, g_{\text{ref}})B_{\Delta\lambda}(T(s)) \\ &\quad + \frac{k_{\text{s}}(\underline{\varphi}(s))}{4\pi} \int_{4\pi} I_{g_{\text{ref}}}(s, \underline{\Omega}')p(\underline{\varphi}(s), \underline{\Omega}', \underline{\Omega})d\underline{\Omega}', \end{aligned} \quad (2.12)$$

where

$$I_{g_{\text{ref}}}(s, \underline{\Omega}) = I_k(s, \underline{\Omega})/f(T_{\text{ref}}, \underline{\varphi}_0, k) \quad (2.13)$$

and

$$\begin{aligned} a(T(s), T_{\text{ref}}, g_{\text{ref}}) &= f(T(s), \underline{\varphi}_0, k)/f(T_{\text{ref}}, \underline{\varphi}_0, k) \\ &= dg(T(s), \underline{\varphi}_0, k)/dg(T_{\text{ref}}, \underline{\varphi}_0, k). \end{aligned} \quad (2.14)$$

In Eq. (2.14)  $a(T(s), T_{\text{ref}}, g_{\text{ref}})$  is a nongray parameter (Modest 2003) that adjusts each local cumulative  $k$ -distribution in the emission term to account for differences between the Planck function evaluated at the local temperature and the Planck

function evaluated at the reference temperature. For notational convenience we replace  $g_{\text{ref}}$  with  $g$  and write the absorption coefficient as  $k_a^*(T_{\text{ref}}, \underline{\varphi}, g)$  to indicate explicitly that the absorption coefficients are evaluated according to the local state variables,  $\underline{\varphi}$ , and are subsequently weighted in the  $k$ -distribution by a Planck function evaluated at the reference temperature  $T_{\text{ref}}$ . With these changes we have

$$\begin{aligned} \frac{dI_g(s, \underline{\Omega})}{ds} = & -[k_a^*(T_{\text{ref}}, \underline{\varphi}(s), g) + k_s(\underline{\varphi}(s))]I_g(s, \underline{\Omega}) \\ & + k_a^*(T_{\text{ref}}, \underline{\varphi}(s), g)a(T(s), T_{\text{ref}}, g)B_{\Delta\lambda}(T(s)) \\ & + \frac{k_s(\underline{\varphi}(s))}{4\pi} \int_{4\pi} I_g(s, \underline{\Omega}')p(\underline{\varphi}(s), \underline{\Omega}', \underline{\Omega})d\underline{\Omega}'. \end{aligned} \quad (2.15)$$

The upper boundary condition for the longwave case is  $I^\downarrow(s_{\text{top}}, \underline{\Omega}, \lambda) = 0$  since there is no source of longwave emission above  $s_{\text{top}}$ . The lower boundary condition is given by

$$I^\uparrow(0, \underline{\Omega}, \lambda) = \epsilon(0, \lambda)B(T(0), \lambda) + \frac{1 - \epsilon(0, \lambda)}{\pi} \int_{2\pi} I^\downarrow(0, \underline{\Omega}', \lambda)(\cos \theta)d\underline{\Omega}', \quad (2.16)$$

where  $\epsilon(0)$  is assumed to be a Lambertian, i.e., isotropic, emissivity and  $T(0)$  is the temperature of the emitting surface (i.e., location 0).

Because the upper boundary condition is trivial we do not develop it further. However, the lower boundary condition must be transformed to use  $g$  as the variable of integration. As with the radiative transfer equation we begin by applying the assumption of correlation; that is, we multiply Eq. (2.16) by  $\delta(k - k_a(\underline{\varphi}_0, \lambda))$

and integrate over  $\Delta\lambda$  to obtain

$$I_k^\uparrow(0, \underline{\Omega}) = \bar{\epsilon}(0)B_{\Delta\lambda}(T(0))f(T(0), \underline{\phi}_0, k) + \frac{1 - \bar{\epsilon}(0)}{\pi} \int_{2\pi} I_k^\downarrow(0, \underline{\Omega}')(\cos \theta)d\underline{\Omega}', \quad (2.17)$$

where  $B_{\Delta\lambda}(T(0))$  is the Planck function evaluated at the surface temperature and integrated over  $\Delta\lambda$ , and  $\bar{\epsilon}(0)$  is the mean emissivity over the spectral interval.

Since the surface of the Earth emits radiation at temperatures similar to those of the atmosphere, it is appropriate to use the same definition for the  $k$ -distribution as was used for internal atmospheric emission in Eq. (2.9). Again evaluating the Planck function in Eq. (2.9) at  $T_{\text{ref}}$  and using the definition of  $g(T_{\text{ref}}, \underline{\varphi}_0, k)$  from Eq. (2.11) we divide Eq. (2.17) by  $f(T_{\text{ref}}, \underline{\phi}_0, k)$  to arrive at

$$I_g^\uparrow(0, \underline{\Omega}) = \bar{\epsilon}(0)B_{\Delta\lambda}(T(0))a(T(0), T_{\text{ref}}, k) + \frac{1 - \bar{\epsilon}_{\text{sfc}}}{\pi} \int_{2\pi} I_g^\downarrow(0, \underline{\Omega}')(\cos \theta)d\underline{\Omega}', \quad (2.18)$$

where we have substituted  $g$  for  $g_{\text{ref}}$  for notational convenience.

### 2.1.3 Full-Spectrum Correlated $k$ -distributions for Shortwave Radiative Transfer

In the special case of no internal source of emission the second term of Eq. (2.1) is zero, so Eq. (2.1) becomes

$$\begin{aligned} \frac{dI(s, \underline{\Omega}, \lambda)}{ds} &= -[k_a(\underline{\varphi}(s), \lambda) + k_s(\underline{\varphi}(s), \lambda)]I(s, \underline{\Omega}, \lambda) \\ &+ \frac{k_s(\underline{\varphi}(s), \lambda)}{4\pi} \int_{4\pi} I(s, \underline{\Omega}', \lambda) p(\underline{\varphi}(s), \underline{\Omega}', \underline{\Omega}, \lambda) d\underline{\Omega}', \end{aligned} \quad (2.19)$$

The boundary conditions for an external solar source are

$$I^\downarrow(s_{\text{top}}, \underline{\Omega}, \lambda) = I_{\text{sun}}^\downarrow(s_{\text{top}}, \underline{\Omega}, \lambda) \equiv q_{\text{sun}}^{\text{TOA}}(\lambda) \delta(\underline{\Omega} - \underline{\Omega}_{\text{sol}}) \quad (2.20)$$

for the downward radiance at the top of the atmosphere (i.e., location  $s_{\text{top}}$ ) where  $q_{\text{sun}}^{\text{TOA}}(\lambda)$  is the solar irradiance at the top of the atmosphere, i.e., the solar source function, and  $\underline{\Omega}_{\text{sol}}$  is the solid angle of incident solar radiation. The lower boundary condition for the upward radiance at the bottom of the atmosphere (i.e., location 0) is given by

$$I^\uparrow(0, \underline{\Omega}, \lambda) = \frac{\alpha}{\pi} \int_{2\pi} I^\downarrow(0, \underline{\Omega}', \lambda) (\cos \theta) d\underline{\Omega}'. \quad (2.21)$$

We have assumed a Lambertian, i.e., isotropically scattering, surface with albedo  $\alpha$ . Multiplying these boundary conditions and Eq. (2.19) by  $\delta(k - k_a(\underline{\varphi}_0, \lambda))$  and

integrating over  $\Delta\lambda$ , the broadband spectral interval of interest, we obtain

$$I_k^\downarrow(s_{\text{top}}, \underline{\Omega}) = I_{\text{sun}, \Delta\lambda}^\downarrow(s_{\text{top}}, \underline{\Omega}) f(I_{\text{sun}}^\downarrow, \underline{\varphi}_0, k), \quad (2.22)$$

$$I_k^\uparrow(0, \underline{\Omega}) = \frac{\alpha}{\pi} \int_{2\pi} I_k^\downarrow(0, \underline{\Omega}') (\cos \theta) d\underline{\Omega}', \quad (2.23)$$

and

$$\begin{aligned} \frac{dI_k(s, \underline{\Omega})}{ds} &= -[k_a^*(\underline{\varphi}(s), k) + k_s(\underline{\varphi}(s))] I_k(s, \underline{\Omega}) \\ &+ \frac{k_s(\underline{\varphi}(s))}{4\pi} \int_{4\pi} I_k(s, \underline{\Omega}') p(\underline{\varphi}(s), \underline{\Omega}', \underline{\Omega}) d\underline{\Omega}', \end{aligned} \quad (2.24)$$

where

$$\begin{aligned} I_k^{\uparrow\downarrow}(s, \underline{\Omega}) &= \int_{\Delta\lambda} I^{\uparrow\downarrow}(s, \underline{\Omega}, \lambda) \delta(k - k_a(\underline{\varphi}_0, \lambda)) d\lambda \\ &= I^{\uparrow\downarrow}(s, \underline{\Omega}, k) f(I_{\text{sun}}^\downarrow, \underline{\varphi}_0, k), \end{aligned} \quad (2.25)$$

$$f(I_{\text{sun}}^\downarrow, \underline{\varphi}_0, k) = \frac{1}{I_{\text{sun}, \Delta\lambda}^\downarrow(s_{\text{top}}, \underline{\Omega})} \int_{\Delta\lambda} I_{\text{sun}}^\downarrow(s_{\text{top}}, \underline{\Omega}, \lambda) \delta(k - k_a(\underline{\varphi}_0, \lambda)) d\lambda, \quad (2.26)$$

and  $I_{\text{sun}, \Delta\lambda}^\downarrow(s_{\text{top}}, \underline{\Omega})$  is the integral of the incident solar radiation over  $\Delta\lambda$ , the broadband spectral interval of interest.

Dividing Eqs. (2.22)–(2.24) by  $f(I_{\text{sun}}^\downarrow, \underline{\varphi}_0, k)$ , which is independent of location  $s$  and can be taken inside the derivative on the left hand side of Eq. (2.24), we obtain

$$I_g^\downarrow(s_{\text{top}}, \underline{\Omega}) = I_{\text{sun}, \Delta\lambda}^\downarrow(s_{\text{top}}, \underline{\Omega}), \quad (2.27)$$

$$I_g^\uparrow(0, \underline{\Omega}) = \frac{\alpha}{\pi} \int_{2\pi} I_g^\downarrow(0, \underline{\Omega}') (\cos \theta) d\underline{\Omega}', \quad (2.28)$$

and

$$\begin{aligned} \frac{dI_g(s, \underline{\Omega})}{ds} &= -[k_a^*(\underline{\varphi}(s), k) + k_s(\underline{\varphi}(s))] I_g(s, \underline{\Omega}) \\ &+ \frac{k_s(\underline{\varphi}(s))}{4\pi} \int_{4\pi} I_g(s, \underline{\Omega}') p(\underline{\varphi}(s), \underline{\Omega}', \underline{\Omega}) d\underline{\Omega}', \end{aligned} \quad (2.29)$$

where

$$I_g^{\uparrow\downarrow}(s, \underline{\Omega}) = I_k^{\uparrow\downarrow}(s, \underline{\Omega}) / f(I_{\text{sun}}^\downarrow, \underline{\varphi}_0, k). \quad (2.30)$$

The cumulative  $k$ -distribution function evaluated with the solar spectral distribution of radiance is

$$g(I_{\text{sun}}^\downarrow, \underline{\varphi}_0, k) = \int_0^k f(I_{\text{sun}}^\downarrow, \underline{\varphi}_0, k') dk'. \quad (2.31)$$

For an absorbing atmosphere and a gray scattering atmosphere with or without absorption, only one spectral interval for the entire spectrum is necessary if the assumption of correlation remains valid. One source of loss of correlation in gaseous absorption between two regions of space is the presence of gradients of temperature in the medium, as in the case of a combustion system. For example, at extremely high temperatures some gas absorption lines, so-called “hot lines,” which originate from excited transitions, are present at spectral locations where there are no lines at room temperature. Another reason for a breakdown in correlation is vertical gradients of opposite sign for mixing ratios of different absorbing species, leading to a loss of correlation in the absorption coefficients with height.

Loss of correlation in the atmosphere results from vertical gradients of ozone and water vapor absorption (Figs. 2.2a–b), as well as with absorption in clouds and their surrounding cloud-free layers (Figs. 2.2b–c). High in the atmosphere (Fig. 2.2a), the strongest water vapor lines are similar in magnitude to ozone continuum absorption near  $0.24 \mu\text{m}$ , so these lines will be sorted into nearly the same part of the cumulative  $k$ -distribution. Lower in the troposphere (Fig. 2.2b), the water vapor lines are much stronger relative to ozone continuum absorption near  $0.24 \mu\text{m}$ , so these lines will be sorted into a different part of the cumulative  $k$ -distribution at that level. As described in the Introduction, this change of the relative sorting of absorption lines between atmospheric levels results in a breakdown of correlation and introduces error into the integration in  $g$ -space.

An example of the manner in which the presence of clouds can violate the assumption of correlation is shown in Figs. 2.2b–c. In Fig. 2.2b, which shows absorption for a clear-sky layer, absorption at point 1 has a similar magnitude to that at point 3, and is smaller than at point 2. However, when nongray cloud absorption coefficients (Fig. 2.1b) are added to the same atmospheric layer (Fig. 2.2c), absorption at point 1 becomes greater than both points 2 and 3. So, if clear-sky absorption in this layer had been correlated with clear-sky absorption in neighboring layers, the assumption of correlation would break down in the presence of cloud. Examples of these problems will be discussed in more detail in Section 2.2 along with an adaptation of the FSCK method to circumvent them.

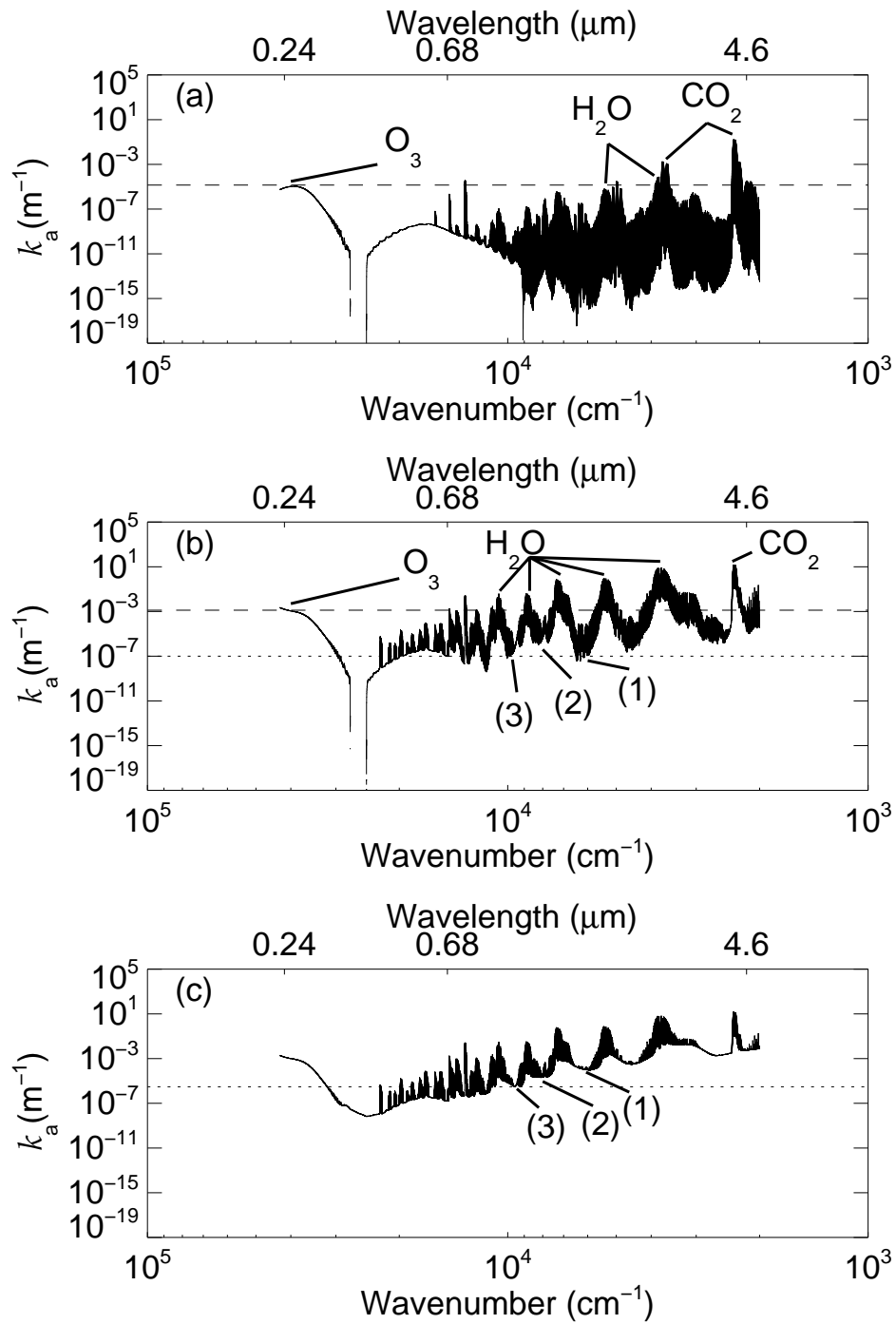


**Figure 2.2.** Combined absorption coefficients of water vapor, carbon dioxide, ozone, nitrous oxide, carbon monoxide, methane, and oxygen at (a) 0.179 hPa and 248.2 K, (b) 841.783 hPa and 267.0 K, and (c) the same as (b) except with absorption coefficients of lognormally distributed cloud liquid water drops with an effective radius of 5.0  $\mu\text{m}$  and a number concentration of 300  $\text{cm}^{-3}$  added to the gas absorption coefficients. (a) and (b) The dashed line is a point of reference to compare the strengths of water vapor lines relative to ozone continuum absorption. (b) and (c) The dotted line is a point of reference to compare the relative strengths of points 1, 2, and 3.

### 2.1.4 Sorting

In practice, the method of sorting the absorption coefficients to construct the solar source function-weighted  $k$ -distribution and then transforming it to make the equivalent fractional solar source function-weighted cumulative  $k$ -distribution,  $g$ , is straightforward. The range of absorption coefficient values is divided into bins. To construct an ordinary  $k$ -distribution, we compute the fraction,  $f(k)\delta k$ , of the wavelength domain occupied by absorption coefficients in each “ $k$ -bin,” i.e., between  $k$  and  $k + \delta k$  (e.g., Goody and Yung 1989). When an absorption coefficient falls within a bin range, the bin count is incremented by the monochromatic wavelength interval,  $\delta\lambda$ , at that spectral location. Note that if the wavelength interval,  $\delta\lambda$ , were constant across the spectrum, it would be sufficient to increment the bin counter by one for each occurrence within a  $k$ -bin. To construct a solar source function-weighted  $k$ -distribution (Fig. 2.3c), rather than incrementing the bin count by  $\delta\lambda$  at that spectral location, the bin count is incremented by the value of the solar source function (Fig. 2.3a) times  $\delta\lambda$  at that spectral location.

The range of values of gas absorption coefficients encountered in the McClatchey mid-latitude winter atmosphere (McClatchey et al. 1972) falls between  $10^{-22}$ – $10^2$   $\text{m}^{-1}$ . This range is divided into  $\log_{10}(k)$  bins, with 100 bins per order of magnitude, for a total of 2401 bins. Once the solar source function-weighted  $k$ -distribution (Fig. 2.3c) is constructed, the transformation to the cumulative  $k$ -distribution,  $g$  (Fig. 2.3d), is accomplished by adding up the  $k$ -bins, i.e.,

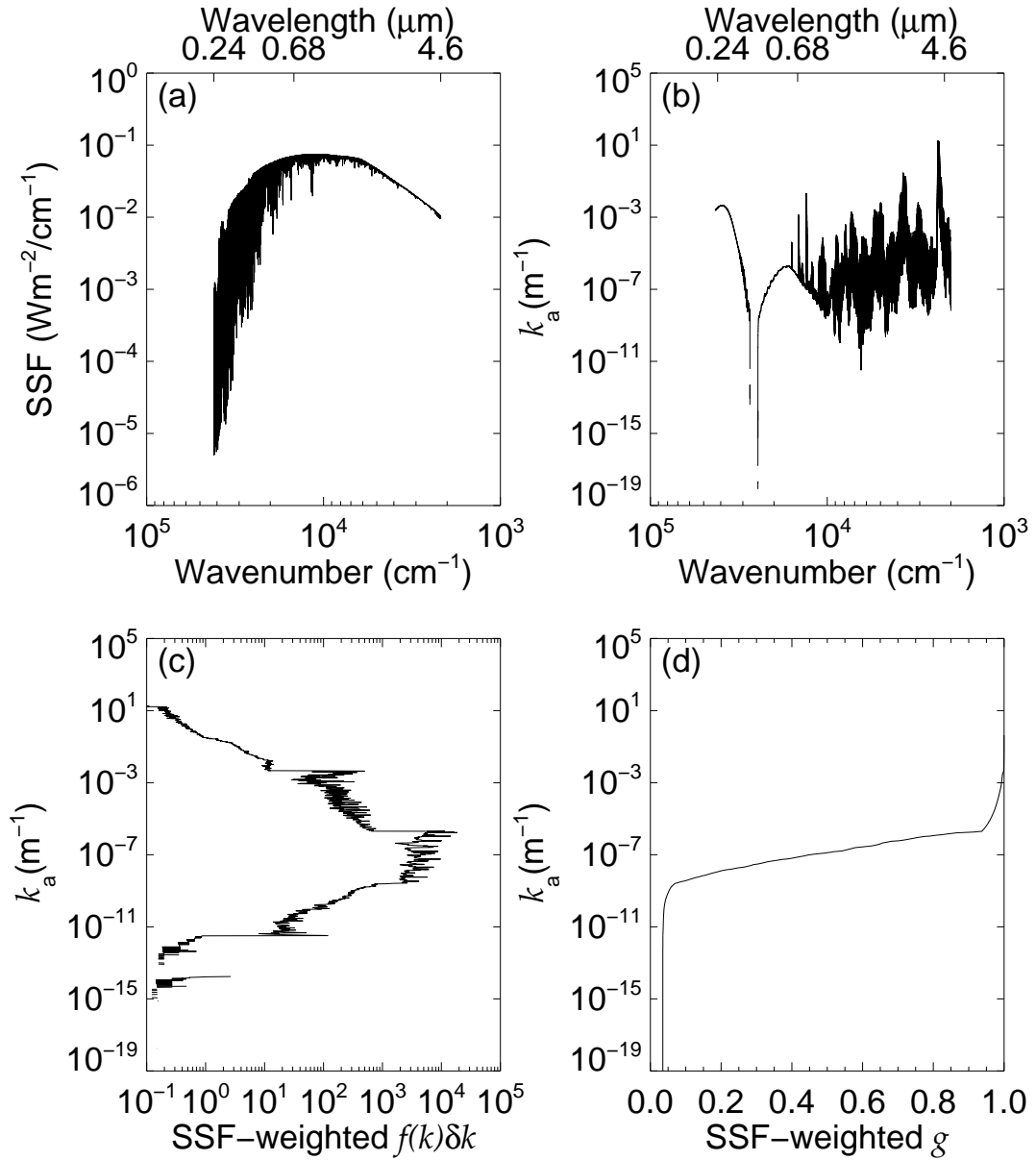


**Figure 2.3.** (a) Solar Source Function (SSF), (b) combined absorption coefficients of water vapor, carbon dioxide, ozone, nitrous oxide, carbon monoxide, methane, and oxygen at 148.949 hPa and 217.9 K, (c) SSF-weighted  $k$ -distribution, and (d) SSF-weighted cumulative  $k$ -distribution.

$g_i = g_{i-1} + f_i \delta k_i$  where  $i$  is the  $k$ -bin index,  $f_i \delta k_i$  is the value of the  $k$ -distribution in the  $i^{\text{th}}$  bin, and  $g_{i-1}$  is the value of the cumulative  $k$ -distribution up to  $k$ -bin  $i - 1$ . Gaussian quadrature is typically used to integrate the cumulative  $k$ -distribution. The specific method of determining quadrature weights and abscissas used in this work will be discussed in Section 2.2.

## 2.2 Fixed Atmosphere Case Studies

In the case study that follows, the two-stream solver of Zdunkowski et al. (1982) is used for the LBL flux and heating rate calculations. These LBL fluxes and heating rates represent the “truth,” i.e., the baseline for our comparison. For consistency, we also used the same solver in the FSCK calculations. Therefore, in the comparisons between the FSCK calculations and the LBL standard, differences due to model solvers are not a consideration.

### 2.2.1 Case Study Atmospheres, Gases, and Clouds

The vertical profiles of pressure, temperature, water vapor and ozone used for the calculations in this case study are taken from the McClatchey et al. (1972) mid-latitude winter, subarctic winter, and tropical atmospheres and are interpolated to 29 layers with a total of 30 layer boundaries, where the lowest 21 layers are 1 km thick, the next two layers are 2 km thick, the next five layers are 5 km thick, and the top layer is 20 km thick. The profiles of oxygen, carbon

dioxide, carbon monoxide, methane, and nitrous oxide are adapted from a METEO 597A class project at the Pennsylvania State University. The atmospheric profiles for the McClatchey et al. (1972) mid-latitude winter, subarctic winter, and tropical atmospheres with gas constituent volume mixing ratios used in this work are shown in Figs. 2.4–2.6. The gas absorption coefficients are extracted from the HITRAN-96-JPL database (Rothman et al. 1998) using the Line-by-Line Radiative Transfer Model (LBLRTM) version 5.21 (Clough et al. 1992; Clough and Iacono 1995). Absorption coefficients for the individual gas constituents are combined by LBLRTM, so line overlap and continuum absorption are explicitly calculated prior to sorting the combined absorption coefficients.

In the cases where clouds are included the cloud optical properties are calculated using Mie theory according to Toon and Ackerman (1981) for lognormal distributions of liquid- or ice-water spheres with a logarithmic distribution width of 0.38. In our calculations, the liquid-water cloud has a visible optical depth of approximately 30, while the ice cloud is optically thin with a visible optical depth of approximately 0.25. The liquid cloud-drop distribution used here has an effective radius of  $5.0 \mu\text{m}$ . The liquid cloud in these cases, which we also call the low-altitude cloud, is homogeneously distributed between 1000–2000 m of altitude. Our ice-, or high-altitude, cloud-drop distribution has an effective radius of  $75.0 \mu\text{m}$  and is homogeneously distributed in the layer between 7000–8000 m. The cloud optical properties used for the monochromatic line-by-line calculations

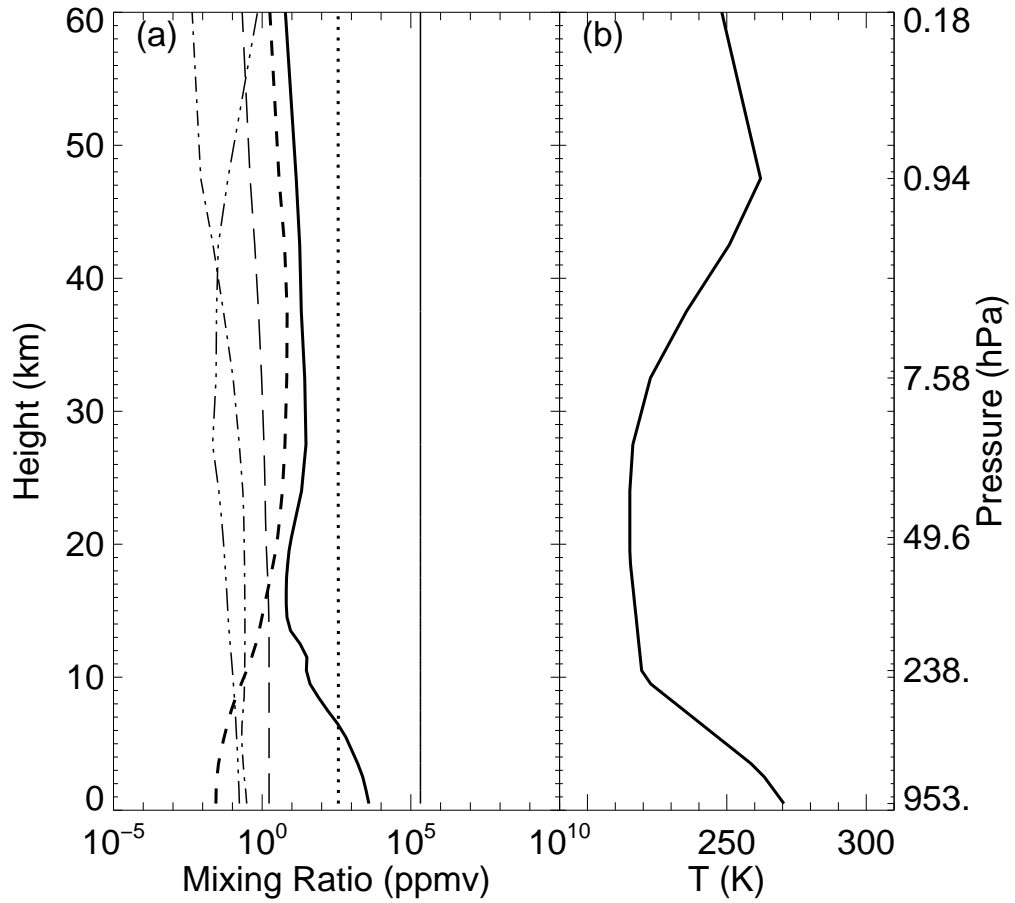


**Figure 2.4.** Gas mixing ratio and temperature profiles for the mid-latitude winter atmosphere of McClatchey et al. (1972). (a) Gas mixing ratios (ppmv). From right to left at 30 km: oxygen (thin solid line), carbon dioxide (dotted line), water vapor (thick solid line), ozone (thick dashed line), methane (thin dashed line), nitrous oxide (dash-dot line), and carbon monoxide (dash-three dots line). (b) Temperature (K).

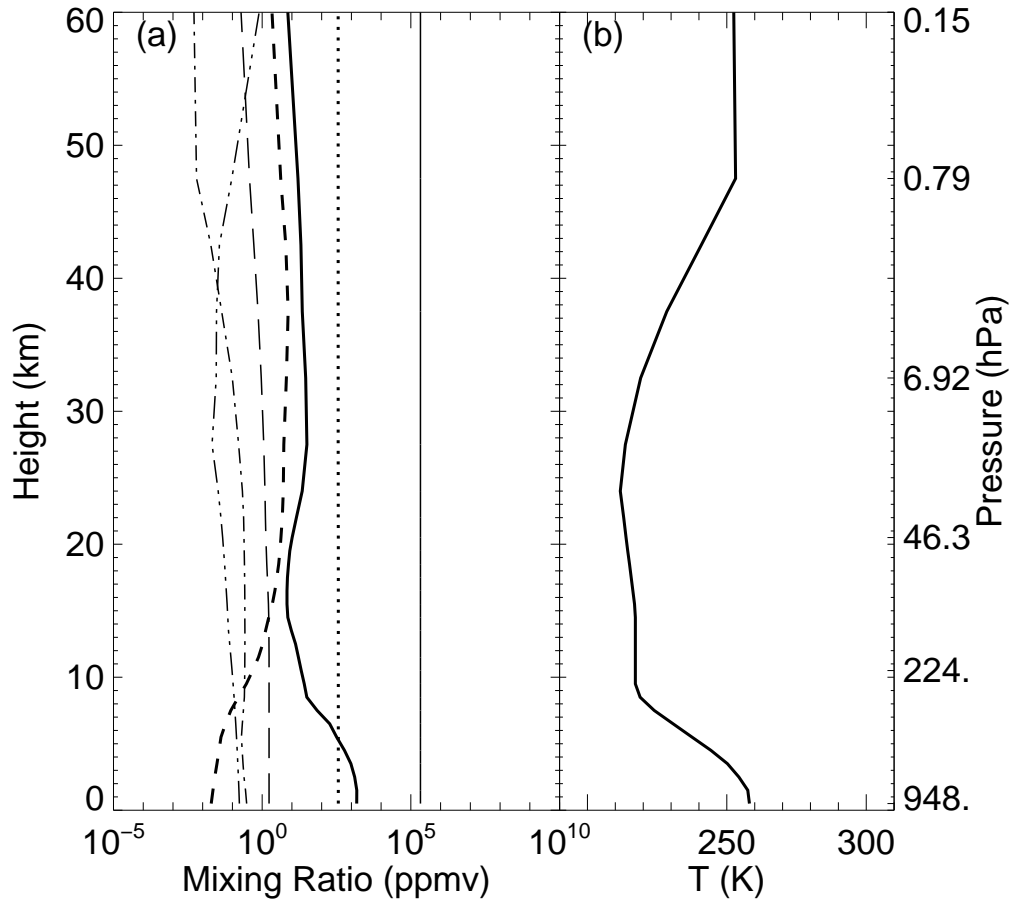


**Figure 2.5.** Gas mixing ratio and temperature profiles for the subarctic winter atmosphere of McClatchey et al. (1972). (a) Gas mixing ratios (ppmv). From right to left at 30 km: oxygen (thin solid line), carbon dioxide (dotted line), water vapor (thick solid line), ozone (thick dashed line), methane (thin dashed line), nitrous oxide (dash-dot line), and carbon monoxide (dash-three dots line). (b) Temperature (K).

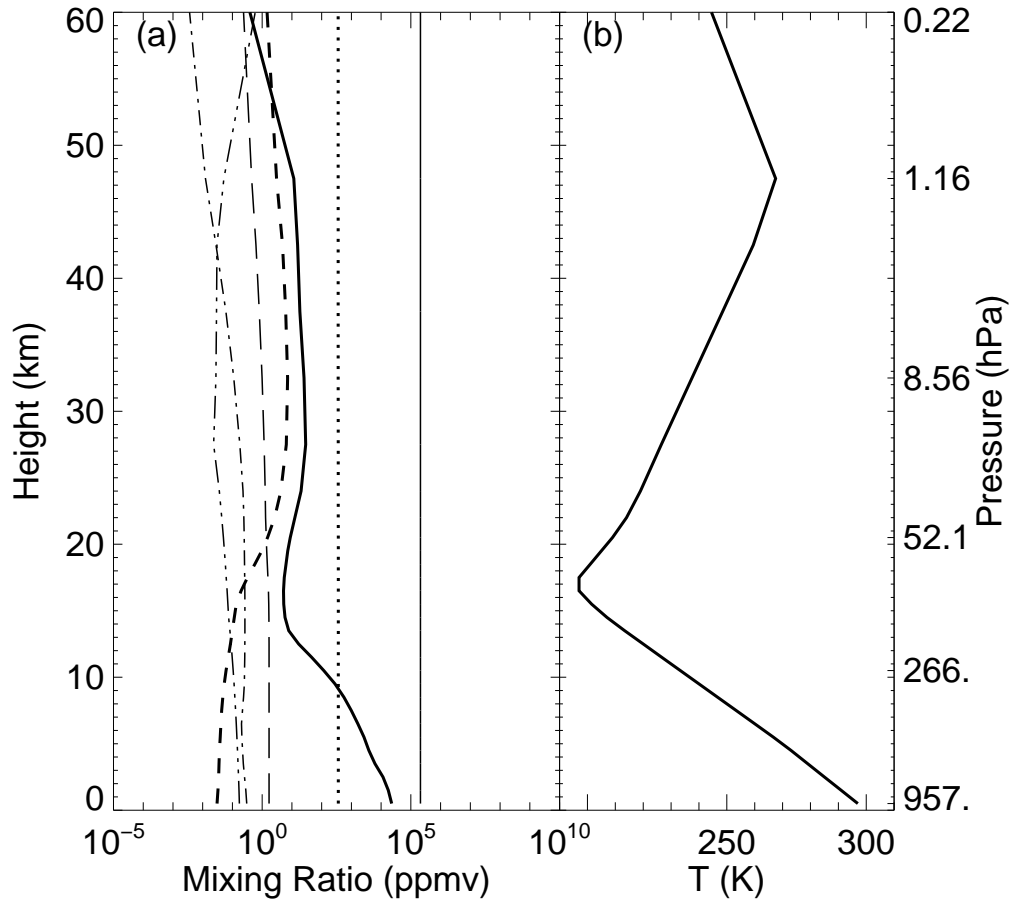


**Figure 2.6.** Gas mixing ratio and temperature profiles for the tropical atmosphere of McClatchey et al. (1972). (a) Gas mixing ratios (ppmv). From right to left at 30 km: oxygen (thin solid line), carbon dioxide (dotted line), water vapor (thick solid line), ozone (thick dashed line), methane (thin dashed line), nitrous oxide (dash-dot line), and carbon monoxide (dash-three dots line). (b) Temperature (K).

were produced at a spectral resolution of  $0.01 \mu\text{m}$  and then interpolated to the wavenumber resolution of the gas absorption coefficients.

### 2.2.2 Clear-Sky Calculations

The first case is a basic test of the FSCK method versus LBL calculations. In this case there are no clouds, no molecular scattering, the surface albedo is zero, and the mid-latitude winter atmospheric profile is used. The full shortwave spectrum ( $0.24\text{--}4.60 \mu\text{m}$ ) is treated as a single spectral band and the gas absorption coefficients are sorted into a single cumulative  $k$ -distribution per layer. For this initial test of the FSCK method, 8192 quadrature points are used for the integration of the cumulative  $k$ -distributions in order to ensure that differences between the FSCK results and the LBL calculations are not due to poor quadrature. This number was selected by doubling the number of quadrature points, starting with one, until the calculated heating rate profile ceased to change with a subsequent doubling of points.

Comparing the vertical profiles of downward fluxes and heating rates for the LBL calculations and the FSCK results (Figs. 2.7a–c), we find less molecular absorption in the FSCK results with the most significant differences in the lowest 14 km of the atmosphere. The heating rate RMS error for the full atmospheric depth is approximately 4.2%, but is nearly 20% for the lowest 14 km. As Figs. 2.2a–b illustrate, these differences result from a loss of correlation between the

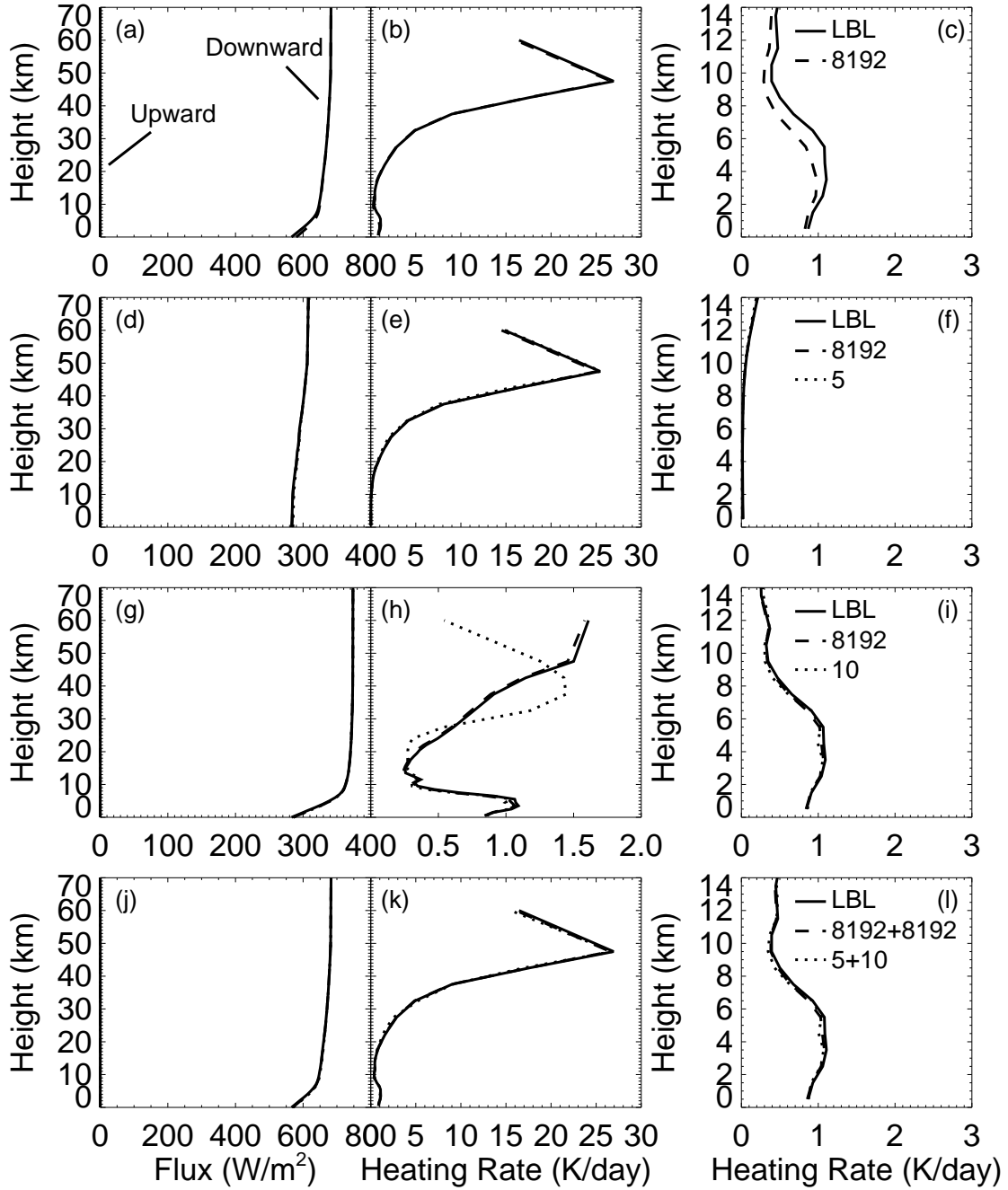


**Figure 2.7.** Upward and downward fluxes (a, d, g, and j), heating rates for all 29 layers (b, e, h, and k), and heating rates for the lowest 14 layers (c, f, i, and l) for (a–c) the full shortwave spectrum (0.24–4.6 μm) treated as a single band, (d–f) band 1 (0.24–0.68 μm), (g–i) band 2 (0.68–4.6 μm), and (j–l) the full shortwave spectrum treated by adding bands 1 and 2. The LBL solution, the 8192 quadrature point solution, and the 15 quadrature point solution are given by the solid, dashed, and dotted lines, respectively.

$k$ -distributions for different vertical levels as a result of different vertical gradients in the water vapor and ozone mixing ratios. This condition is always present in the atmosphere of Earth.

Since absorption by ozone is dominant in the upper atmosphere, less absorbing in the lower atmosphere relative to the other gases, and nearly the only mechanism for absorption in the spectral range from 0.24–0.68  $\mu\text{m}$ , we separate the shortwave spectrum into two bands, with band 1 from 0.24–0.68  $\mu\text{m}$  and band 2 from 0.68–4.60  $\mu\text{m}$ , and test the assumption of vertical correlation within each of these two spectral bands.

This approach is similar to the part-spectrum approach described by Modest and Riazzi (2004), in which spectral regions with similar scattering properties are grouped together. In our case the spectral separation is not intended to group together parts of the spectrum with common scattering properties. Rather, the spectral separation isolates the part of the shortwave spectrum dominated by ozone continuum absorption from the remainder of the shortwave spectrum.

The resulting fluxes and heating rates are much more accurate (Figs. 2.7d–l). For band 1 the maximum errors in the flux in the lowest layers of the atmosphere are less than 1% and heating rate errors are also small, being less than approximately 0.005 K/day (Figs. 2.7d–f). We were able to find a 5-point quadrature of the FSCK cumulative distribution functions for band 1 that led to nearly identical results with the 8192-point quadrature. That is, the FSCK treatment of gaseous

absorption in band 1 is accurate to approximately 3% of LBL heating rates and a 5-point quadrature for this band is possible without a significant loss of accuracy.

The band 2 comparisons (Figs. 2.7g–i) demonstrate that the assumption of vertical correlation is also valid for the spectral interval from 0.68–4.60  $\mu\text{m}$ , as the FSCK 8192-point quadrature flux and heating rate differences from the LBL results are less than 1% and 6%, respectively. However, for band 2, the quality of the FSCK results are highly dependent on the number of quadrature points. Using a 10-point quadrature, which represents a compromise between accuracy and computational efficiency, we found the heating rate errors in the troposphere to be less than 13%, while the errors in the stratosphere reached 66%. But, the consequence of the large percentage error in the stratosphere amounts to only a heating rate error of 1.1 K/day, which is small, i.e., less than 6%, when the total, full spectrum heating rate is considered (Figs. 2.7j–l). Overall, the 8192 quadrature-point FSCK method produced heating rates accurate to approximately 3.8% in the lowest 14 km and 3.0% for the full depth of the atmosphere. Limiting the two-band quadrature scheme to 5 points in band 1 and 10 points in band 2 led to larger full spectrum heating rate errors of 5.1% and 7.3% in the lowest 14 km and the full atmospheric depth, respectively.

Shifted Gauss-Chebyshev II quadrature (Wang and Modest 2004) is used to calculate the weights and abscissas for band 2 (Table 2.1). However, there is a sharp kink present in many of the cumulative  $k$ -distributions of band 1 near

**Table 2.1.** Trapezoidal quadrature abscissas and weights for band 1 and shifted Gauss-Chebyshev II quadrature abscissas and weights for band 2 before and after transformation.

Band 1		Band 2 before transformation		Band 2 after transformation	
Abscissa	Weight	Abscissa	Weight	Abscissa	Weight
0.453830	0.907660	0.000000	0.076046	0.000000	0.113893
0.929175	0.043030	0.156434	0.160133	0.225220	0.220272
0.962060	0.022740	0.309017	0.144407	0.425618	0.179779
0.981040	0.015220	0.453990	0.144940	0.596540	0.160402
0.994325	0.011350	0.587785	0.122105	0.735342	0.117413
		0.707107	0.116036	0.841487	0.094052
		0.809017	0.087385	0.916537	0.057194
		0.891007	0.076215	0.964017	0.037684
		0.951057	0.043742	0.989172	0.014493
		0.987688	0.028991	0.998634	0.004818

$g=0.95$  (not shown) that reduces the accuracy of Gaussian quadrature methods. As a result, we use trapezoidal quadrature for band 1 with weights and abscissas optimally selected to fit the LBL solution.

The next test case also consisted of the same clear-sky mid-latitude winter profile, but with molecular (i.e., “Rayleigh”) scattering and a Lambertian surface with gray albedo of 0.15 included in both the FSCK and LBL calculations. For the LBL calculations we used the spectrally-dependent Rayleigh scattering optical depths calculated according to Teillet (1990), while for the two-band FSCK calculations the Rayleigh scattering optical depths were calculated using the same technique but at fixed wavelengths of  $0.47 \mu\text{m}$  for band 1 and  $0.90 \mu\text{m}$  for band 2. In the FSCK calculations we also used the same 5- and 10-point quadrature values for bands 1 and 2 that we derived in the gas-absorption only case. Not

surprisingly, the flux and heating rate errors that we obtained for this case (Fig. 2.8a–c) do not differ in any significant way from those that we obtained for the gas-absorption only case. Moreover, results for clear-sky calculations in subarctic winter and tropical atmospheres are similar (not shown).

### 2.2.3 Cloudy Sky Calculations

The next two sets of test cases examine the accuracy of FSCK calculations in cloudy conditions. In the first case, an FSCK treatment of nongray cloud absorption with parameterized gray cloud scattering is evaluated, and in the second case, both gray cloud absorption and gray cloud scattering are parameterized. In both sets of calculations we consider the effects of low cloud, high cloud and both low and high clouds combined. The two sets of calculations differ in the method by which we account for cloud absorption in the FSCK calculations.

In the first set of calculations, where cloud absorption is nongray and cloud scattering is gray, we interpolated the  $0.01\text{-}\mu\text{m}$  resolution cloud absorption coefficients (Fig. 2.1b) to the spectral resolution of the gas coefficients in the two cloud layers and then added the interpolated cloud absorption coefficients to the gas absorption coefficients. The combined cloud and gas absorption coefficients were then sorted to form the cumulative  $k$ -distribution functions from which the final 5- and 10-point quadrature  $k$ -values for the radiative transfer were selected. The advantage of this approach is that spectral variations in the cloud absorption

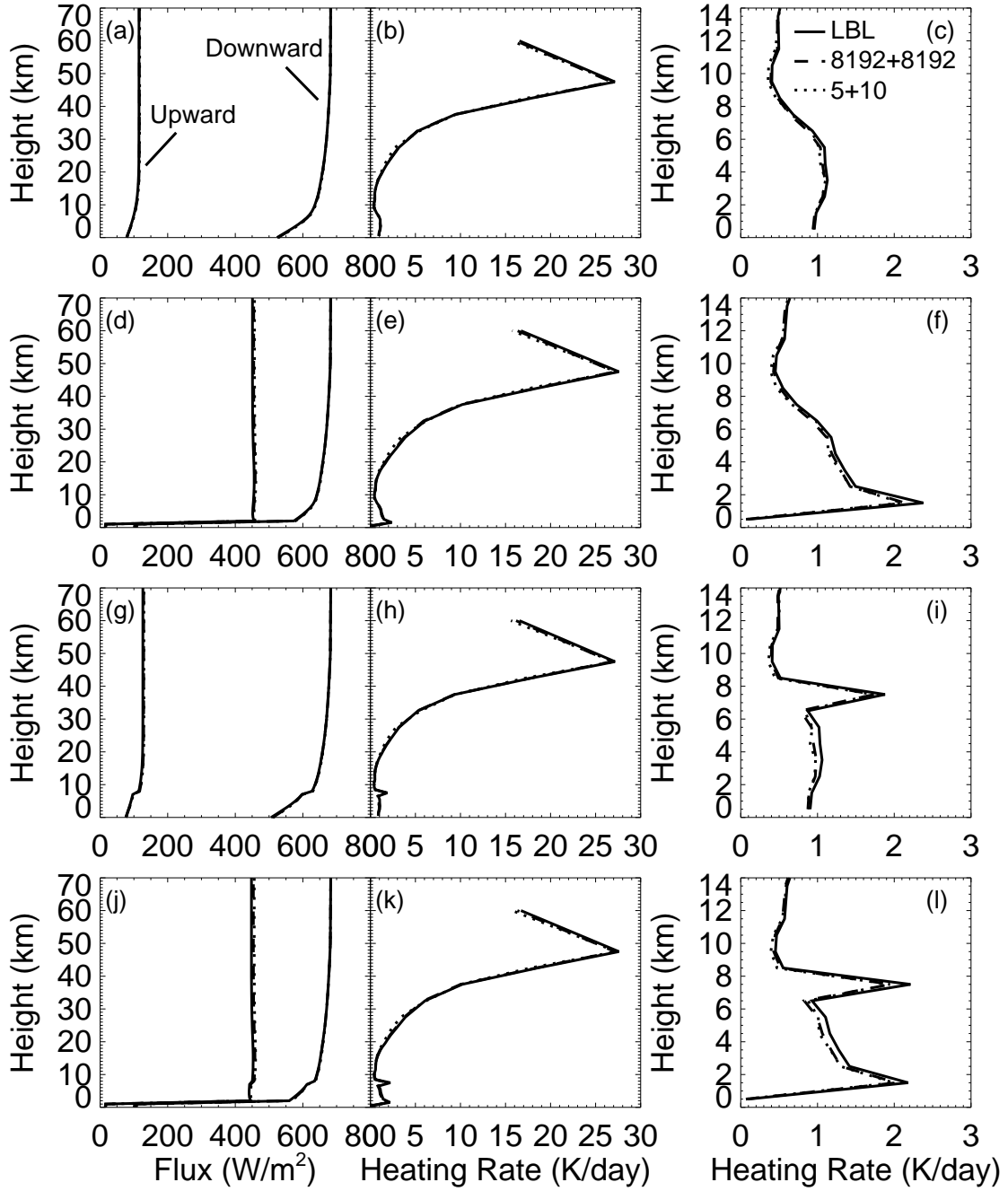


**Figure 2.8.** Upward and downward fluxes (a, d, g, and j), heating rates for all 29 layers (b, e, h, and k), and heating rates for the lowest 14 layers (c, f, i, and l) for (a–c) clear sky, (d–f) a liquid cloud with nongray absorption and gray scattering, (g–i) an ice cloud with nongray absorption and gray scattering, and (j–l) both clouds with nongray absorption and gray scattering. The LBL solution, the 8192 quadrature point solution, and the 15 quadrature point solution are given by the solid, dashed, and dotted lines, respectively.

coefficients are explicitly taken into account. The disadvantage to this approach is that adding the cloud absorption coefficients to the gas absorption coefficients leads to a partial loss of correlation in the  $k$ -distributions between the cloudy layers and their neighboring clear sky layers, as we illustrated in Fig. 2.2b–c.

The parameterized gray liquid- and ice-cloud asymmetry parameters, single-scattering albedos, and scattering cross sections used for this first set of nongray cloud absorption and gray cloud scattering calculations are shown in Table 2.2. We obtained these values by taking a band average of the fine-spectral-resolution Mie calculations weighted by spectrally-varying direct downwelling transmission at 500 hPa. The resulting parameters were fine-tuned by minimizing the flux errors between the 8192-point solution and the LBL calculations. Note that in this case nongray absorption by cloud drops is explicitly accounted for by the  $k$ -distributions, whereas absorption by cloud drops is typically accounted for by gray cloud extinction cross section and single-scattering albedo parameters. In order to avoid accounting for absorption by cloud drops twice, the gray cloud parameters are adjusted. First, the gray cloud parameter representing the extinction cross section is given the value of the scattering cross section; that is, the extinction cross section times the single-scattering albedo. Next, the single-scattering albedo is set to 1.0. This procedure essentially subtracts the gray cloud absorption cross section from the gray cloud extinction cross section.

As Figs. 2.8d–f illustrate for a low cloud and Figs. 2.8g–i illustrate for a high

**Table 2.2.** Asymmetry parameter,  $g$ , single-scattering albedo,  $\omega_0$ , and extinction cross section,  $\sigma_{ext}$ , for a lognormal distribution of liquid water spheres of radius  $5 \mu\text{m}$  and ice spheres of radius  $75 \mu\text{m}$  for band 1 ( $0.24\text{--}0.68 \mu\text{m}$ ) and band 2 ( $0.68\text{--}4.60 \mu\text{m}$ ), nongray absorption and gray scattering, and gray absorption and gray scattering.

	Band 1			Band 2		
	$g$	$\omega_0$	$\sigma_{ext}$	$g$	$\omega_0$	$\sigma_{ext}$
Nongray absorption and gray scattering						
Liquid	0.849	1.000	1.10e+02	0.825	1.000	9.40e+01
Ice	0.888	1.000	2.33e+04	0.898	1.000	2.35e+04
Gray absorption and gray scattering						
Liquid	0.856	0.999	1.10e+02	0.800	0.998	9.30e+01
Ice	0.867	0.999	2.32e+04	0.898	0.995	2.34e+04

cloud, maximum upward and downward flux errors were always less than 6% with typical errors near 1%, while the heating rate errors were generally less than 4% in the clear sky region above the highest cloud layer and no greater than 8–12% in and below the cloud layer. In both the low- and high-cloud cases the FSCK simulations with nongray cloud absorption and gray cloud scattering produced slightly less heating than the LBL calculations. The cloud parameters that we obtained for the single cloud-layer cases were used for the combined low- and high-cloud case, and results of that case were consistent with the single cloud-layer cases (Figs. 2.8j–l).

The likely source of error in this case of nongray cloud absorption is a breakdown in correlation between the cloud and surrounding clear-sky layers, as described in Section 2.1, and correlation could be partially restored by subdividing band 2

into more bands. However, we are attempting to balance accuracy with efficiency. Each additional band would require 5–10 additional quadrature points, and since the magnitude of the maximum in-cloud heating rate errors in this nongray cloud absorption case are of similar magnitude to heating rate errors of other state-of-the-art one-dimensional radiative transfer models relative to line-by-line calculations (Barker et al. 2003), we do not attempt to reduce further the two-band FSCK errors.

In the second set of calculations we treated the cloud absorption coefficients as gray within each band, in addition to gray scattering coefficients and asymmetry parameters. The values of the three parameterized gray cloud properties, i.e., asymmetry parameter, single-scattering albedo and extinction cross-section, were determined as described above for the gray cloud scattering properties in the first set of calculations, except that the gray cloud extinction cross sections and single-scattering albedos now account for cloud absorption. The tuning parameters for gray cloud absorption and gray cloud scattering are shown in Table 2.2.

As the results in Figs. 2.9a–c and d–f illustrate, values for the three coefficients exist that provide accurate fluxes, to better than 3%, and heating rates, to better than 2%, for each cloudy atmosphere. These results demonstrate that relatively accurate parameterization of single cloud-layer optical properties with gray values for the two bands is possible. Note that with three tuning parameters, i.e., asymmetry parameter, single-scattering albedo, and extinction coefficient, flux errors

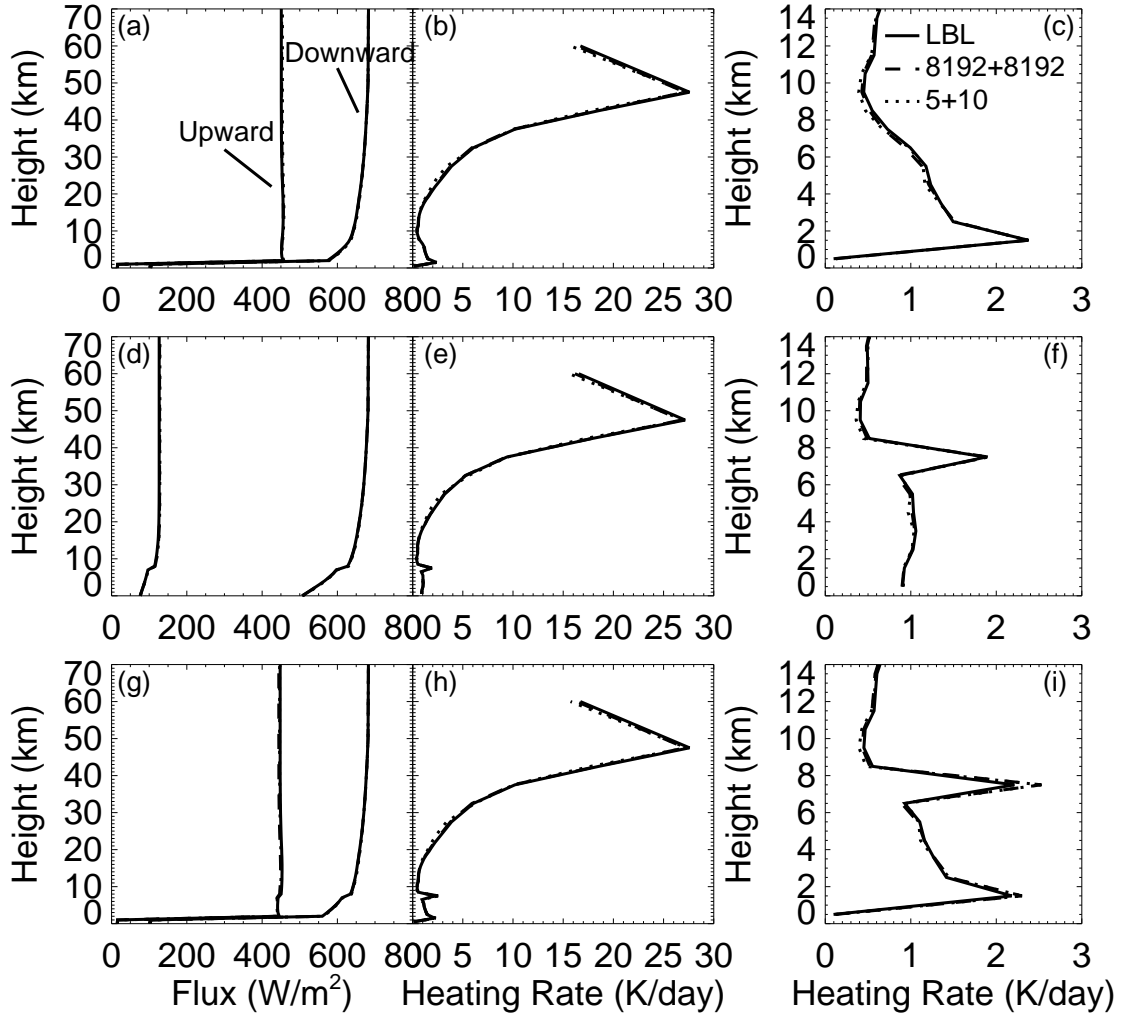


**Figure 2.9.** Upward and downward fluxes (a, d, and g), heating rates for all 29 layers (b, e, and h), and heating rates for the lowest 14 layers (c, f, and i) for (a-c) a liquid cloud with gray absorption and gray scattering, (d-f) an ice cloud with gray absorption and gray scattering, and (g-i) both clouds with gray absorption and gray scattering. The LBL solution, the 8192 quadrature point solution, and the 15 quadrature point solution are given by the solid, dashed, and dotted lines, respectively.

might be reduced more with a different combination of these parameters. If this gray cloud absorption and gray cloud scattering approach is further developed, sets of parameters must be determined for the range of cloud particle size distributions encountered in the numerical models in which the FSCK approach is implemented.

Incorporating the coefficients computed separately for the low and high clouds into a combined low and high cloud FSCK calculation produced flux and in-cloud heating rate errors of 1% and 6–14%, respectively, relative to the LBL results (Figs. 2.9g–i). The magnitudes of the in-cloud heating rate errors using this second approach are similar to those resulting from explicitly incorporating the nongray cloud absorption coefficients into the solar source function-weighted cumulative  $k$ -distributions, although the magnitudes and signs of the errors are less consistent from the single-layer to two-layer cloud cases than for the nongray cloud absorption calculations.

As we just demonstrated, the two sets of FSCK calculations for the mid-latitude winter atmosphere produced comparable results, with errors in the fluxes and heating rates of similar magnitudes. Performing identical sets of calculations for both the subarctic winter and tropical atmospheres, with the same quadrature points and cloud parameters derived for the mid-latitude winter atmosphere, we obtained results consistent with those from the mid-latitude atmosphere calculations.

## 2.2.4 Case Study Observations

The flux and heating rate results obtained in this case study demonstrate that the full spectrum correlated  $k$ -distribution (FSCK) method is an accurate and efficient alternative to line-by-line (LBL) calculations for shortwave atmospheric radiative transfer. By weighting  $k$ -distributions by the Planck function, or by the solar source function in the case of solar radiation, the FSCK method eliminates the requirement that the Planck function, or solar source function, be constant over the spectral intervals to be integrated. Consequently, a spectral band may be arbitrarily large in the FSCK approach, even encompassing the full spectrum, as long as the assumption of correlation in the gas absorption coefficients between regions of the atmosphere remains valid. As a result of the vertical distribution of absorbing gases in the atmosphere, primarily ozone and water vapor, the correlation assumption breaks down when the full shortwave spectrum is treated as a single band. However, the breakdown of correlation may be circumvented by separating the spectrum at  $0.68 \mu\text{m}$  into two bands, one band in which ozone continuum absorption is dominant and the other where it is less important relative to absorption by other gases.

Comparisons of two-band FSCK and LBL results indicate that the broadband FSCK clear-sky fluxes and heating rates are accurate to better than 1% and 3%, respectively, when 8192 quadrature points are used within each band. Limiting the first band from  $0.24\text{--}0.68 \mu\text{m}$  to 5 quadrature points and the second band

from 0.68–4.60  $\mu\text{m}$  to 10 quadrature points, the accuracies of the FSCK fluxes and heating rates become approximately 1% and 7%, respectively. For low- and high-altitude cloud test cases we found that gray cloud scattering for the two spectral bands with 5- and 10-point quadratures is sufficient to reproduce the LBL generated fluxes and heating rates, which used spectrally varying cloud absorption and scattering properties, to approximately 1% and 8%, respectively. Two different approaches to modeling absorption by cloud drops were examined. Explicitly including spectrally varying cloud absorption into the solar source function-weighted  $k$ -distributions resulted in realistic in-cloud heating rates, although the heating rates were consistently less than LBL calculated rates. Gray cloud absorption parameters that were chosen to optimally fit LBL results for one atmosphere but applied to different atmospheres or cloud combinations also closely approximated LBL in-cloud heating rates, although the heating rate errors were less consistent in magnitude and sign than for the first approach.

The FSCK solution requires only 15 quadrature points per layer, a 40–90% reduction in computational overhead from other correlated  $k$ -distribution models currently in use (e.g., Fu and Liou 1992; Mlawer and Clough 1997; Mlawer and Clough 1998; Kato et al. 1999). Hence, the FSCK method is potentially important to numerical modeling of radiative transfer, because the computational burden of the radiative transfer calculations is strongly linked to the number of spectral bands required. The next step in the application of the FSCK method to

shortwave atmospheric radiative transfer is to develop a robust radiative transfer module that may be used in operational numerical weather prediction or global climate models. Furthermore, direct comparisons between the FSCK method and current models will be required to determine the relative accuracy of the models. By explicitly accounting for spectral variability of the solar source function, the FSCK method has the potential for improving accuracy relative to traditional correlated  $k$ -distribution models which assume constant solar emission over each narrow band.

# Chapter 3

## Model Development for General Atmospheres

### 3.1 Design Considerations

To advance the FSCK model discussed in Chapter 2 from a model that can be applied to an atmosphere with pre-specified pressures, temperatures, mixing ratios, and cloud properties to an operational model that calculates fluxes and heating rates given any input atmospheric conditions, there are many factors to consider regarding model design. For the study discussed in Chapter 2 we knew the properties of each atmospheric layer beforehand. Therefore, we were able to retrieve absorption coefficients for mixtures of gases with pre-specified mixing ratios from LBLRTM and sort them to produce solar source function-weighted cumulative  $k$ -

distributions for each model layer. Subsequently, we used numerical quadrature to select values of the cumulative  $k$ -distributions to be used for integration of the radiative transfer equation. Since production of absorption coefficients using LBLRTM, sorting them into  $k$ -distributions, and summing them into cumulative  $k$ -distributions are computationally expensive procedures, these procedures cannot be performed in an operational model at runtime. Therefore, one must perform these procedures in advance, for selected pressures, temperatures, and mixing ratios, storing the resulting quadrature values of absorption coefficients in tables. When the operational model is running, interpolation is performed between stored values to absorption coefficients appropriate for the actual pressure, temperature, and mixing ratio values in each atmospheric layer.

Important considerations for implementing these procedures are the size and “shape” of the stored absorption coefficient table and the method of combining the optical properties of constituent species. The best methods for interpolating stored coefficients to the actual atmospheric state must also be established in the operational model. Each of these elements must be examined in the model design stage to balance accuracy and efficiency.

An example of the importance of the model design to modern Numerical Weather Prediction is the Weather and Research Forecasting (WRF) model (Michalakes et al. 2001). The design of this model was a cooperative venture amongst a number of major national and educational institutions. As such, the

WRF model is intended to be the next generation community model for operational and research use. With such a broad scope of applications, strict design standards must be adhered to for new algorithms implemented into the model. One such standard is that each physical parameterization be coded within a single module. In the case of our full-spectrum correlated  $k$ -distribution radiative transfer algorithm, the implication is that the absorption coefficient table cannot be stored in an external data table to be read by the parameterization at runtime — the table must be coded into data blocks and compiled within the code. The size of the table, which is now important, is determined by the number of pressures, temperatures, and constituent mixing ratios used to calculate the stored absorption coefficients.

The “shape” of the table is also important, where “shape” refers to the specific choice of pressures, temperatures, and constituent mixing ratios used to calculate the stored absorption coefficients. The magnitude of the separation between pressures, temperatures, and constituent mixing ratios contributes to the quality of the interpolation to the actual atmospheric state, especially for absorption coefficients not linearly related to the atmospheric state variables. Moreover, the range of pressures, temperatures, and constituent mixing ratios must encompass as many likely natural atmospheric states as possible to avoid extrapolation, which may introduce large errors. As a result, the table must be sufficiently large to minimize heating rate errors, yet it must not be so large as to prohibit its inclusion in the

WRF model.

We must also consider the method of combining the absorption coefficients of constituent species. The LBLRTM model produces absorption coefficients of individual gases in spectral space, but our radiative transfer calculations require absorption coefficients for gas mixtures in cumulative  $k$ -distribution, or  $g$ , space. Adding absorption coefficients of constituent species in spectral space is simple and accurate, although the individual gas concentrations are not known in advance within an operational model setting. Because orders of magnitude fewer points are involved in  $g$  space compared to spectral space, it may be possible to combine constituent  $g$ -space values within the run time of the numerical model. Because absorption by individual species may be correlated and one must account for overlapping absorption lines from different species, combining absorption coefficients in  $g$ -space requires care in order to avoid significant errors. Modest and Riazz (2004) address this topic at length, and we will discuss it further in Sections 3.2 and 3.3.

The method of interpolation must also be considered carefully, balancing accuracy against efficiency. Interpolating from a table of stored absorption coefficients calculated for predetermined pressures, temperatures and constituent mixing ratios requires interpolation in at least three, and possibly more, dimensions. While linear interpolation is relatively fast compared to higher order interpolations or spline techniques, the relative accuracies of the different methods depends on the

problem to which they are applied. Finding the appropriate method for a particular problem requires many “trial and error” studies. We briefly discuss in Sections 3.2 and 3.3 the motivation for the interpolation method that we adopted for our FSCK studies. In Section 3.4 we describe the size and shape of the correlated  $k$ -coefficient table that we developed, our method of combining constituent radiative properties, and the method of interpolation that we chose to create absorption and scattering coefficients suitable for general atmospheric conditions.

## 3.2 Precombined Gases with Gray Cloud

### Absorption

In Chapter 2 we extracted gas constituent properties from the HITRAN database and combined them in spectral space using LBLRTM, which accounts for line overlap and continuum absorption. In the calculations from Chapter 2 we created constituent radiative properties for the specific pressures, temperatures, and mixing ratios of the atmospheric profiles of interest. As mentioned in Section 3.1, in the case of an arbitrary atmospheric profile from an operational model, one does not know the values of the atmospheric state variables in advance. Moreover, the computational time of running LBLRTM and combining the resulting gas properties is far too expensive during the runtime of an operational numerical model. However, we can tabulate combined constituent  $k$ -values at any number

of values of pressure, temperature, and constituent mixing ratios and use them to interpolate to values for any arbitrary atmospheric profile.

If we adopt this precombined gas property approach, we must compute combined  $k$ -values for a sufficient number of combinations of pressures, temperatures and constituent mixing ratios to allow for reasonably accurate interpolated absorption coefficients. However, too many tabulated values may become too unwieldy to use in practice. For example, if we use the same gases that we used in Chapter 2 and store 15 double-precision  $k$ -values for each combination of, say, 15 pressures, 15 temperatures, and 15 mixing ratios for each of the seven gases, the resulting table will have a size of  $4.6 \times 10^{12}$  bytes. Using the same 15 double-precision quadrature points, if we also include combinations with nongray absorption coefficients for 15 cloud-liquid and 15 cloud-ice drop-size effective radii, the table increases in size to  $1.0 \times 10^{15}$  bytes!

One way to reduce the size of the table is to treat some gases as minor constituents, and to set their mixing ratio to a single “typical” value appropriate for each pressure and temperature combination. Major constituents are those gases with multiple mixing ratios for each pressure and temperature combination. Based on the preliminary results in Chapter 2, we treat water vapor as a major constituent in both band 1 and band 2, ozone as a major constituent in band 1 and a minor constituent in band 2, and carbon dioxide as a minor constituent in band 1 and a major constituent in band 2. Minor constituents in both band 1 and band 2

are carbon monoxide, methane, nitrous oxide, and oxygen. If we use 15 pressures, but reduce the number of temperatures to 10, the number of water vapor number concentrations to 13, the number of ozone mixing ratios in band 1 to 6, and the number of carbon dioxide mixing ratios in band 2 to 4, while further limiting the size of the table by treating cloud absorption as gray, i.e., making a separate table for cloud optical properties that is independent of pressure and temperature with one value per band for each lognormal drop-size distribution, the gas absorption coefficient table is reduced to a more reasonable  $1.1 \times 10^6$  bytes. With this framework in mind we construct Table 3.1 based loosely on the procedure described by Kato et al. (1999). Also shown in Table 3.1 are effective radii of lognormal drop-size distributions of liquid and ice clouds used to calculate gray cloud scattering properties and gray or nongray cloud absorption independent of other state variables.

The units of gas concentration used to tabulate  $k$ -values for different gas species requires a short explanation. Carbon dioxide, nitrous oxide, carbon monoxide, methane, and oxygen are all fairly well-mixed atmospheric gases, so mixing ratio (in units of parts per million by volume, [ppmv]) is a natural unit to describe their variation through the atmospheric profile. The full range of typical mixing ratio values for these gases can be resolved adequately with only a few values. On the other hand, water vapor concentrations vary significantly through the atmospheric profile, so many values of mixing ratio are necessary to adequately resolve the

**Table 3.1.** Atmospheric state variables, combinations of which are used to calculate tabulated  $k$ -values. Also shown are effective radii of a lognormal distribution of liquid- and ice-cloud drops used to calculate gray cloud scattering properties and gray or nongray cloud absorption.

$p$ [hPa]	$T$ [K]	$q_{\text{H}_2\text{O}}$ [\# $\text{m}^{-3}$ ]	$q_{\text{CO}_2}$ [ppmv]	$q_{\text{O}_3}$ [ppmv]	$q_{\text{N}_2\text{O}-\text{CO}-\text{CH}_4-\text{O}_2}$	$r_{\text{liquid}}$ [ $\mu\text{m}$ ]	$r_{\text{ice}}$ [ $\mu\text{m}$ ]
1050.0	120.0	1.50e+25	340	1.0e-04	A single	0.5	0.5
834.0	142.2	3.23e+24	375	1.0e-03	appropriate	1.0	1.0
662.0	164.4	6.96e+23	410	1.0e-02	mixing ratio	2.5	2.5
526.0	186.7	1.50e+23	750	1.0e-01	is assigned to	5.0	5.0
418.0	208.9	3.23e+22		1.0e+00	each gas for	7.5	7.5
320.0	231.1	6.96e+21		1.0e+01	each combination	10.0	10.0
240.0	253.3	1.50e+21			of pressure	15.0	15.0
165.0	275.6	3.23e+20			and temperature	20.0	20.0
106.0	297.8	6.96e+19				25.0	25.0
67.0	320.0	1.50e+19				35.0	35.0
42.0		1.50e+16				50.0	50.0
24.0		1.50e+13				100.0	100.0
8.0		1.50e+10				250.0	250.0
1.5						500.0	500.0
0.1						1000.0	1000.0
(15)	(10)	(13 - Bands 1 & 2)	(4 - Band 2)	(6 - Band 1)	(1)	(15)	(15)

full range of water vapor mixing ratios, regardless of units chosen. We would have been more consistent had we chosen to tabulate water vapor mixing ratios in units of [ppmv]. However, as mentioned, we based our table on the earlier work of Kato et al. (1999), in which water vapor is tabulated for fixed values of number concentration (in units of number of molecules per cubic meter,  $[m^{-3}]$ ). Since number concentration is the most appropriate unit for radiative transfer, and in fact all other units of constituent concentration must be converted to number concentration to calculate absorption coefficients, we tabulate water vapor  $k$ -values for fixed values of number concentration in units of  $[m^{-3}]$ , thus eliminating the need for unit conversion at model runtime. Ozone is neither as well mixed as the minor constituents, nor as variable as water vapor. Consequently we tabulate  $k$ -values for ozone based on fixed values of [ppmv], but use more mixing ratios than the minor constituents to resolve the typical range of ozone mixing ratios.

To interpolate from stored absorption coefficients associated with Table 3.1 to the atmospheric state of interest requires interpolation in four dimensions, i.e., pressure, temperature, water vapor number concentration, and the mixing ratio of either ozone for band 1 or carbon dioxide for band 2.

In this chapter we use only linear interpolations for simplicity and efficiency, since higher-order interpolations, while likely to improve accuracy, are certain to reduce efficiency, especially if applied to this four-dimensional problem. Similarly, cubic spline interpolations would likely improve accuracy, but cubic spline algo-

rithms for more than one dimension are computationally expensive, as well. In this chapter we determine the error introduced by interpolating tabulated absorption coefficients to an atmospheric profile of interest by applying linear interpolations. In Chapter 4, we assess whether or not the magnitude of the interpolation error is acceptable relative to state-of-the-art operational and research models. If it is not acceptable, future research on FSCK atmospheric applications will have to consider implementing a higher-order or cubic-spline interpolation scheme, or perhaps a hybrid interpolation scheme, to improve accuracy.

Note that a four-dimensional linear interpolation does not require 4 linear interpolations for each quadrature point of each layer; rather, it requires 15 linear interpolations, i.e., 8 interpolations in pressure, 4 in temperature, 2 in water vapor number concentration, and 1 in the mixing ratio of the other major gas.

In order to determine the error introduced by interpolating tabulated absorption coefficients to an atmospheric profile of interest using linear interpolations, we compare the heating rates resulting from the use of our table of precombined  $k$ -values to the heating rates produced from absorption coefficients computed from the precise properties of the atmospheric profile of interest, which we call the “hardwired” atmosphere. We generate 2-band, 15 quadrature-point solutions for both the interpolated and “hardwired” absorption coefficients and use the “hardwired” results as the standard for evaluating the results based on interpolation. This approach allows us to quantify the errors produced by the interpolation procedure,

as opposed to quantifying the loss of accuracy relative to LBL results produced by the use of the FSCK algorithm itself. We have already investigated the latter type of errors in Chapter 2.

We evaluate our interpolation scheme using the CLEAR, CLOUD A, and CLOUD B cases in the model intercomparison study of Barker et al. (2003). The atmospheric thermodynamic profile is the tropical atmosphere of McClatchey et al. (1972) with 62 layers from the surface to approximately 70 km. The surface albedo is set to 0.20. In the CLOUD A case, the layer between 3.5 km and 4.0 km contains a uniform overcast cloud with a cloud water mixing ratio of  $q_c = 0.159 \text{ g kg}^{-1}$ . The cloud water is modeled as lognormally distributed pure liquid water spheres with an effective radius of  $r_{\text{eff}} = 10 \text{ }\mu\text{m}$ . The visible optical depth that results is  $\sim 10$ . The CLOUD B case uses the same cloud-drop size distribution as for the CLOUD A case, but fills the layer between 10.5 km and 11.0 km with a uniform overcast cloud having a cloud water mixing ratio of  $q_c = 0.034 \text{ g kg}^{-1}$  for a visible optical depth of  $\sim 1$ .

As the results in Fig. 3.1a demonstrate, there is some reduction in the accuracy of clear-sky heating rates due to interpolation. The maximum clear-sky heating rate errors relative to the 15-point hardwired solution are less than 10% when the 15-point hardwired solution heating rate has a value greater than about 1 K/day. Heating rate errors don't exceed 5% below 7 km. Maximum heating rate errors are approximately 13% at the top of the atmospheric profile (not shown). The FSCK

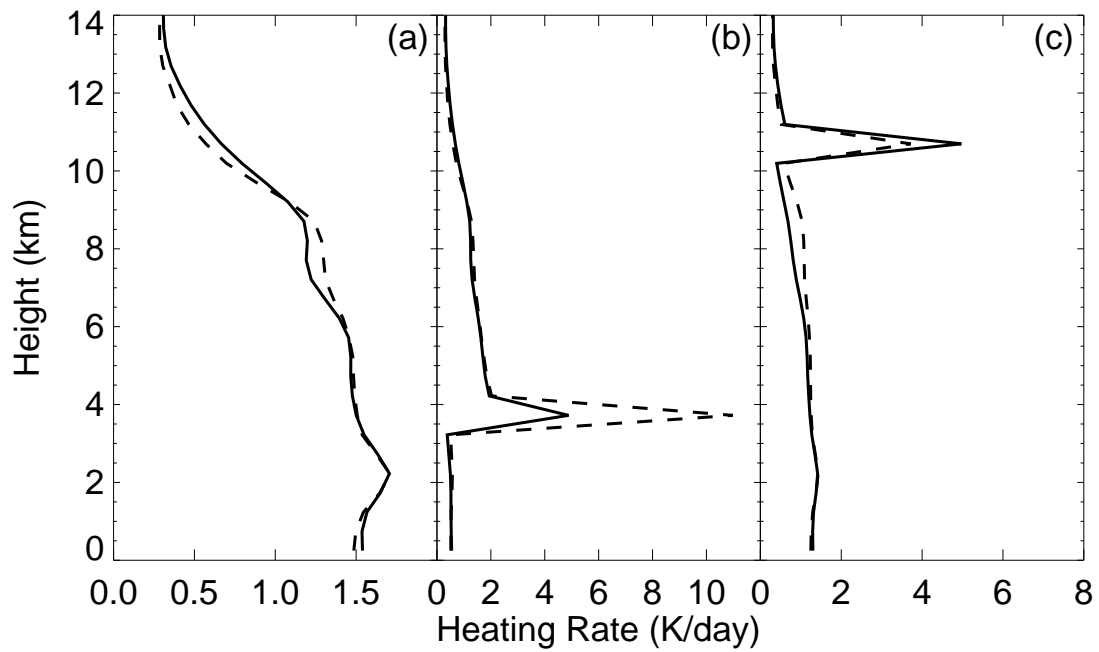


**Figure 3.1.** Broadband heating rates (K/day) for the FSCK 15-point hardwired solution (solid) and FSCK calculations using precombined gases with gray cloud absorption (dashed) for the (a) CLEAR, (b) CLOUD A, and (c) CLOUD B cases of Barker et al. (2003).

results for the CLOUD A and CLOUD B cases are less promising here, as compared to the results in Chapter 2, when gray cloud optical properties are used in the simulations. We computed gray cloud optical properties using Mie theory applied to the Barker et al. (2003) cloud-drop distributions. Unfortunately, we could not reduce our two-band Mie results to a single set of parameters (i.e., extinction cross section, single-scattering albedo, and asymmetry parameter) that could accurately reproduce both the CLOUD A and CLOUD B LBL results. We could tune the gray parameters to accurately model either of the clouds, but parameters tuned for one cloud are inappropriate for the other. The implication of this result is that any operational scheme would minimally have gray cloud parameters that are a function of both cloud-particle size and their vertical location within the atmosphere. Such a scheme is not practical to implement. Based on these results we do not develop further the use of gray cloud optical properties for the two-band application of the FSCK method.

### **3.3 Gases Combined On-the-Fly with Nongray Cloud Absorption**

We now explore the advantages and disadvantages of another approach to tabulating absorption coefficients. Rather than using LBLRTM to combine absorption coefficients of constituent gases in spectral space prior to sorting into  $k$ -distributions,

we extract and sort the absorption coefficients of each individual gas. We then save the  $k$ -values at 15 quadrature points for each gas and set of state variables, thereby creating an absorption coefficient table for each gas. We also create nongray absorption coefficient tables for lognormally distributed cloud liquid- and ice-particle size distributions with a range of effective radii in the same manner as for the gases. We subsequently combine the gas and cloud particle absorption coefficient  $k$ -values on-the-fly using the method of Modest and Riazzi (2004). The justification for using this method of combining nongray cloud absorption and gas absorption is discussed in Section 3.4. Here, we use two different implementations of this method: we combine all of the constituents simultaneously (Section 3.3.1) and we combine the constituents serially (Section 3.3.2).

Because the constituents properties are not combined for various mixing ratios of each constituent, the tables of stored coefficients are significantly smaller in size for this approach. The  $k$ -value tables for each constituent are at most three-dimensional, with axes of pressure, temperature, and gas mixing ratio given in Table 3.1. Because the tables are smaller, we treat water vapor, ozone, and carbon dioxide as major gases in both band 1 and band 2, where each gas is indexed by pressure, temperature, and its own mixing ratio. We treat carbon monoxide, methane, nitrous oxide, and oxygen as minor constituents for both bands, so their  $k$ -value tables are two-dimensional, indexed only by pressure and temperature. The nongray absorption coefficient tables for cloud-liquid and cloud-ice particles

are one-dimensional, being indexed only by effective radius. We use these same  $k$ -value tables whether we combine constituents simultaneously or serially.

As an alternate implementation, ozone, carbon dioxide, and the other minor gas constituent  $k$ -values could be calculated for a single pressure, temperature, and mixing ratio combination. The resulting  $k$ -values could then be scaled as a function of pressure, temperature, and mixing ratio, because there is no significant self-broadening associated with these gases. However, although scaling of  $k$ -values for these gases would likely be more efficient than interpolating from tabulated values calculated for specific pressures, temperatures, and mixing ratios, we adhere to the current implementation to avoid introducing additional complexity at this stage of development. We leave the development and evaluation of scaling functions to subsequent research.

Because the  $k$ -tables for the individual constituents are of a lower dimension than the  $k$ -table for precombined gases, interpolation from tabular state variables to the atmospheric state of interest is also performed at a lower dimension. However, this does not imply fewer interpolations. In the case of precombined gases with gray cloud absorption, we performed 15 linear interpolations for each quadrature point at each atmospheric layer. Now we require 7 linear interpolations (i.e., 4 for pressure, 2 for temperature, and 1 for mixing ratio) for each major constituent and 3 linear interpolations (i.e., two for pressure and 1 for temperature) for the remaining minor constituents. Altogether, we now have a total of 24 linear inter-

polations for each quadrature point of each layer. An additional interpolation is necessary for layers containing either a liquid or an ice cloud, while 2 additional interpolations are necessary for layers with a mixed-phase cloud.

### 3.3.1 Constituents Combined Simultaneously

The method that we chose to combine tabulated  $k$ -values obtained from constituent specie cumulative  $k$ -distributions was adapted from Modest and Riazzi (2004). The derivation of the Modest and Riazzi (2004) method is included here for the convenience of the reader.

Taine and Soufiani (1999) have shown that the product of the transmissivities  $\tau_i$  of  $n_i$  individual gas species, i.e.,

$$\tau_{\text{mix}} \cong \prod_{i=1}^{n_i} \tau_i, \quad (3.1)$$

can accurately reproduce direct LBL transmissivities for the mixture. This is true as long as the monochromatic transmissivities, and hence absorption coefficients, of the constituent species are statistically uncorrelated across the spectral interval for which the  $\tau_i$  are computed. Modest and Riazzi (2004) extended Eq. (3.1) to a method of mixing cumulative  $k$ -distributions from gas species with uncorrelated absorption coefficients. Modest and Riazzi (2004) note that the definition of

transmissivity in terms of the  $k$ -distribution for a single absorbing specie,

$$\tau_i = \int_0^\infty e^{-k_i L} f_i(k) dk_i, \quad (3.2)$$

is also the definition of the Laplace transform of  $f_i(k)$ . Using Eqs. (3.1) and (3.2), the transmissivity  $\tau_{\text{mix}}$  of a mixture of  $k$ -distributions may be expressed as the product of the Laplace transforms of the constituent  $k$ -distributions:

$$\tau_{\text{mix}} = \mathcal{L}[f_{\text{mix}}(k)] = \prod_{i=1}^{n_i} \mathcal{L}[f_i(k)]. \quad (3.3)$$

In terms of the cumulative  $k$ -distribution the transmissivity of an individual constituent is

$$\tau_i = \int_0^1 e^{-k_i L} dg_i. \quad (3.4)$$

For a mixture of two constituents this becomes

$$\begin{aligned} \tau_{\text{mix}} &= \mathcal{L}[f_{\text{mix}}(k)] = \int_0^1 e^{-k_1 L} dg_1 \int_0^1 e^{-k_2 L} dg_2 \\ &= \int_{g_1=0}^1 \int_{g_2=0}^1 e^{-[k_1(g_1)+k_2(g_2)]L} dg_2 dg_1, \end{aligned} \quad (3.5)$$

where  $k_1$  and  $k_2$  are  $k$ -values for constituents 1 and 2, respectively. Modest and

Riazzi (2004) use the integral property of the Laplace transform to obtain

$$\begin{aligned} \mathcal{L}\left[\int_0^k f_{\text{mix}}(k)\right] &= \mathcal{L}[g_{\text{mix}}(k)] = \left(\int_{g_1=0}^1 \int_{g_2=0}^1 e^{-[k_1(g_1)+k_2(g_2)]L} dg_2 dg_1\right) \frac{1}{L} \\ &= \int_{g_1=0}^1 \int_{g_2=0}^1 \frac{e^{-[k_1(g_1)+k_2(g_2)]L}}{L} dg_2 dg_1. \end{aligned} \quad (3.6)$$

When the inverse Laplace transform of Eq. (3.6) is taken we have

$$g_{\text{mix}}(k_{\text{mix}}) = \int_{g_1=0}^1 \int_{g_2=0}^1 H[k_{\text{mix}} - (k_1 + k_2)] dg_2 dg_1, \quad (3.7)$$

where  $k_{\text{mix}}$  is a threshold value from an array of  $k$ -bins constructed to encompass the full range of  $k$ -values for the two constituents to be combined in a model layer and  $dg_1$  and  $dg_2$  are the quadrature weights associated with  $k_1$  and  $k_2$ . In Eq. (3.7)  $H$  is the Heaviside step function given by

$$H = \begin{cases} 1 & \text{for } k_1 + k_2 < k_{\text{mix}} \\ 0 & \text{for } k_1 + k_2 \geq k_{\text{mix}}. \end{cases} \quad (3.8)$$

The function  $g_{\text{mix}}$  represents the cumulative  $k$ -distribution of the mixture to be constructed from the  $k$ -values for each of the constituent gases.

Modest and Riazzi (2004) construct the array of  $k$ -bins for the mixture,  $k_{\text{mix}}$ , using a power distribution:

$$\Delta[(k_{\text{mix}})^q] = [(k_{\text{max}})^q - (k_{\text{min}})^q]/(N_{k_{\text{mix}}} - 1), \quad (3.9)$$

and

$$(k_{\text{mix}_i})^q = (k_{\text{min}})^q + i\Delta[(k_{\text{mix}})^q] \quad (i = 0, \dots, N_{k_{\text{mix}}}), \quad (3.10)$$

where  $q$  is an exponential factor set to 0.095,  $k_{\text{min}}$  is the sum of the minimum quadrature values of the two constituents in the model layer, and  $k_{\text{max}}$  is the sum of the maximum quadrature values of the two constituents in the model layer. The number of  $k$ -bins,  $N_{k_{\text{mix}}}$ , is important to the accuracy of  $g_{\text{mix}}$  reconstructed from the values of  $k_1$  and  $k_2$ . The finer the resolution in  $k_{\text{mix}}$ , the more precisely the original quadrature values will be captured in the new distribution.

To combine  $i$  constituents Modest and Riazzi (2004) use a simple generalization of Eq. (3.7):

$$g_{\text{mix}}(k_{\text{mix}}) = \int_{g_1=0}^1 \dots \int_{g_i=0}^1 H[k_{\text{mix}} - (k_1 + \dots + k_i)] dg_i \dots dg_1. \quad (3.11)$$

The Heaviside step function is now defined as

$$H = \begin{cases} 1 & \text{for } k_1 + \dots + k_i < k_{\text{mix}} \\ 0 & \text{for } k_1 + \dots + k_i \geq k_{\text{mix}}. \end{cases} \quad (3.12)$$

We still compute the  $k$ -bins using Eqs. (3.9) and (3.10), but with  $k_{\text{min}}$  and  $k_{\text{max}}$  obtained from summing over all constituent minimum and maximum quadrature values, respectively.

As a result of the nested integrals in Eq. (3.11), the innermost loop will be

repeated  $N_{k_{\text{mix}}} \times N_{k_1} \times \dots \times N_{k_i}$  times, where  $i$  is the number of constituents and  $N_{k_i}$  is the number of quadrature points for the  $i^{\text{th}}$  constituent. In our case, since each of the constituents have the same number of quadrature points, the innermost loop will repeat  $N_{k_{\text{mix}}} \times (N_{k_{\text{band}}})^i$  times for each spectral band, where  $N_{k_{\text{band}}}$  is the number of quadrature points for each spectral band. To achieve reasonable accuracy we choose  $N_{k_{\text{mix}}} = 200$ . For 5 quadrature points for band 1, 10 quadrature points for band 2, and  $i = 6$  constituents, which includes the three major gases, the minor gases treated together as a single constituent, and cloud liquid- and ice-water particles, the innermost loop will repeat approximately  $2.0 \times 10^8$  times.

In our application, we first construct a new cumulative  $k$ -distribution for the mixture,  $g_{\text{mix}}$ , at a specified set of  $k_{\text{mix}}$  values. In order to use the 15 quadrature points we chose in Chapter 2 we must invert the array  $g_{\text{mix}}(k_{\text{mix}})$  to  $k_{\text{mix}}(g_{\text{mix}})$  and interpolate the values of  $k_{\text{mix}}$  to our known  $g$ -values (see Table 2.1). This procedure requires another interpolation for each quadrature point in each layer.

The heating rates for the Barker et al. (2003) atmospheric profiles resulting from combining gases on-the-fly simultaneously with nongray cloud absorption are shown in Fig. 3.2. The heating rate errors are as high as 33% for the CLEAR case relative to the 15-point hardwired solution in the lowest 10 km, but are less than 10% below 7 km. This approach results in a 44%, or 2.2 K/day, in-cloud error in the CLOUD A case and a 5%, or 0.25 K/day, in-cloud error in the CLOUD B case.

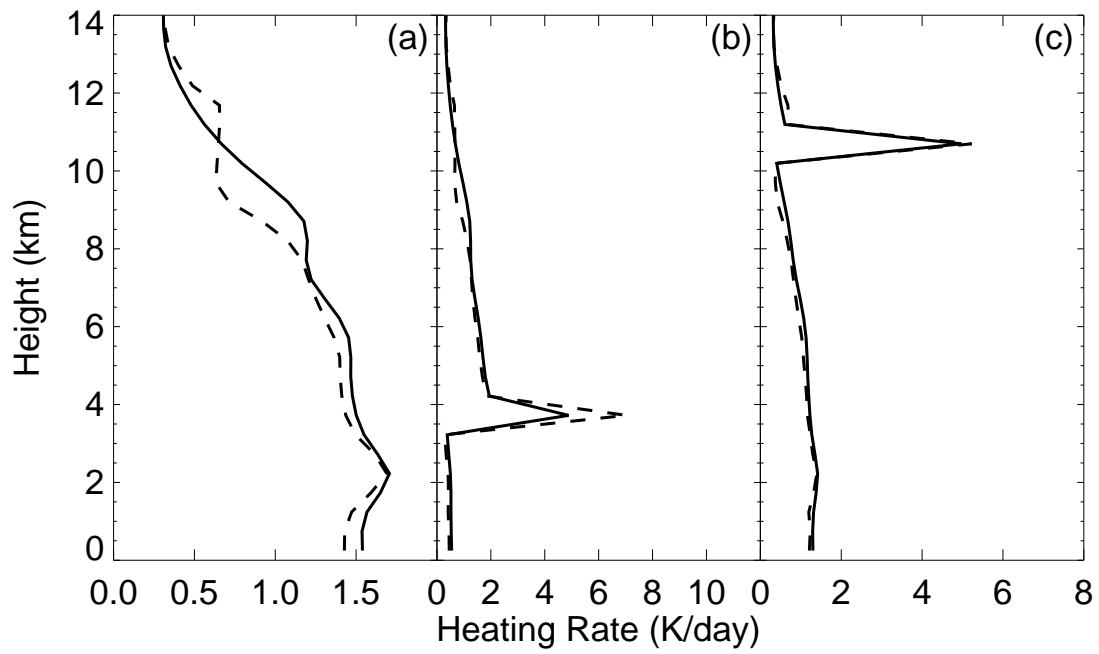


**Figure 3.2.** Broadband heating rates (K/day) for the FSCK 15-point hardwired solution (solid) and FSCK calculations using gases and nongray cloud absorption combined on-the-fly simultaneously (dashed) for the (a) CLEAR, (b) CLOUD A, and (c) CLOUD B cases of Barker et al. (2003).

One possible source of error present in this approach, which is not present in the precombined gas approach, is in the interpolation of individual gas absorption coefficient  $k$ -values, rather than the mixture absorption coefficient  $k$ -values, from tabulated states to the desired atmospheric state. The additional interpolations necessary in the process of combining gases, i.e., interpolating values of  $k_{\text{mix}}$  from corresponding  $g_{\text{mix}}$ -values onto our 15 quadrature points, may introduce additional errors. Also, it is possible that error is introduced by the mixing method itself, because it assumes absorption coefficients of the component gases are statistically uncorrelated, which may not be the case. Notwithstanding all of these errors, in-cloud absorption is more accurate with the current treatment of combining nongray cloud absorption coefficients with those of the gases.

### 3.3.2 Constituents Combined Serially

A slightly different implementation of the approach outlined in Section 3.3.1 is possible. Rather than combining the constituents simultaneously through Eq. (3.11), we simply apply Eq. (3.7) repeatedly. That is, we combine the first two constituents and reassign the resulting mixture to  $k_1$ . We then reapply Eq. (3.7) to the two-constituent mixture as  $k_1$  and the  $k$ -values of the next constituent as  $k_2$ .

One advantage of this approach is computational efficiency. As the number of constituents increases, the computational benefit of the serial approach over

the simultaneous approach also increases. Because there are only two integrals in Eq. (3.7), the innermost loop will be repeated  $(i - 1) \times N_{k_{\text{mix}}} \times (N_{k_{\text{band}}})^2$  times, where again  $i$  is the number of constituents. Because of the improved computational efficiency of this method, we increase  $N_{k_{\text{mix}}} = 2000$  to improve the accuracy of the combination process. For our six constituents (i.e., three major gases, the minor gases treated together as a single constituent, and cloud liquid- and ice-water particles), the innermost loop will repeat only  $1.2 \times 10^6$  times rather than the  $2.0 \times 10^8$  times required for simultaneous combination of six constituents.

Another advantage of this approach is that it is trivial to add more constituents. As a result, adding additional gases as major constituents or even aerosols, requires only the addition of the new constituent  $k$ -tables to the iteration process. The flexibility of this approach would certainly be advantageous in the design of a radiative transfer module that can fully interact with an online atmospheric chemistry model. A disadvantage is an increase in the number of interpolations. Each time two constituents are combined, the resulting  $g_{\text{mix}}(k_{\text{mix}})$  must be inverted and  $k_{\text{mix}}(g_{\text{mix}})$  must be interpolated to our 15 quadrature-point values.

The heating rates resulting from combining gases on-the-fly serially with nongray cloud absorption are illustrated in Fig. 3.3. The heating rate errors are less than 26% relative to the 15-point hardwired solution for the CLEAR case in the lowest 10 km, with a 34% in-cloud error in the CLOUD A case and a 7% in-cloud error in the CLOUD B case. Differences in the results between the se-

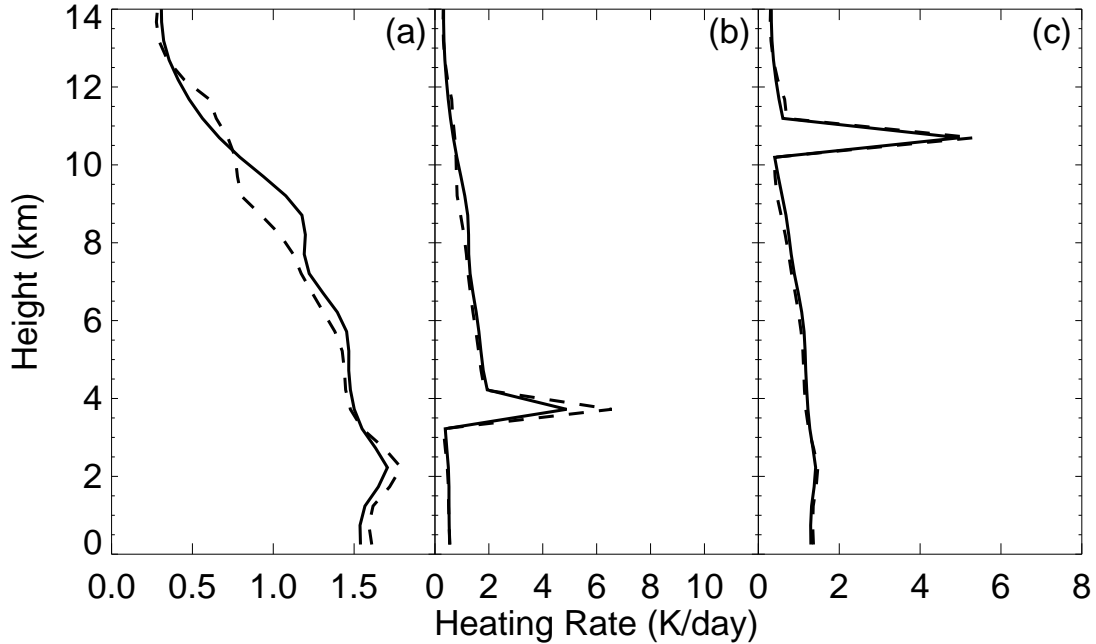


**Figure 3.3.** Broadband heating rates (K/day) for the FSCK 15-point hardwired solution (solid) and FSCK calculations using gases and nongray cloud absorption combined on-the-fly serially (dashed) for the (a) CLEAR, (b) CLOUD A, and (c) CLOUD B cases of Barker et al. (2003).

rial and the simultaneous combination approaches are numerical in origin. The bin resolutions of  $k_{\text{mix}}$  are different and the threshold values of  $k_{\text{mix}}$  in Eqs. (3.7) and (3.11) are met in a different sequence in the two approaches. Another reason for differences between the serial- and simultaneous-combination approaches is the varying number of interpolations to the final 15 quadrature points.

### 3.4 The Way Forward

Of the three approaches discussed in this chapter, the clear-sky heating rate errors were the smallest for the precombined gas approach. Whether this is the result of

explicitly accounting for line overlap by combining the absorption coefficients in spectral space prior to sorting or the fewer interpolations necessary to use tabulated values for a specific model layer, this approach appears to be the most accurate for clear-sky calculations. However, when we used this method with gray cloud properties, in-cloud heating rate errors exceeded 125%. As mentioned in Section 3.2, if we include nongray cloud absorption in the precombined mixtures, the size of the precombined  $k$ -table will become unmanageable.

A compromise approach is one that uses precombined gases, but combines nongray cloud absorption on-the-fly. In this approach we use the same clear-sky table developed in Section 3.2, but we add nongray cloud absorption in cloudy atmospheric layers serially using Eq. (3.7).

An underlying assumption of the method we chose to combine constituents, described in Section 3.3.1, is that the constituents must have absorption coefficients that are statistically uncorrelated. However, the absorption coefficients of cloud drops and atmospheric gases, including water vapor, may not be entirely uncorrelated. Therefore, there is no clear theoretical basis for applying Eq. (3.7) to the combination of cloud absorption coefficients. To determine whether or not the method embodied in Eq. (3.7) is appropriate for this purpose we compare FSCK band 2 transmissions for a non-scattering layer of a clear-sky gas mixture, an absorbing, but not scattering, cloud with a lognormal distribution of liquid cloud drops with effective radius of 10  $\mu\text{m}$  and a varying cloud-drop number con-

centration, a cloud-gas mixture whose absorption coefficients have been combined monochromatically and the product of the clear-sky gas mixture and cloud band 2 transmissions (Fig. 3.4b). The near infrared (wavelengths  $1.0 \mu\text{m}$  and  $3.0 \mu\text{m}$ ) cloud absorption optical depths resulting from the variation of cloud-drop number concentration are shown in Fig. 3.4a, and the percent error between the product of clear-sky and cloud transmissions relative to the transmission of the clear- and cloudy-sky mixture is shown in Fig. 3.4c.

As Fig. 3.4c illustrates, errors in the product of constituent transmissions are less than 10% for concentrations less than  $86 \text{ cm}^{-3}$  and remain less than 15% for concentrations less than  $1000 \text{ cm}^{-3}$ . We expect these errors to be representative of other cloud-drop effective radii, as well as for ice clouds and clouds embedded in air with slightly different gas concentrations. Based on the magnitude of these errors we proceed to use the method of combination described in Section 3.3.1.

The heating rates resulting from the use of precombined gases with nongray cloud absorption added on-the-fly serially are shown in Fig. 3.5. The resulting errors are less than 13% for the CLEAR case relative to the 15-point hardwired solution when the 15-point hardwired solution heating rate is greater than about 1 K/day. When the 15-point hardwired solution heating rate is less than about 1 K/day, the absolute error does not exceed 0.1 K/day. The in-cloud error in the CLOUD A case is 25% and is 6% in the CLOUD B case. This approach is the one that we use in comparison of the FSCK method with state-of-the-art operational

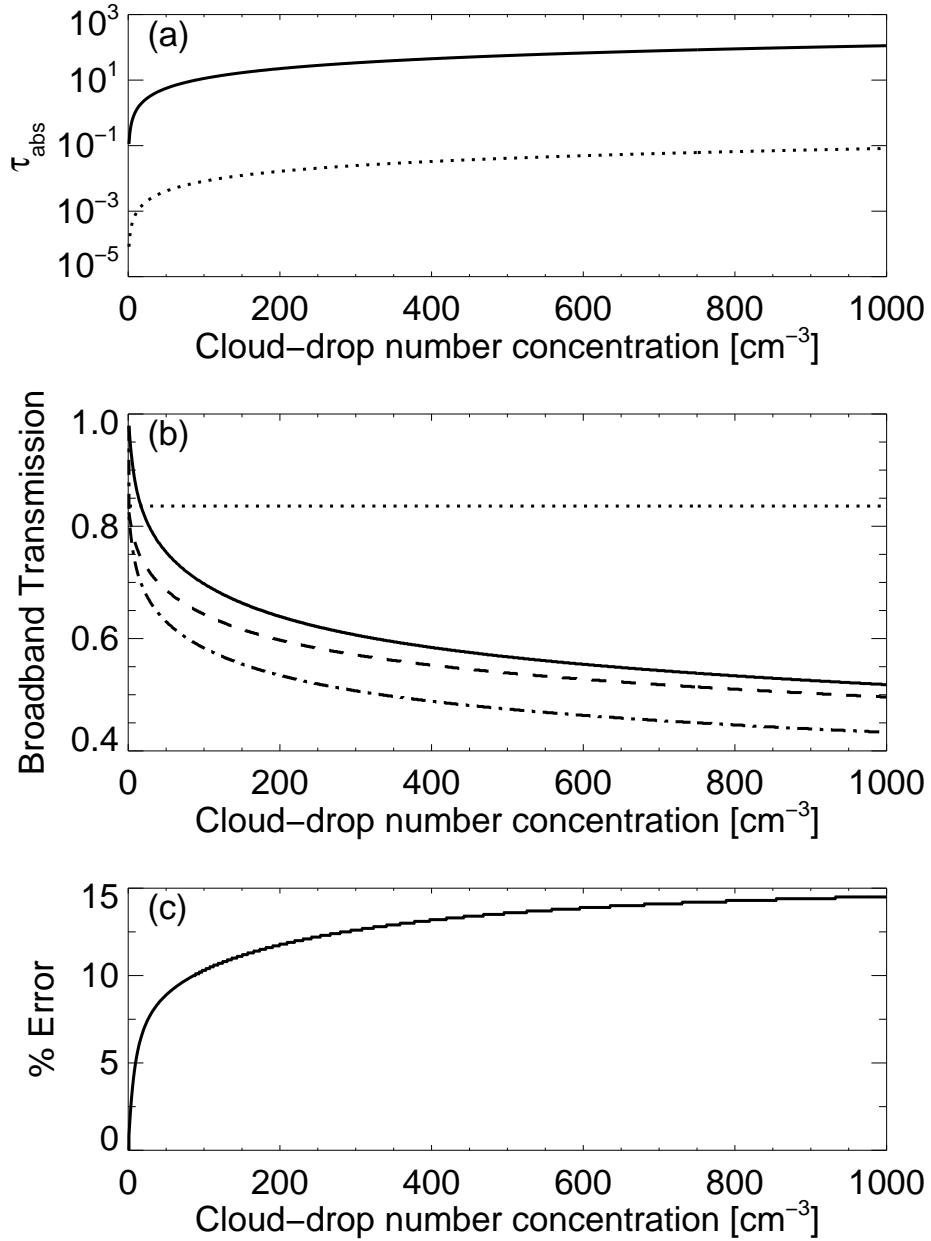


**Figure 3.4.** (a) Near infrared (wavelength  $1.0 \mu\text{m}$  dotted, and wavelength  $3.0 \mu\text{m}$  solid) absorption optical depths for a lognormal distribution of liquid-water cloud drops with effective radius of  $10 \mu\text{m}$  as a function of number concentration. (b) Broadband near infrared transmission for a non-scattering layer consisting of a clear-sky gas mixture (dotted), a lognormal distribution of liquid-water cloud drops with effective radius of  $10 \mu\text{m}$  (solid), and a mixed gas-cloud layer (dashed) as a function of number concentration. The product of the gas-mixture and cloud broadband transmissions is represented by the dash-dot line. (c) Percent error of the product of the clear-sky gas mixture and cloud broadband transmissions relative to the broadband transmission for the mixed gas-cloud layer as a function of number concentration.

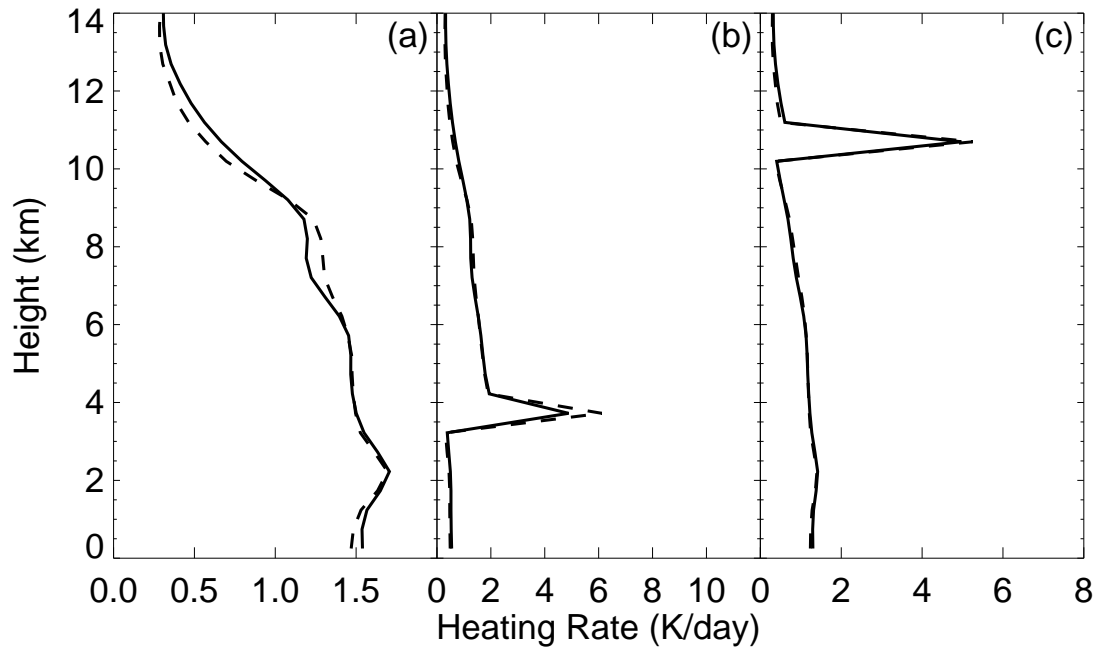


**Figure 3.5.** Broadband heating rates (K/day) for the FSCK 15-point hardwired solution (solid) and FSCK calculations using precombined gases with nongray cloud absorption combined on-the-fly serially (dashed) for the (a) CLEAR, (b) CLOUD A, and (c) CLOUD B cases of Barker et al. (2003).

and research radiative transfer methods in the next chapter.

## Chapter 4

# Evaluation versus Operational and Research Models

Based on the results from Chapter 3 we chose to implement an operational FSCK approach that uses a table of quadrature values for a precombined gas mixture together with on-the-fly serial addition of nongray cloud absorption. To assess the performance of the two-band FSCK model relative to other currently available operational models, we now compare it to other operational GCM or NWP model shortwave radiative transfer parameterizations.

A number of shortwave radiative transfer model comparisons have been undertaken in recent years, most notably the Inter-comparison of Radiation Codes in Climate Models (ICRCCM) program of the World Climate Research Programme (1984). An important follow-up study was performed by Barker et al. (2003),

hereafter referred to as “the ICRCCM-III study.” The ICRCCM-III study included results from 25 1-D models and compared the results of those models to calculations of four 3-D Monte Carlo algorithms. Since the 3-D models were not yet able to perform LBL calculations, the four 3-D models were also compared to results calculated by the CHARTS model (Clough et al. 1989), a 1-D LBL benchmark. A comparison of our results with those of the ICRCCM-III study will allow us to characterize the performance of the two-band FSCK algorithm relative to many other operational and research shortwave radiative transfer models that are currently available. This comparison will be discussed in more detail in Section 4.1.

Although many of the models included in the ICRCCM-III study are two-stream solvers similar to the one used in our model development process (Zdunkowski et al. 1982), differences between our calculated results and the ICRCCM-III results may still be attributed to differences in specific model solvers rather than the treatments of gas and cloud optical properties, which is the focus of this work. To eliminate differences resulting from the radiative transfer solver, we also compare results of the two-band FSCK approach to results from six popular operational and research GCM and NWP model radiative transfer algorithms that we have embedded, when possible, within the Zdunkowski et al. (1982) two-stream solver. These comparisons allow us to isolate those differences that result from different treatments of gas and cloud optical properties, as well as the databases upon

which they are built. We describe the six models in Section 4.2, with results of our comparisons to those models following in Section 4.3.

## 4.1 Comparison to ICRCM-III Models

In our comparisons of the performance of the two-band FSCK model to the ICRCM-III operational and research models, we adhere as closely as is possible to the atmospheric inputs for each case study. However, there are technical features of our two-band FSCK approach that are not amenable to adaptation to some of the ICRCM-III analyses. Therefore, there are differences in implementation that will produce differences in model results. We identify differences in specific results with specific implementation differences whenever possible.

The ICRCM-III study compared several aspects of shortwave radiative transfer parameterizations, including treatments of cloud overlap and the performance of different 1-D solvers relative to the 3-D solvers. While these are important considerations in the development of a complete radiative transfer model, in this work we wish to focus on the treatment of gas and cloud optical properties. Therefore, we perform calculations for the CLEAR case and when clouds are present, we assume cloud layers are simply plane-parallel and homogeneous, i.e., uniform overcast. These cases constitute a subset of the ICRCM-III study, allowing a direct comparison to the ICRCM-III results without the need for introducing any additional complications.

Each of the ICRCCM-III cases uses the lowest 62 layers of the McClatchey et al. (1972) tropical atmosphere, which extends from the surface to  $\sim 70$  km. A Lambertian surface with gray albedo of 0.20 was used. The pressure, temperature, water vapor and ozone mixing ratios are specified in the atmospheric profile, with Barker et al. (2003) also specifying a fixed carbon dioxide mixing ratio of 360 ppmv. Barker et al. (2003) also suggested that oxygen be included in the ICRCCM-III calculations, but they did not provide a specific oxygen mixing ratio. We include in our model, and in the LBL benchmark, oxygen mixing ratios adapted from a METEO 597A class project at the Pennsylvania State University (Fig. 2.6). Because methane, carbon monoxide, and nitrous oxide are built into the gas mixtures that we used to construct the precombined gas  $k$ -table for our operational FSCK approach, we include these gases as minor constituents. The inclusion of these gases may cause some difference between our calculations and those of the ICRCCM-III study.

As in Chapter 3, we apply the operational FSCK approach to the ICRCCM-III CLEAR, CLOUD A, and CLOUD B cases. Cloud properties are calculated for lognormally distributed liquid-water spheres with an effective radius  $r_{\text{eff}}$  of  $10 \mu\text{m}$  and a logarithmic distribution width of 0.38. In the CLOUD A case, the overcast cloud fills the layer between 3.5 km and 4.0 km with a liquid cloud water mixing ratio of  $q_c = 0.159 \text{ g kg}^{-1}$ , resulting in a visible optical depth of  $\sim 10$  in the cloud layer. In the CLOUD B case, the overcast cloud fills the layer between 10.5 km

and 11.0 km with  $q_c = 0.034 \text{ g kg}^{-1}$ , resulting in an in-cloud visible optical depth of  $\sim 1$ .

In the comparison below, we replicate Figures 4, 5, and 6 of the ICRCM-III study (Barker et al. 2003) using model outputs both from the Barker et al. (2003) study and from our operational two-band FSCK model with its supporting LBL calculations. These figures display results of the 1-D models as a function of spectral band, as Barker et al. (2003) have divided the spectrum into two bands, one from 0.2–0.7  $\mu\text{m}$  and the other from 0.7–5.0  $\mu\text{m}$ . As described in Chapter 2, our spectral band limits are 0.24–0.68  $\mu\text{m}$  and the other from 0.68–4.60  $\mu\text{m}$ . The full spectrum results are also shown, where the limits of the ICRCM-III models are 0.2–5.0  $\mu\text{m}$  and the limits of our model are 0.24–4.60  $\mu\text{m}$ . The difference between the spectral limits is one source of differences in the spectral band results.

The original ICRCM-III figures also show results for one of the 3-D Monte Carlo codes and CHARTS LBL benchmark calculations. Since, for this study, we are not interested in differences resulting from different solvers, we do not include the Monte Carlo and CHARTS results in our figures. For the benchmark calculations we use instead our own LBL calculations with the Zdunkowski et al. (1982) two-stream solver. Finally, while we have included results of the 1-D models as a function of cosine of solar zenith angle,  $\mu_0$ , we generated the results for the FSCK model only for  $\mu_0 = 0.5$ .

Figure 4.1a–c shows top-of-atmosphere (TOA) albedo, surface absorptance, and

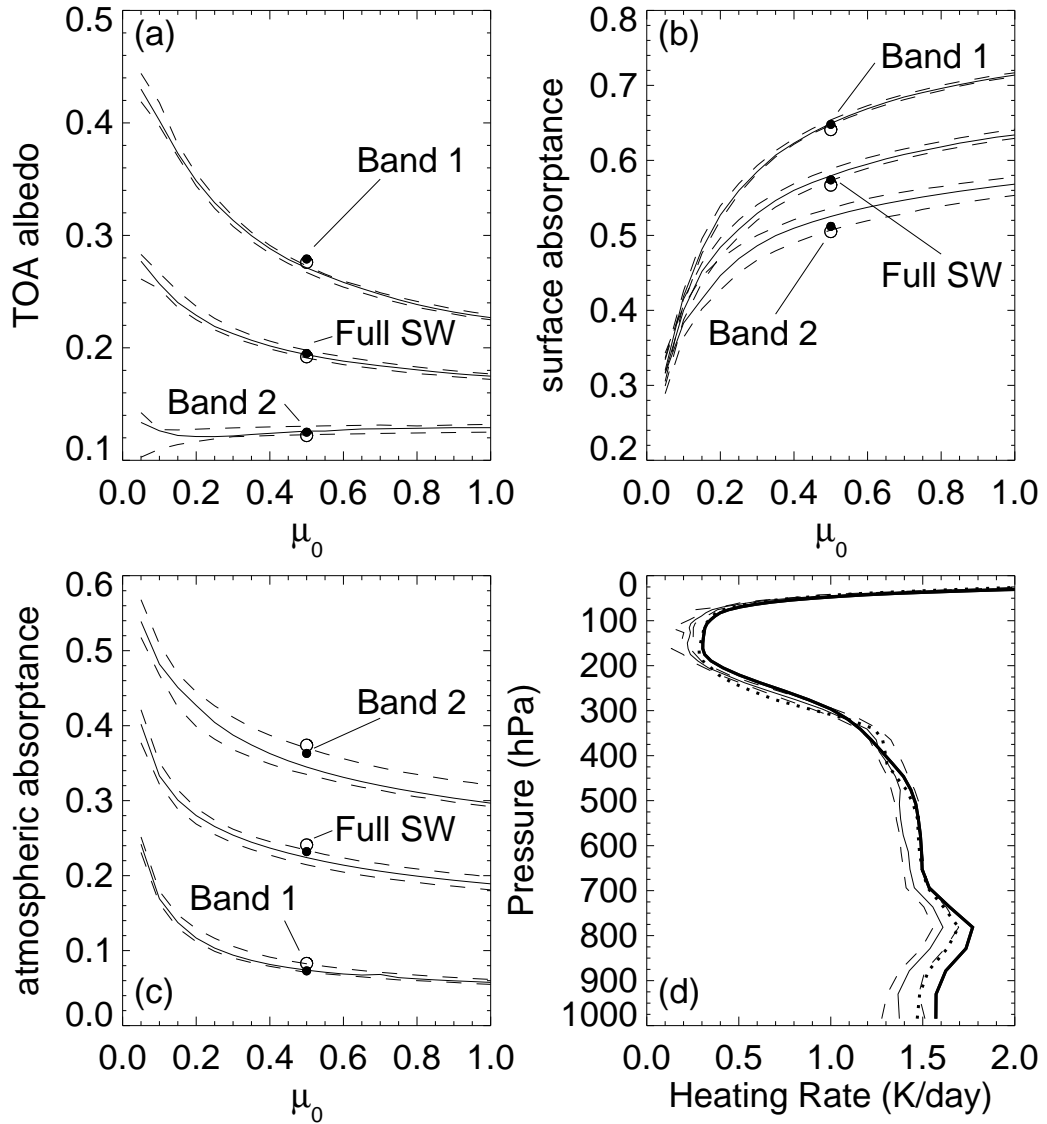


**Figure 4.1.** (a) Top-of-atmosphere albedo, (b) surface absorptance, and (c) atmospheric absorptance for the CLEAR case as a function of cosine of solar zenith angle  $\mu_0$ . ICRCCM-III 1-D model median values are represented by solid lines, while the upper and lower quartiles are represented by dashed lines. Our LBL calculations are plotted as open circles and FSCK calculations are plotted as solid circles for  $\mu_0=0.5$ . (d) Heating rate profiles for the CLEAR case. Here, the thick solid line represents our LBL benchmark calculations, whereas the thin solid and dashed lines are the same as for (a)–(c). The FSCK calculations are plotted as a dotted line.

atmospheric absorptance for the CLEAR case as a function of  $\mu_0$ . In the figures the median values of the 1-D ICRCM-III models along with the 25% and 75% percentiles are illustrated, as well as the FSCK calculations for  $\mu_0 = 0.5$ . The FSCK broadband TOA albedo agrees to within 0.001 of the median 1-D value, but the FSCK atmospheric absorptance is high and the surface absorptance is low relative to the median values of the ICRCM-III 1-D models; this difference is also apparent in the near IR band 2 results. FSCK calculations for both the broadband and band 2 surface and atmospheric absorptances are closer to the LBL calculations than are the 1-D median values. Barker et al. (2003) noted that the 1-D codes in the ICRCM-III study markedly underestimated atmospheric absorptance and overestimated surface absorptance relative to the Monte Carlo and LBL benchmarks, and postulated that the underestimations were likely due to lack of water vapor continuum absorption and parameterizations based on old spectroscopic databases relative to the newer parameterizations used by the 3-D and benchmark codes. Since the FSCK model includes water vapor continuum absorption and is based on the same fairly recent spectroscopic data as our LBL benchmark, i.e., the HITRAN-96-JPL database (Rothman et al. 1998), we expect the FSCK model to have somewhat higher atmospheric absorptance than the median of the ICRCM-III 1-D models.

The heating rates for the CLEAR case are shown in Fig. 4.1d. Although we do not use the same LBL benchmark as employed in the ICRCM-III case, our

benchmark calculations demonstrate the same feature remarked upon by Barker et al. (2003). Below  $\sim 350$  hPa “the benchmark values are systematically larger than the vast majority of 1D estimates.” Barker et al. (2003) again attributed those differences to poor, or old, water vapor line and continuum absorption information used by the 1-D models. In the case of the FSCK model, in which we use the same water vapor line and continuum absorption as our LBL benchmark, our heating rates are generally closer to the benchmark calculations than the other 1-D models. The mean bias heating rate error relative to the LBL benchmark over all atmospheric layers is  $-0.27$  K/day for the median of the 1-D models, but is only  $+0.04$  K/day for the FSCK model. Another likely source for the improvement of FSCK over the ICRCM-III 1-D models is the fact that the FSCK approach explicitly accounts for the spectral variation of the solar irradiance. Where the FSCK heating rates differ from the LBL calculations, errors are primarily due to interpolations from tabulated absorption coefficients as discussed in Chapter 3, rather than a deficiency in the FSCK algorithm itself. Recall that the FSCK algorithm produced more accurate results relative to LBL calculations when the exact atmospheric profile was prespecified as in Chapter 2.

Figures 4.2 and 4.3 show results for the CLOUD A and CLOUD B cases, respectively. Note that we have reduced the vertical extent of the y-axes in Figs. 4.2d and 4.3d in order to show heating rates within and immediately above and below the cloud layers. As in Fig. 4.1, Figs. 4.2a–c and 4.3a–c show median and

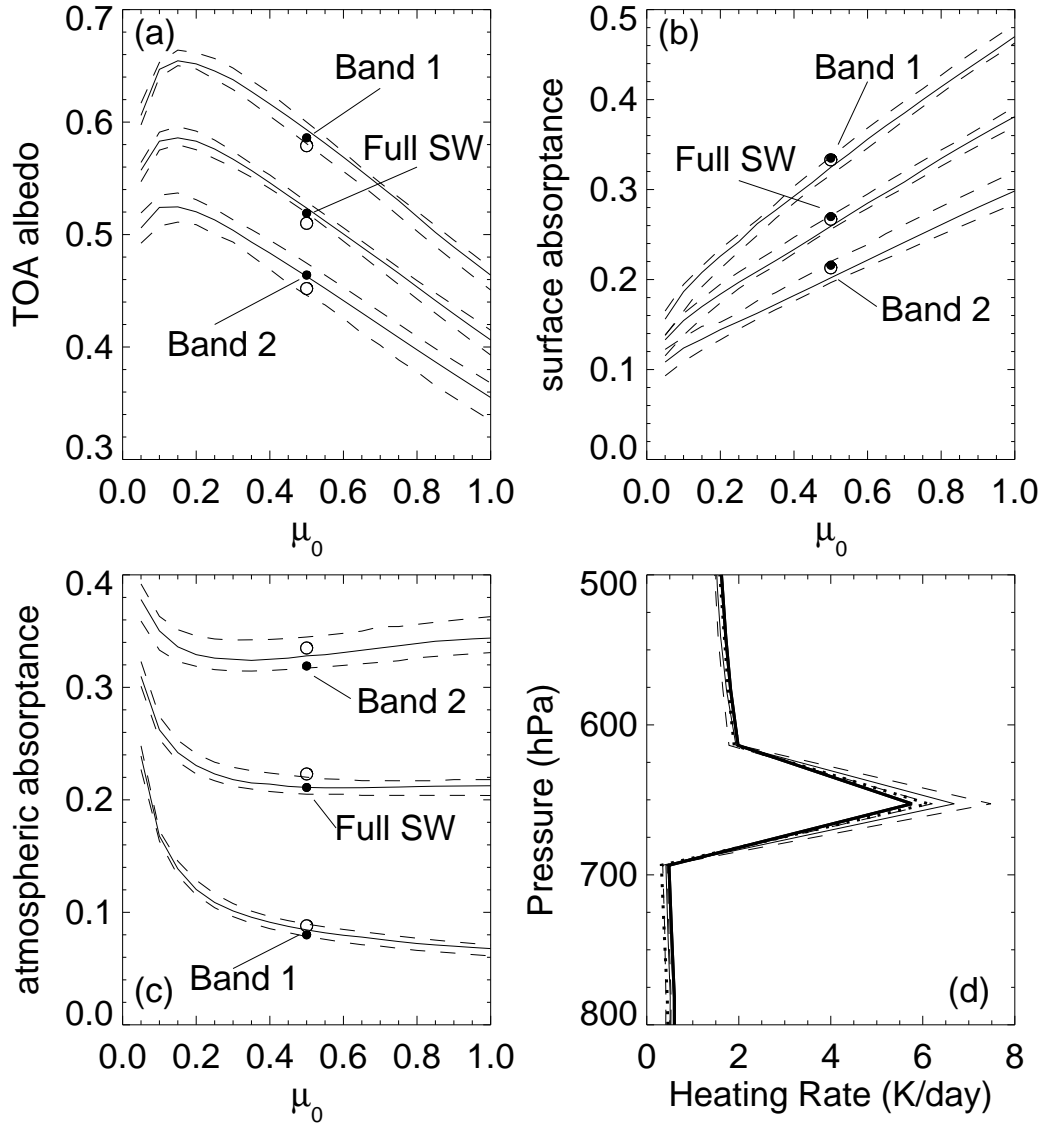


**Figure 4.2.** (a) Top-of-atmosphere albedo, (b) surface absorptance, and (c) atmospheric absorptance for the CLOUD A case as a function of cosine of solar zenith angle  $\mu_0$ . ICRCM-III 1-D median values are represented by solid lines, while the upper and lower quartiles are represented by dashed lines. Our LBL calculations are plotted as open circles and FSCK calculations are plotted as solid circles for  $\mu_0=0.5$ . (d) Heating rate profiles for the CLOUD A case. Here, the thick solid line represents our LBL benchmark calculations, whereas the thin solid and dashed lines are the same as for (a)–(c). The FSCK calculations are plotted as a dotted line.

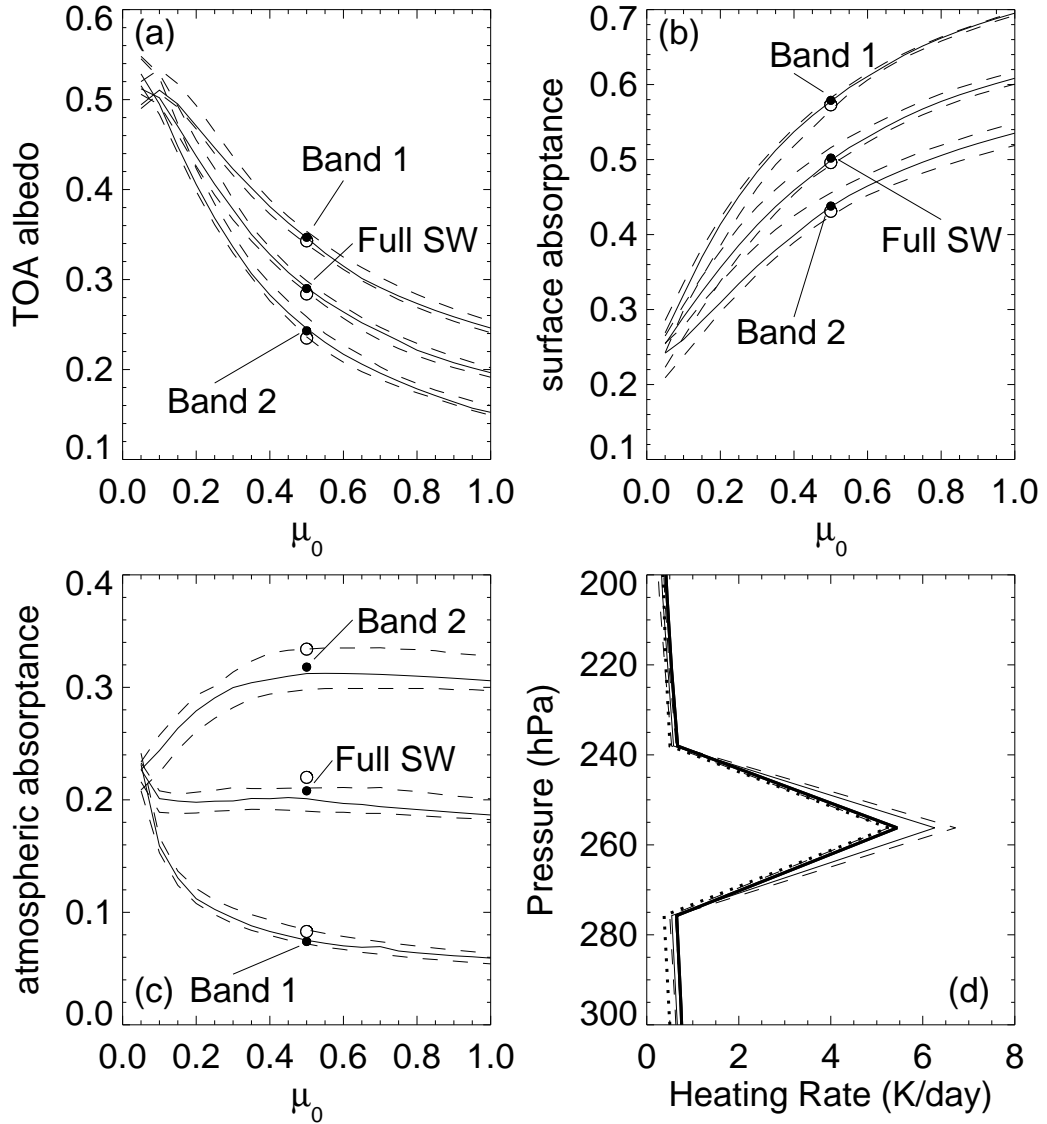


**Figure 4.3.** (a) Top-of-atmosphere albedo, (b) surface absorptance, and (c) atmospheric absorptance for the CLOUD B case as a function of cosine of solar zenith angle  $\mu_0$ . ICRCM-III 1-D median values are represented by solid lines, while the upper and lower quartiles are represented by dashed lines. Our LBL calculations are plotted as open circles and FSCK calculations are plotted as solid circles for  $\mu_0=0.5$ . (d) Heating rate profiles for the CLOUD B case. Here, the thick solid line represents our LBL benchmark calculations, whereas the thin solid and dashed lines are the same as for (a)–(c). The FSCK calculations are plotted as a dotted line.

quartile values for the ICRCM-III 1-D models rather than mean values. This explains the apparent contradiction of FSCK atmospheric absorptance values in Fig. 4.2c that are low relative to the 1-D model median values for both band 1 and band 2, but are virtually identical to the full shortwave 1-D median value.

In both cloud cases the heating rate profiles demonstrate that the FSCK treatment of cloud absorption as nongray is more accurate relative to LBL calculations than the ICRCM-III 1-D models, which tend to overabsorb in the cloud layers. In-cloud heating rate errors for the CLOUD A case were 6.1% for the FSCK approach and 16.0% for the 1-D model median. For the CLOUD B case in-cloud heating rate errors were -3.5% for the FSCK approach and 15.0% for the 1-D model median. The most likely source of error for the ICRCM-III 1-D models is averaging cloud properties over spectral intervals where the properties are changing rapidly. To demonstrate that the overestimate of heating by the ICRCM-III 1-D models relative to our LBL calculations is not the result of the ICRCM-III models extending their calculations in the near infrared to  $5.0 \mu\text{m}$  versus the FSCK upper limit of  $4.6 \mu\text{m}$ , we performed LBL calculations from a wavelength of  $4.6\text{--}5.0 \mu\text{m}$  and added the absorbed energy to our LBL results. The clear sky heating rates increased by 0.01 K/day or less, while the in-cloud heating rates increased by approximately 0.09 K/day, or 1.6% for CLOUD A and by 0.13 K/day or 2.5% for CLOUD B.

Given the higher in-cloud heating rates of the ICRCM-III models relative to

FSCK and LBL calculations, one might expect ICRCM-III 1-D model column atmospheric absorptance to exceed that of the FSCK calculations. This is the case for bands 1 and 2 of CLOUD A and band 1 of CLOUD B. However, FSCK atmospheric absorptance for CLOUD B exceeds that of the ICRCM-III 1-D models for band 2 and for the full shortwave. We attribute this result to poor water vapor line and continuum absorption in the ICRCM-III 1-D models, just as we did for the source of differences in the CLEAR case comparisons. In both of the cloud cases for all of the spectral bands the median 1-D atmospheric absorptance is less than the LBL benchmark. As pointed out by Barker et al. (2003), the ICRCM-III 1-D models “underestimate systematically relative to...CHARTS by amounts similar to those for” the CLEAR case.

As one would expect, with less cloud absorption the FSCK results for the CLOUD A and CLOUD B cases show more energy absorbed at the surface relative to the ICRCM-III 1-D models. Lower FSCK TOA albedo values relative to the ICRCM-III results, especially for the CLOUD A case, have a number of possible sources. Primary among them is less than optimal tuning of the gray cloud asymmetry parameter (Section 2.2.3). This might also contribute to FSCK atmospheric absorptance values that underestimate those calculated by LBL for the CLOUD A and B cases.

## 4.2 State-of-the-Art Operational and Research Models

While the comparisons with the ICRCM-III cases demonstrate that the FSCK approach produces reasonable results relative to other methods, we cannot easily use the ICRCM-III study to separate differences between the solvers, the treatments of gas and cloud optical properties, and any manipulations of the input fields. To eliminate the solver and manipulations of the input fields as the sources of any differences, we picked six NWP and research-grade schemes commonly used for handling gas and cloud absorption and scattering and we embedded them within the Zdunkowski et al. (1982) two-stream solver. We can draw much stronger conclusions regarding treatment of gas absorption using the results from these six models, as well as our FSCK and LBL results, all of which use the same solver.

The six shortwave radiative transfer algorithms that we chose for this study are the Dudhia shortwave scheme (Dudhia 1989), the Geophysical Fluid Dynamics Lab (GFDL)-Eta scheme (Lacis and Hansen 1974), the Community Atmosphere Model version 2 (CAM2) and version 3 (CAM3) schemes (Briegleb 1992) counted as one model, the correlated  $k$ -distribution model developed by Fu and Liou (1992), the correlated  $k$ -distribution model developed by Kato et al. (1999), and the shortwave correlated  $k$ -distribution model Rapid Radiative Transfer Model (RRTM SW; Mlawer and Clough 1997; Mlawer and Clough 1998). A breakdown for these

models of the treatment of gas and cloud optical properties by spectral interval is depicted in Fig. 4.4. In the figure, spectral intervals not treated by a model are indicated by a diagonal line through the interval. The first three models rely heavily on the empirical methods of Lacis and Hansen (1974), while the other models, separated from the first three by a blank line in Fig. 4.4, are three different implementations of the correlated  $k$ -distribution approach.

The codes for the models used in this comparison were obtained from a variety of sources, including from modules within operational NWP models. Because our focus here is on optical property generation, we extracted only those parts of the codes necessary for our comparison. In the case of the GFDL-Eta scheme, the code for cloudy conditions was heavily interwoven through a number of subroutines with dependencies upon other modules. We felt that the time spent extracting the cloud optical property code for the GFDL-Eta scheme was better spent elsewhere. As a consequence, no results are included for the GFDL-Eta scheme for the CLOUD A and CLOUD B cases.

The work by Lacis and Hansen (1974) is a fundamental source for three of the models used in this comparison, although each of the three models uses different aspects of the work. Because of the relevance of their work to current operational models, we will take a close look at the development of their treatments of gas absorption and how those treatments are applied in the three models. We will also show how a number of the six models in our study, including that of Lacis and



Hansen (1974), discuss or implement ideas that are similar to the FSCK method for the specific case of solar radiation and point out where those models differ from the FSCK approach.

#### 4.2.1 Dudhia Shortwave Scheme

The Dudhia shortwave scheme (Dudhia 1989), which is used in the fifth generation Penn State University/National Center for Atmospheric Research (NCAR) Mesoscale Model (MM5) (Grell et al. 1994) and the Weather Research and Forecasting (WRF) model (Michalakes et al. 2001), is based on the absorption by water vapor in the near infrared according to Lacis and Hansen (1974). The treatment of water vapor absorption by Lacis and Hansen (1974) is, in turn, based on work by Howard et al. (1956) and Yamamoto (1962). Yamamoto (1962) defined absorptivity as the ratio of the energy absorbed by the entire vertical air column to the solar constant, assuming normal incidence. Applying that definition, Yamamoto (1962) took the measured absorption data of Howard et al. (1956), as well as data for two additional weak absorption bands not included in the earlier measurements, and weighted them by measured incoming solar energy in the same spectral intervals to get fractional absorptivities. Yamamoto (1962) then summed the fractional absorptivities to get a total absorptivity for the near infrared (0.7–4.0  $\mu\text{m}$ ) and plotted a curve of total absorptivity as a function of precipitable water vapor. Lacis and Hansen (1974) then fit a curve using a least squares fit method

to the curve of Yamamoto (1962), arriving at a function for absorption due to water vapor given by

$$A_{wv}(y) = \frac{2.9y}{(1 + 141.5y)^{0.635} + 5.925y}, \quad (4.1)$$

where  $A_{wv}(y)$  is the fraction of incident solar flux that is absorbed by water vapor, i.e., the absorptivity, as a function of the water vapor amount,  $y$  (in units of centimeters of precipitable water vapor).

Molecular and aerosol scattering in the Dudhia model are treated as gray and proportional to the atmospheric mass path length, which accounts for the solar zenith angle, with a constant giving 10% reflectivity for 1 atm. Absorptivity and reflectivity due to clouds are provided by tabulated functions of the cosine of the zenith angle,  $\mu_0$ , and  $\ln(w/\mu_0)$ , where  $w$  [ $gm^{-2}$ ] is the vertically integrated cloud water path. These tabulated functions are derived from theoretical results of Stephens (1978). The gas and cloud optical properties used in the Dudhia model are not easily put into a form, i.e., gas absorption optical depth, gas scattering optical depth, cloud extinction optical depth, cloud asymmetry parameter, and cloud single-scattering albedo, needed by the Zdunkowski et al. (1982) two-stream solver. Consequently, we calculated heating rates using the native solver of the Dudhia scheme for the comparisons in Section 4.3.

The Dudhia solver simply attenuates the downward flux layer by layer. First, the top layer is treated as though it is the entire atmospheric column, and the ab-

sorption for that column is calculated. Next, the atmospheric thickness is extended to include the top two layers, and the absorption for that thickness is calculated, and so on. The heating rates for a layer are determined by subtracting absorption by water vapor and cloud for the previously calculated thickness from that of the current thickness. The simplicity of this model gives it a significant advantage over other models included in this comparison with respect to efficiency, but this efficiency comes at the expense of accuracy, as will be shown in Section 4.3.

#### **4.2.2 GFDL-Eta Scheme**

The GFDL-Eta scheme used in the National Centers for Environmental Prediction (NCEP) Eta model and the WRF model is also based on the work of Lacis and Hansen (1974), adopting from that work the parameterization of absorption by ozone and by water vapor in cloudy skies. This model uses two spectral bands. One band, covering ultraviolet ( $\lambda \leq 0.35 \mu\text{m}$ ) and visible wavelengths ( $0.5 \leq 0.7 \mu\text{m}$ ), accounts for absorption by ozone and water vapor, as well as molecular “Rayleigh” scattering. A second band, for near infrared wavelengths, accounts for absorption by water vapor and carbon dioxide.

Using a least square fit to solar flux-weighted measured ozone absorptivities, Lacis and Hansen (1974) express the fraction of solar flux across the ultraviolet

wavelengths absorbed by the Hartley and Huggins ozone bands as

$$A_{oz}^{uv}(x) = \frac{1.082x}{(1 + 138.6x)^{0.805}} + \frac{0.0658x}{(1 + 103.6x)^3}, \quad (4.2)$$

where  $x$  is ozone amount (in units of cm at 293.16 K and 1013.25 hPa). The fraction of solar flux across visible wavelengths absorbed by the Chappuis ozone band is given by

$$A_{oz}^{vis}(x) = \frac{0.02118x}{(1 + 0.042x + 0.000323x^2)}. \quad (4.3)$$

Total ozone absorption then is given by

$$A_{oz}(x) = A_{oz}^{uv}(x) + A_{oz}^{vis}(x). \quad (4.4)$$

Absorption by carbon dioxide in the near infrared is parameterized according to Sasamori et al. (1972), who use the relation

$$\alpha = 2.35 \times 10^{-3}(u + 0.0129)^{0.26} - 7.5 \times 10^{-4}, \quad (4.5)$$

where  $\alpha$  is the fractional absorptivity and  $u$  is the pressure-corrected path length of carbon dioxide (in units of cm reduced to STP). This relation is an empirical curve fit to the data of Burch et al. (1960).

The GFDL-Eta model uses, for clear and cloudy conditions, an approach for absorption by water vapor in the near infrared that is adapted from the cloudy-sky

formulation by Lacis and Hansen (1974), who use a “ $k$ -distribution” consisting of 8 points derived from measured absorptivities. Lacis and Hansen (1974) did not have a “database of monochromatic absorption coefficients and their pressure-temperature dependence.” So, rather than construct a true  $k$ -distribution, they used a least-square search to numerically invert the equation

$$A_{wv}(y) = 1 - \int_0^\infty p(k)e^{-ky} dk \approx 1 - \sum_{n=1}^N p(k_n)e^{-k_n y} \Delta k_n, \quad (4.6)$$

to obtain  $N$  values for the discrete probability distribution  $p(k_n)$  and the corresponding absorption coefficient  $k_n$ . The absorption for water vapor is corrected for pressure and temperature by using an effective absorber amount given by

$$y_{\text{eff}} = y \left( \frac{p}{p_0} \right)^n \left( \frac{T_0}{T} \right)^{\frac{1}{2}}. \quad (4.7)$$

This approach is effectively the weighted-sum-of-gray-gases method (Hottel and Sarofim 1967; Modest 1991). Lacis and Hansen (1974) state that “the expression  $p(k)dk$  is the fraction of the incident flux that is associated with an absorption coefficient between  $k$  and  $k + dk$ ,” in essence describing the FSCK method for the special case of shortwave radiation. Had a “database of monochromatic absorption coefficients and their pressure-temperature dependence” been available to them, Lacis and Hansen (1974) might have developed the FSCK method of Modest (2003).

The weights,  $p(k_n)$ , used in the GFDL-Eta model have been altered from those given by Lacis and Hansen (1974). Moreover, three additional  $k$ -values have been added to improve the accuracy of absorption by water vapor (Y.-T. Hou 2004, personal communication). Rayleigh scattering is accounted for as Lacis and Hansen (1974) describe for clear-sky conditions and is only calculated for the ultraviolet-visible band and only for the lower atmosphere. The reflection function for the lower atmosphere for the UV-VIS band is given by

$$\bar{R}(\mu_0) = \frac{0.219}{1 + 0.816\mu_0}, \quad (4.8)$$

where  $\mu_0$  is the cosine of the solar zenith angle. This formula is again obtained by an iterative least-square fit to obtain the best agreement between the vertical absorption profiles for their parametric formula and their benchmark.

As with the Duhdia scheme, the gas absorption and scattering properties are firmly integrated with the solver, an adding and doubling scheme also described by Lacis and Hansen (1974). So rather than attempt to disentangle the properties from the solver and implement them into the Zdunkowski et al. (1982) two-stream solver, we use heating rates calculated by this model's solver for our comparisons in Section 4.3.

### 4.2.3 CAM2 and CAM3 Schemes

The Community Atmosphere Model version 2 (CAM2; Collins 1998), which is the NCAR community climate model, includes a radiative transfer parameterization that is an updated version of the parameterization used in the Community Climate Model version 2 (CCM2; Briegleb 1992). The Briegleb (1992) solver in CCM2 is also available as a shortwave radiative transfer option in MM5. The CAM2 model accounts for absorption by ozone, water vapor, carbon dioxide, and oxygen, scattering by molecules, and absorption and scattering by cloud-water drops.

Ozone absorption was initially treated by Briegleb (1992) as gray in eight spectral intervals from 0.2–0.7  $\mu\text{m}$ . The absorption coefficient values and solar weights were derived from the absorption cross section data of King and Gast (1961), and solar data used for the weights were taken from Labs and Neckel (1968). Briegleb (1992) used a trial and error method to reduce the number of spectral intervals from those of King and Gast (1961) to the eight intervals between 0.2–0.7  $\mu\text{m}$ . Later, the spectral interval from 0.35–0.70  $\mu\text{m}$  was divided at 0.64  $\mu\text{m}$  to provide better agreement with observations (Collins 1998), for a total of nine ozone-related bands.

Absorption by oxygen accounts for the A- and B-oxygen bands between 0.35–0.70  $\mu\text{m}$ . Oxygen absorption is treated as gray over the interval and the absorption

is scaled by the absorber amount  $u_{O_2}$  defined as

$$u_{O_2} = \sqrt{\mu_0 q_{O_2} \frac{p}{g}}, \quad (4.9)$$

where  $p$  is the path pressure,  $g$  is gravity,  $\mu_0$  is the cosine of the solar zenith angle, and  $q_{O_2}$  is the mass mixing ratio of oxygen.

Absorption by carbon dioxide in two near infrared bands, 2.63–2.86  $\mu\text{m}$  and 4.16–4.55  $\mu\text{m}$ , is treated in much the same way as oxygen using data from Kiehl et al. (1985). Note that the 4.16–4.55  $\mu\text{m}$  band is actually subdivided into two monochromatic bands using the weighted-sum-of-gray-gases method (Hottel and Sarofim 1967; Modest 1991).

As in the GFDL-Eta model, the Briegleb (1992) approach makes use of the Lacis and Hansen (1974) treatment of water vapor absorption in the near infrared. Briegleb (1992) uses seven of the eight  $k$ -values from Lacis and Hansen (1974), but the weights are empirically adjusted to give good agreement to LBL calculations by Ramaswamy and Freidenreich (1991) of water vapor transmission (B. P. Briegleb and W. D. Collins 2004, personal communication). Cloud optical properties are taken from Slingo (1989), where the properties are parameterized based on liquid water path and equivalent radius of the drop-size distribution.

Molecular scattering optical depths are taken from Fröhlich and Shaw (1980), and are applied at the midpoint of each interval from 0.20–0.35  $\mu\text{m}$ . For the visible band the optical depth was evaluated at 0.495  $\mu\text{m}$ , the wavelength that gave the

best agreement with their benchmark. The molecular scattering optical depth for the first quadrature interval in the near infrared was tuned to fit their benchmark calculations, while the midpoint of the near infrared spectral interval was used to calculate the molecular scattering optical depths for the remaining quadrature intervals.

The CAM version 3 (CAM3) radiation code (Collins et al. 2004) is an update of version 2 with a modified treatment of absorption by water vapor in the near infrared. In CAM3 the quadrature weights are the same as those used by CAM2. The seven  $k$ -values are determined using iterative exponential sum fitting to fit LBL calculations. For the first three  $k$ -values, Collins et al. (2004) minimize differences between flux divergences calculated with their parameterized  $k$ -values and weights and those calculated by LBL. For the remaining four  $k$ -values, Collins et al. (2004) minimize differences between parameterized and LBL-calculated heating rate profiles.

The LBL calculations are based on the HITRAN2000 database and its 2001 update (Rothman et al. 2003) with water vapor continuum absorption modeled using the CKD-2.4.1 approximation (Clough et al. 1989). Solar spectral information is taken from Kurucz (1994), and Rayleigh scattering in the near infrared is calculated following Lenoble (1993). The near infrared spectral interval in CAM3 also includes the effects of water vapor line absorption out to 10  $\mu\text{m}$ , although the overall solar weight given to the band is unchanged from the CAM2 weight for

the band from 0.7–5.0  $\mu\text{m}$ . In application, the only differences between the CAM2 and CAM3 shortwave radiation codes are the values of the seven  $k$ -values in the near infrared and the value of an empirical constant,  $\delta$ , used to scale water vapor absorption to agree with LBL heating rates in the stratosphere.

We calculate the gas and cloud optical properties according to the methods used in the CAM2 and CAM3 models and pass them to the Zdunkowski et al. (1982) two-stream solver to calculate heating rates for the comparisons in Section 4.3.

#### 4.2.4 Fu and Liou Scheme

Fu and Liou (1992) describe a correlated  $k$ -distribution model that divides the solar spectrum into five bands associated with water vapor, with a sixth band for ozone absorption added later. The Fu and Liou (1992) scheme uses a total of 44 (later 54) quadrature points. The Fu and Liou (1992) model bears a similarity to the FSCK model for shortwave radiation described in Section 2.1.2 because they account for the spectral dependence of the solar flux by defining the cumulative  $k$ -distribution as

$$g(k, p, T) = \sum_j S_j g_j(k, p, T) \Delta\nu_j / S_{\bar{\nu}}, \quad (4.10)$$

where  $S_{\bar{\nu}} = \sum_j S_j \Delta\nu_j$ . Fu and Liou (1992) denote each of the six spectral bands as  $\Delta\nu$ , which are themselves divided into spectral subintervals of width  $\Delta\nu_j$  taken to be  $50 \text{ cm}^{-1}$ . Over each of the  $\Delta\nu_j$  subintervals the solar flux is assumed to

be constant with a spectrally integrated value of  $S_j$ . A cumulative  $k$ -distribution,  $g_j(k, p, T)$ , is created for each of the subintervals from which the total cumulative  $k$ -distribution,  $g(k, p, T)$ , for the band is constructed. Cumulative  $k$ -distributions are created for 11 pressures,  $p$ , and 3 temperatures,  $T$ .

The version of the Fu and Liou (1992) model used for the comparison in Section 4.3 is essentially that described in the original paper, together with the added spectral band for ozone absorption. We obtained the code from the Spherical Harmonic Discrete Ordinate Method (SHDOM; Evans 1998) website. As a consequence, our version of the Fu and Liou (1992) code is not the more recent version used by the Clouds and the Earth’s Radiant Energy System (CERES) program at NASA Langley. Deficiencies in our version of the Fu and Liou (1992) parameterization include use of a single ozone band for the ultraviolet and visible spectral regions, the outdated water vapor continuum absorption (Roberts et al. 1976), and missing trace gas absorbing species (Evans 2004, personal communication). We couple the gas absorption  $k$ -values of Fu and Liou (1992) with Rayleigh scattering calculated according to Teillet (1990) and cloud optical properties calculated according to the “Mie” approach of Toon and Ackerman (1981) into the two-stream solver of Zdunkowski et al. (1982) for the comparisons in Section 4.3.

### 4.2.5 Kato Scheme

The correlated  $k$ -distribution model developed by Kato et al. (1999) is a traditional correlated  $k$ -distribution method as described in Section 2.1.1. The model accounts for gas absorption by ozone, oxygen, carbon dioxide, and water vapor, including water vapor continuum absorption, using 154 quadrature points across 32 spectral intervals over each of which cloud properties are approximately constant. Tables of quadrature values, similar to those described in Chapter 3, are generated for water vapor and oxygen, while ozone is treated as a gray gas over several of the spectral intervals and carbon dioxide and ozone are treated as minor constituents with fixed concentrations in the  $k$ -distributions. Using these gas absorption properties, along with Rayleigh scattering calculated according to Teillet (1990) and cloud optical properties calculated according to Toon and Ackerman (1981), we again calculate heating rates with the two-stream solver of Zdunkowski et al. (1982) for the comparisons in Section 4.3.

### 4.2.6 RRTM SW Scheme

The shortwave Rapid Radiative Transfer Model (RRTM SW; Mlawer and Clough 1997; Mlawer and Clough 1998) is a correlated  $k$ -distribution model that uses 14 narrow bands for the shortwave, with 16 quadrature points per band, for a total of 224 radiative transfer calculations. Gas absorption values for water vapor, carbon dioxide, ozone, methane, and oxygen are stored at 59 reference pressures. The

spectral bands “were chosen as a consequence of the absorption band structure of the absorbing species (Mlawer and Clough 1997).”

Applying an algorithm similar to the FSCK approach, RRTM keeps track of the “mapping” of absorption coefficients from spectral space to  $g$ -space for the highest atmospheric level in the McClatchey et al. (1972) midlatitude summer atmosphere as a reference level. That mapping is then applied to the Planck, or solar source, function (e.g., Kurucz 1994) and these mapped solar irradiance values are summed and used as weights for each  $g$ -value.

At the reference level, this method would be identical to that described in Section 2.1.2 if the mapped solar source function were used instead of the standard  $k$ -distribution. In order to ensure equivalence with the FSCK method, it would be necessary to keep track of the monochromatic spectral intervals associated with each mapped value of the solar source function. This would make it possible to normalize the resulting energy distribution over the spectral interval to which it applies. As such, this method would be exact for a homogeneous atmosphere if extended to the full spectrum. However, because the mapping of the solar irradiances is only done at the reference level, if this technique were extended to the full spectrum, the mapping would not be correct at levels where the sorting changes significantly, i.e., where correlation breaks down. Because Mlawer and Clough (1997) have implemented bands that take into account correlations across the shortwave spectrum, they avoid a breakdown of the mapping but at a cost of

many radiative transfer calculations.

The RRTM SW treatment of absorption by gases used for this comparison is the version implemented in SHDOM (Evans 1998) and differs from the original algorithm of Mlawer and Clough (1997) and Mlawer and Clough (1998). In the SHDOM version, although the  $k$ -distribution mapping of the solar source function is implemented, the mapped solar irradiances are summed for each complete spectral band rather than just for the weights associated with each quadrature point. As a result, some of the correlation between solar flux and absorption is lost (S. A. McFarlane 2004, personal communication). Mlawer and Clough (1998) show that neglecting the mapping results in a substantial difference in energy absorbed by the atmosphere. While the mapping is not completely neglected for the solar irradiances in this implementation, these differences in implementation and their consequences must be noted when interpreting results in the comparisons in Section 4.3.

As for Fu and Liou (1992) and Kato et al. (1999), we used the gas absorption properties from the RRTM SW algorithm, along with cloud optical properties calculated according to Toon and Ackerman (1981), to compute heating rates with the two-stream solver of Zdunkowski et al. (1982). Furthermore, nongray Rayleigh scattering is normally combined with the absorption coefficients in the RRTM scheme (S. A. McFarlane 2004, personal communication). The precise methodology for combining Rayleigh scattering with gas absorption coefficients

and later separating the two quantities for use by the solver is not clear from the presentation of the method (Mlawer and Clough 1997; Mlawer and Clough 1998). Consequently, Rayleigh scattering for the RRTM scheme is gray in each spectral band for our comparison, calculated according to Teillet (1990). Mlawer and Clough (1998) remark that the use of spectrally averaged values of key physical properties, such as the Rayleigh scattering used for this comparison, will result in significant differences from the complete RRTM SW scheme.

### **4.3 Comparison to State-of-the-Art Operational and Research Models**

Figure 4.5 shows heating rates for the ICRCCM-III CLEAR case calculated by each of the models described in Section 4.2, where height is the vertical coordinate in the figure rather than pressure as in the ICRCCM-III comparison. Figure 4.5a extends into the mesosphere, a part of the atmosphere not normally considered in numerical weather prediction. However, ozone must be included as an absorbing gas in the shortwave, and a model must account for the reduction of incoming solar radiation by ozone in the stratosphere before the radiation reaches a typical “model top” level used for other physical and dynamical calculations. Otherwise, too much absorption and heating will occur in the top layers of the model. Figure 4.5a shows a striking range of heating rate differences between models, primarily

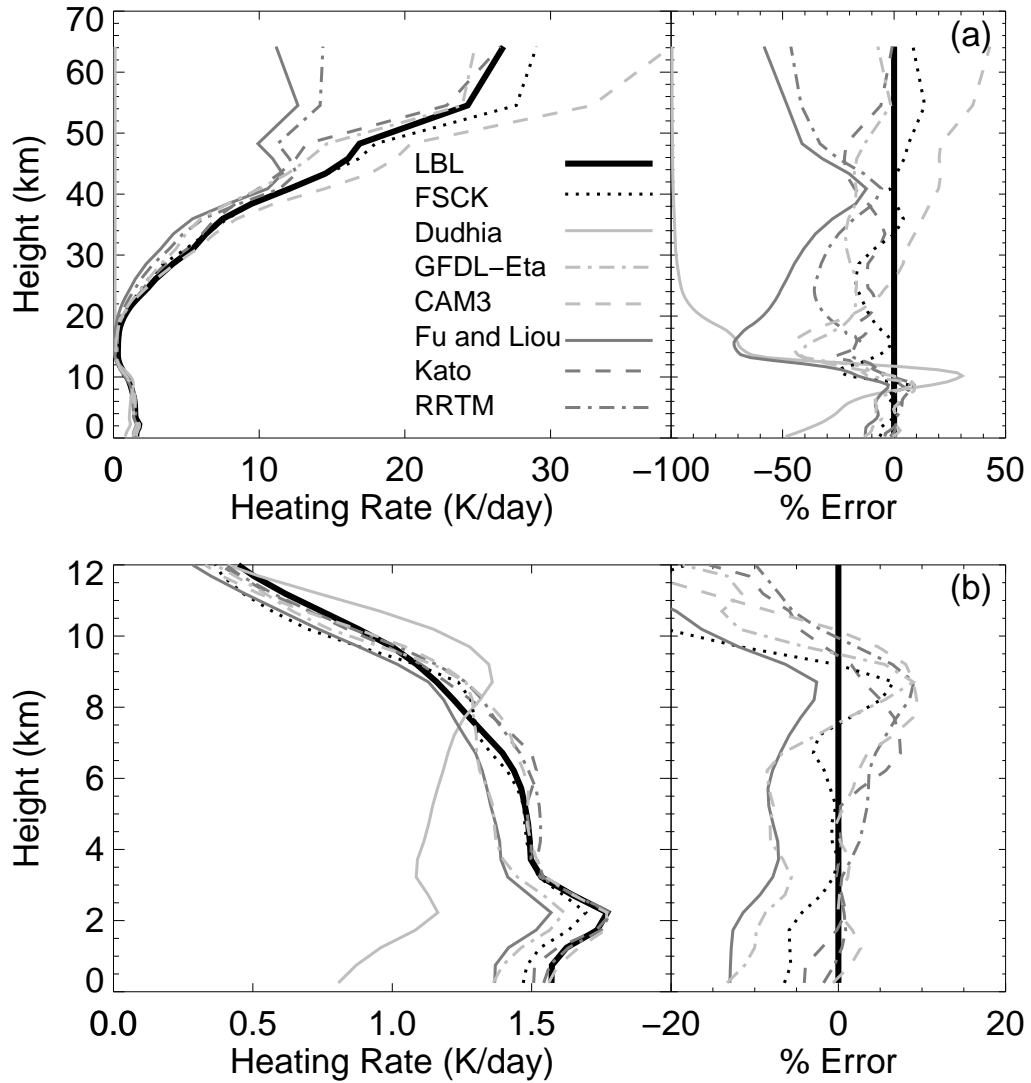


**Figure 4.5.** Broadband heating rates (K/day) calculated by LBL (black solid), the FSCK approach (black dotted), the Dudhia scheme (light gray solid), the GFDL-Eta scheme (light gray dash-dot), the CAM3 scheme (light gray dashed), the Fu and Liou scheme (dark gray solid), the Kato scheme (dark gray dashed), and the RRTM SW scheme (dark gray dash-dot) for the CLEAR case of Barker et al. (2003).

due to differences in the treatment of absorption by ozone. Also note that the heating rate percent errors for all of the models in the comparison become large and negative between  $\sim 12$ – $18$  km as the magnitude of the LBL heating rate profile becomes small, i.e., less than  $0.5$  K/day.

The Dudhia model, which does not include absorption by ozone, was not designed to model the atmosphere above the troposphere. Therefore, this model has essentially 100% heating rate errors relative to LBL calculations above the lower stratosphere (Fig. 4.5a). Near the troposphere (Fig. 4.5b) the Dudhia model overestimates heating by over 30% and underestimates heating by approximately 50% near the ground. The heating rate RMS error for the Dudhia model relative to the LBL benchmark over all atmospheric layers is 6.28 K/day. Note that although the heating rate profiles are shown for the Dudhia model in the left panels of Fig. 4.5a–b and Dudhia model heating rate errors are plotted in the right panel of Fig. 4.5a, the Dudhia model heating rate errors are not plotted in the right panel of Fig. 4.5b.

Figure 4.6 shows the percent errors in downward flux absorbed at the surface calculated by each of the models relative to the LBL calculated value of  $483.72 \text{ Wm}^{-2}$  for the ICRCCM-III CLEAR case. In numerical weather prediction, downward flux at the surface is extremely important because it is a major contribution to the surface energy budget. The surface energy budget controls, to a great extent, the operation of the planetary boundary layer model, which, in turn, has a major influence on the overall model physical and dynamical solution.

The Dudhia model underestimates the downward flux at the surface by nearly 6%. While the Dudhia model errors in heating rate and downward flux at the surface are quite large relative to the other models in this comparison, the heating

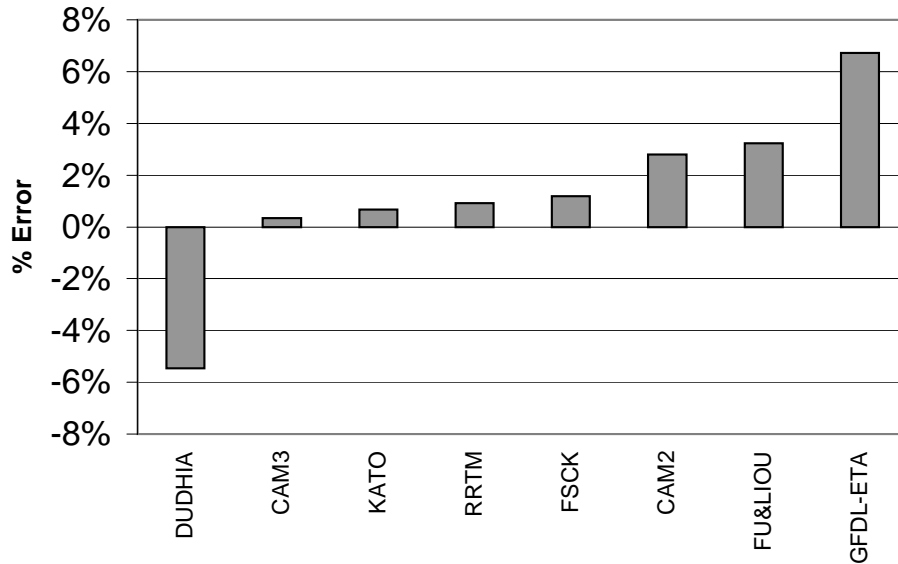


**Figure 4.6.** Percent error in model downward flux absorbed at the surface relative to LBL calculations ( $483.72 \text{ Wm}^{-2}$ ).

rates in the troposphere are correct to within a factor of 2 or less, which may be acceptable for some applications where efficiency has a significantly higher priority than accuracy. Figure 4.7 shows that the Dudhia model requires  $\sim 8$  seconds on a single 1.7 GHz processor for 100,000 solutions of the ICRCCM-III CLEAR case, which includes generating the optical properties and running the radiative transfer solver. This is more than four times faster than the next fastest model.

The GFDL-Eta model performs exceptionally well in the upper atmosphere compared to the other models, with heating rate errors generally less than 20% above  $\sim 45$  km (Fig. 4.5a). In the lower atmosphere the GFDL-Eta heating rates are less accurate than most of the other models, underestimating heating by as much as 10–15% (Fig. 4.5b). The heating rate RMS error for the GFDL-Eta model relative to the LBL benchmark over all atmospheric layers is 0.78 K/day.

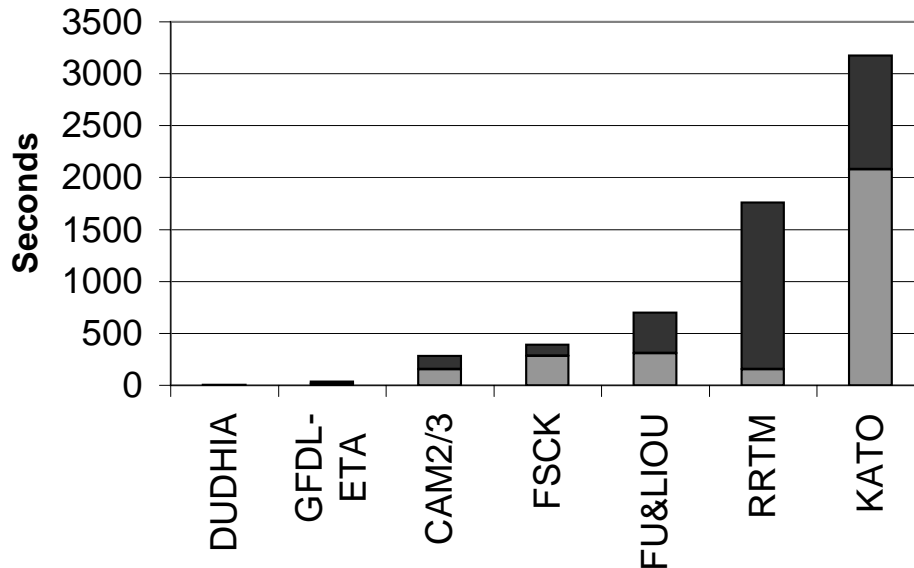


**Figure 4.7.** Processing time in seconds on a single 1.7 GHz processor for 100,000 iterative model calculations without inputs and outputs to hard disk. The time spent on creating the optical properties is represented by the lightly shaded region, while the time spent on the solver is the darkly shaded region.

This deficiency is also evident in Fig. 4.6, which shows that the GFDL-Eta model overestimated the downward flux at the surface by 6.7% . Figure 4.7 shows that the GFDL-Eta model was the second fastest in this comparison, requiring about 34 seconds for 100,000 solutions of the CLEAR case.

The CAM3 model is significantly more accurate in the troposphere than the CAM2 model (not shown) for this CLEAR case due to the use of recent water vapor line and continuum absorption data. There is no difference in the treatment of ozone between the CAM2 and CAM3, however, with upper atmospheric heating rate errors as large as 40% (Fig. 4.5a). CAM3 heating rate errors in the lower troposphere are small compared to most other models in the comparison, generally less than 5% below 6 km (Fig. 4.5b). The heating rate RMS error for the CAM3

model relative to the LBL benchmark over all atmospheric layers is 2.00 K/day. While the improvement of CAM3 over CAM2 in the troposphere is in large part due to the use of more recent information, the small heating rate errors relative to the LBL calculations in the comparison are an indication of the care taken in the empirical reevaluation of water vapor absorption for CAM3. The CAM3 model improvement over CAM2 is evident in Fig. 4.6, which shows that the CAM2 model overestimated the CLEAR case downward flux at the surface by 2.8% while the CAM3 model overestimates it by only 0.3%. Timing for the CAM2 and CAM3 models is identical, since only eight parameters changed between the two versions. The two models each take 285 seconds for 100,000 solutions of the CLEAR case (Fig. 4.7), with 55% of that time devoted to generating the optical properties and the remaining 45% of the time required for the radiative transfer solver.

The version of the Fu and Liou (1992) model that we have tested here has heating rate errors of nearly 60% in the upper atmosphere (Fig. 4.5a) and nearly 13% in the lower troposphere (Fig. 4.5b). The heating rate RMS error for the Fu and Liou model relative to the LBL benchmark over all atmospheric layers is 2.83 K/day. Because we are not using the most current version of the Fu and Liou (1992) model, these heating rate errors result, in part, from the omission of water vapor continuum absorption and old spectral line absorption information for both water vapor and ozone absorption. But, we cannot separate this source of error from the choice of bands and the number of quadrature points per band.

The Fu and Liou (1992) model also overestimates downward flux at the surface by 3.2%, or  $15.6 \text{ Wm}^{-2}$  (Fig. 4.6) and requires 702 seconds per 100,000 solutions of the CLEAR case (Fig. 4.7). Of the total processing time, 44% was expended to calculate the optical properties and 56% was used by the solver. The generation of optical properties requires 5.7 seconds per quadrature point per 100,000 solutions, resulting mainly from the 2-D interpolation of  $k$ -values stored on the pressure and temperature grid.

The Kato et al. (1999) model tested here is based on the same HITRAN database as the LBL benchmark. This fact, coupled with the large number of spectral bands in the Kato scheme, leads to heating rate errors that are less than 10% at the top of the atmosphere (Fig. 4.5a) and remain less than 30% through the entire atmospheric profile. Errors from the surface to  $\sim 6$  km are less than 5% and remain less than 10% up to 10 km (Fig. 4.5b). The heating rate RMS error for the Kato model relative to the LBL benchmark over all atmospheric layers is 0.85 K/day. Downward flux at the surface is overestimated by  $3.2 \text{ Wm}^{-2}$  or 0.7% (Fig. 4.6). This accuracy results from the use of 154 quadrature points covering 32 bands, which comes at the cost of efficiency. The Kato model required 3175 seconds for 100,000 solutions (Fig. 4.7), of which 65% was used to generate the optical properties and 35% was needed to run the solver. The generation of optical properties requires 13.5 seconds per quadrature point per 100,000 solutions, resulting mainly from the 3-D interpolation from  $k$ -values stored on a pressure,

temperature, and water vapor mixing ratio grid.

The RRTM shortwave model heating rate errors are nearly 50% in the upper atmosphere (Fig. 4.5a), and the heating rate profile above  $\sim 40$  km bears a strong similarity to that of the Fu and Liou (1992) model. In the lower atmosphere, however, heating rate errors are near 0% below 4 km, and do not exceed 10% in the lowest 12 km (Fig. 4.5b). The heating rate RMS error for the RRTM model relative to the LBL benchmark over all atmospheric layers is 2.28 K/day. The RRTM shortwave model overestimates downward flux at the surface by 0.9% (Fig. 4.6) and requires 1758 seconds for 100,000 solutions (Fig. 4.7). Of the total time used by RRTM, only 9% was used to generate the optical properties, while the remaining 81% was used by the solver.

The time used by the Zdunkowski et al. (1982) two-stream solver is directly proportional to the number of quadrature points per layer. The large proportion of time used by the solver with the RRTM shortwave model-generated optical properties results from the use of 224 quadrature points. The amount of time required to generate the optical properties for a correlated  $k$ -distribution model appears to be related not only to the number of points, but also the dimensionality of the table in which  $k$ -values are stored. In RRTM the  $k$ -values are stored on a 1-D pressure grid and generation of the optical properties requires only 0.7 seconds per quadrature point per 100,000 solutions. To all appearances the code to generate optical properties for the RRTM shortwave model has been carefully optimized.

Note that we did not use any compiler optimization options for any of the models used in this comparison.

Heating rates calculated by the two-band FSCK model remain within 20% of the LBL benchmark through the entire atmospheric profile (Fig. 4.5a), with the exception from 12–18 km where LBL heating rate values are less than 0.5 K/day. Heating rate errors below 10 km do not exceed 7% (Fig. 4.5b). The heating rate RMS error for the FSCK model relative to the LBL benchmark over all atmospheric layers is 0.57 K/day. The FSCK model-calculated downward surface fluxes are overestimated by  $5.7 \text{ Wm}^{-2}$  or 1.2% (Fig. 4.6). The FSCK model took 391 seconds for 100,000 solutions (Fig. 4.7), requiring 72% of the time for calculating optical properties, averaging 18.9 seconds per quadrature point per 100,000 solutions, and 18% for the solver.

The results of the model comparisons for the ICRCCM-III CLOUD A and CLOUD B cases are shown in Fig. 4.8. As in Fig. 4.5b, we show heating rate profiles for the Dudhia model, but we omit the Dudhia model heating rate errors. As mentioned above, heating rates for the GFDL-Eta model are not shown for the CLOUD A and CLOUD B cases.

The Dudhia model overestimates in-cloud heating by nearly 4 K/day for the CLOUD A case and by over 8 K/day for the CLOUD B case, representing errors of about 66% and 130%, respectively. Again, these results are due to the use of a very simple empirical algorithm that is fast but not accurate. There is much

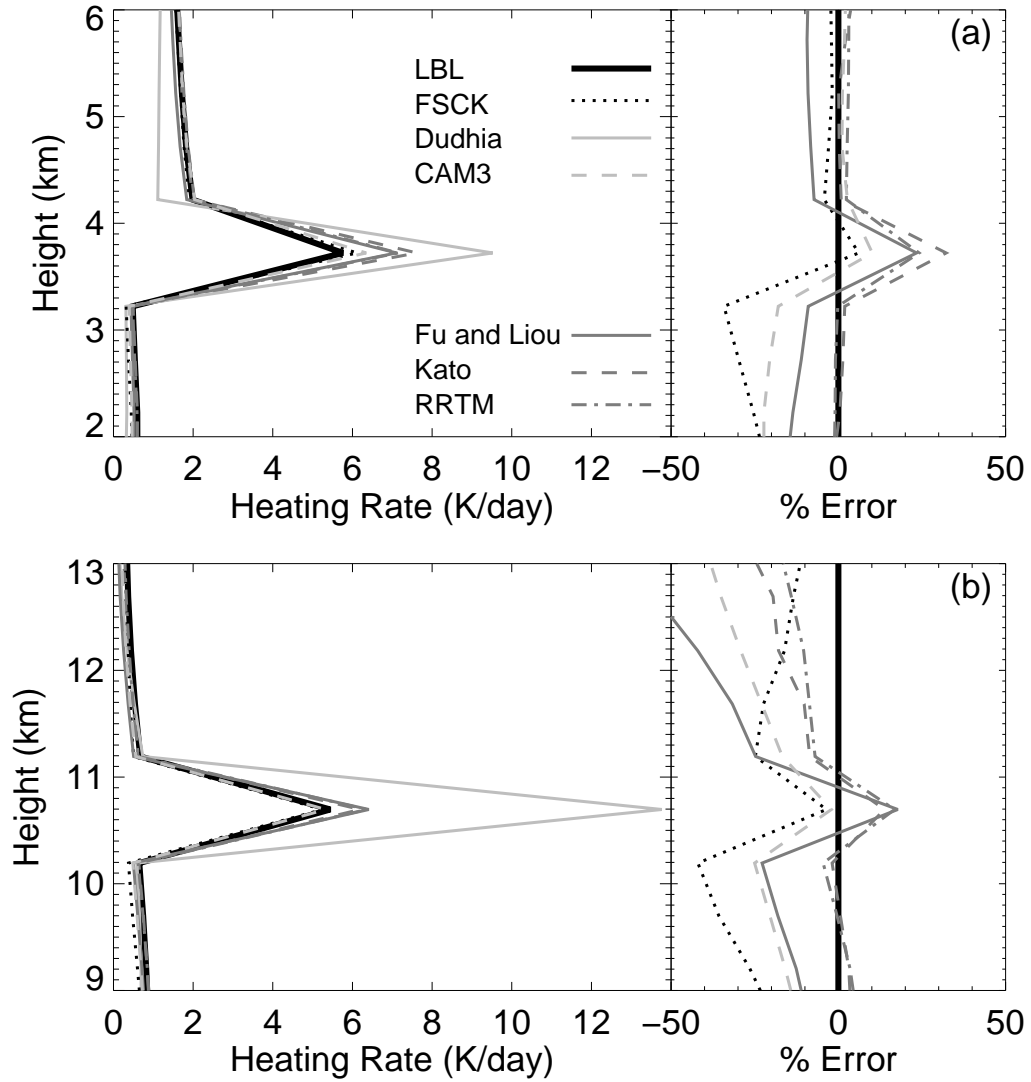


**Figure 4.8.** Broadband heating rates (K/day) calculated by LBL (black solid), the FSCK approach (black dotted), the Dudhia scheme (light gray solid), the CAM3 scheme (light gray dashed), the Fu and Liou scheme (dark gray solid), the Kato scheme (dark gray dashed), and the RRTM SW scheme (dark gray dash-dot) for (a) the CLOUD A case and (b) the CLOUD B case of Barker et al. (2003).

less variability of in-cloud heating rate errors among the other models in this comparison. The CAM3 model, which uses the Slingo (1989) parameterization, has in-cloud heating rate errors of about 10% for the CLOUD A case (Fig. 4.8a) and less than 1% errors for the CLOUD B case (Fig. 4.8b). The CAM3 in-cloud heating rates are the same as for CAM2 (not shown).

We use 500 hPa transmission-weighted band average “Mie” theory cloud optical properties calculated according to Toon and Ackerman (1981) for all three correlated  $k$ -distribution models, i.e., the Fu and Liou (1992) model, the Kato et al. (1999) model, and the RRTM shortwave model of Mlawer and Clough (1997) and Mlawer and Clough (1998). For the averaging of the cloud optical properties we used the spectral bands appropriate for each model. We also used the Toon and Ackerman (1981) method to calculate cloud optical properties for the LBL benchmark and the nongray cloud absorption for the FSCK model, although at a spectral resolution of  $0.01 \mu\text{m}$ . For the LBL benchmark and the FSCK model, we then interpolated the  $0.01 \mu\text{m}$  resolution cloud absorption coefficients to the higher resolution gas absorption coefficients before using them. We performed a similar interpolation of the cloud scattering coefficients in the LBL benchmark calculations. As explained in Chapter 2 the two-band FSCK cloud scattering properties were tuned to minimize flux errors.

As Fig. 4.8 illustrates, the nongray treatment of cloud absorption in the FSCK model is an accurate alternative to treating cloud optical properties as gray in

several narrow spectral bands. The process of averaging cloud absorption over typical narrow bands, where the absorption is rapidly changing, clearly may introduce more error than using directly nearly monochromatic LBL and FSCK cloud absorption coefficients in the calculations.

Figures 4.5, 4.6, 4.7, and 4.8 clearly show that the two-band FSCK model is more accurate than most of the empirically based models. Moreover, the two-band FSCK approach is more efficient than all of the correlated  $k$ -distribution models used in this comparison while rivaling them in accuracy. The new CAM3 model is also relatively accurate and efficient, at least in the lower troposphere for the test cases in our current set of comparisons.

As we showed in Chapter 2, the FSCK method itself is not the source of the errors that we see in Fig. 4.5. In fact, none of the models included in our comparison rival the accuracy of the 15-quadrature point “hardwired” solution through most of the atmosphere, as shown in Fig. 4.9. The heating rate RMS error for the 15-quadrature point “hardwired” model relative to the LBL benchmark over all atmospheric layers is 0.30 K/day. The 8192-point “hardwired” solution, an even closer representation of the performance of the FSCK algorithm itself, has heating rate errors that do not exceed 5% below 9 km or above 17 km. The heating rate RMS error for the 8192-quadrature point “hardwired” model relative to the LBL benchmark over all atmospheric layers is 0.16 K/day.

The errors in our implementation of the two-band FSCK approach are intro-

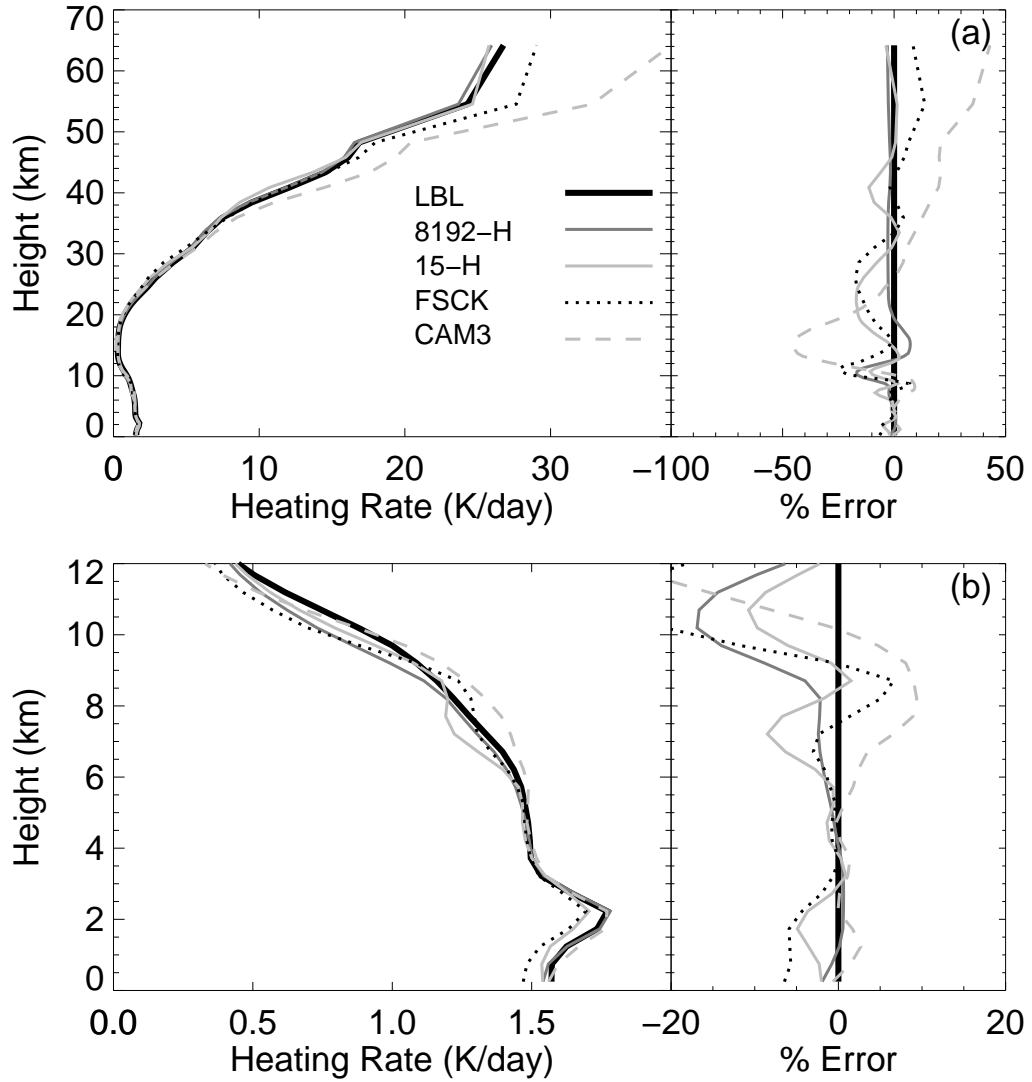


**Figure 4.9.** Broadband heating rates (K/day) for LBL calculations (black solid), the FSK 8192-point hardwired solution (dark gray solid), the FSK 15-point hardwired solution (light gray solid), the FSK solution from the current implementation (black dotted), and the CAM3 scheme solution (light gray dashed) for the CLEAR case of Barker et al. (2003).

duced in several of the steps in our model development process. First, relatively small errors are introduced by our choice of 15 quadrature points. These errors are indicated by the deviation of the 15-quadrature point “hardwired” solution from the 8192-quadrature point solution as shown in Fig. 4.9. Additional errors are introduced by our choice of pressures, temperatures, and mixing ratios used to calculate stored absorption coefficients and the method we have chosen to interpolate from the stored values to the atmospheric profile of interest. These errors are evident when comparing the FSCK tabulated solution to the 15-quadrature point “hardwired” solution in Fig. 4.9.

However, even with these errors, the two-band FSCK approach is more consistently accurate through the depth of the profile than the CAM3 model. As Fig. 4.9 illustrates, the CAM3 model overestimates heating by as much as 42% relative to LBL from approximately 25–65 km versus a maximum FSCK error of 17%. CAM3 calculations then underestimate heating by as much as 45% from about 10–25 km, versus -25% for the FSCK approach. Except for a narrow range where the CAM3 results change from overheating to underheating, CAM3 again overestimates heating relative to LBL calculations by more than the FSCK calculations from about 5–10 km. From approximately 3–5 km the FSCK and CAM3 methods produce similar heating rate errors relative to LBL. Only from the lowest model layer to about 3 km are the CAM3 heating rates more accurate than the FSCK calculations relative to LBL calculations. The reduced accuracy of the FSCK ap-

proach for the lowest 3 km likely results from poor resolution in pressure space of the tabulated  $k$ -values. For the lowest atmospheric layers,  $k$ -values are linearly interpolated between those calculated for 1050 hPa and 834 hPa.

In terms of both accuracy and efficiency the current implementation of the two-band FSCK approach is a viable alternative to any of the state-of-the-art models included in our comparison. However, given the superior accuracy of the two-band FSCK approach demonstrated by the 8192-quadrature point and 15-quadrature point “hardwired” solutions, it may be worthwhile to continue development of a more accurate, yet still efficient, method to select, store, and retrieve absorption coefficients.

# Chapter 5

## Discussion

### 5.1 Summary and Conclusions

A fundamental limitation of the correlated  $k$ -distribution method for radiative transfer is the requirement that the Planck function be constant over the spectral interval for which the  $k$ -distributions are constructed. In Chapter 2 we presented the FSCK method of Modest (2003) which removes the requirement of a constant Planck function by creating Planck function-weighted  $k$ -distributions. We simplified the FSCK equations for the special boundary-value problem of solar radiation and implemented them using the solar source function of Kurucz (1994), rather than the Planck function, to weight the  $k$ -distributions.

In Section 2.2, we presented a series of initial tests of the FSCK algorithm. For the first case, which included only the effects of gaseous absorption with zero

surface albedo, we used the FSCK algorithm to model the full shortwave spectrum (0.24–4.60  $\mu\text{m}$ ) as a single spectral interval. Using 8192 quadrature points to obtain a baseline estimate of the accuracy of the FSCK method, the heating rate RMS error for the full atmospheric depth was approximately 4.2%, but was nearly 20% for the lowest 14 km. This significant tropospheric heating rate error motivated us to divide the solar spectrum into two bands in order to circumvent a breakdown of correlation with height in clear-sky absorption. This application of the FSCK method to multiple spectral intervals is similar to the part-spectrum approach of Modest and Riazzi (2004), where absorption coefficients are divided into spectral regions based on similar scattering properties. After dividing the spectrum into two bands, using 8192 quadrature points for each band, the heating rate RMS error was reduced to 3.0% for the full atmospheric depth and 3.8% for the lowest 14 km.

We then reduced the number of FSCK quadrature points to 5 points in band 1 (0.24–0.68  $\mu\text{m}$ ) and 10 points in band 2 (0.68–4.60  $\mu\text{m}$ ), and again computed the fluxes and heating rates for comparison with the 8192 quadrature-point and LBL results. The RMS error for clear-sky broadband heating rates computed using 15 quadrature points was 7.3% for the full atmospheric depth and 5.1% for the lowest 14 km. The 15 quadrature-point solution appeared to us as the best compromise between accuracy and computational efficiency that we could obtain. We computed fluxes and heating rates for cases with nonzero surface

albedo, molecular (“Rayleigh”) scattering and low- and high-altitude clouds in three different atmospheres.

Numerical tests demonstrated that both gray and nongray treatments of absorption by cloud particles produced reasonable in-cloud heating rates relative to LBL calculations. When clouds were treated as nongray, in-cloud heating rate errors were approximately 8–12%, for both single cloud-layer and combined low- and high-cloud cases. Gray cloud absorption produced less consistent results than nongray cloud absorption, with in-cloud heating rate errors of less than 2% for both single cloud-layer cases, but 6–14% for the combined low- and high-cloud cases. For both treatments of cloud absorption, scattering by cloud particles was treated as gray in the two-spectral bands, where we tuned the gray scattering parameters. That is, we first estimated the scattering parameters using “Mie” theory, then we adjusted them to minimize flux errors above and below the cloud layer. Once completed for a given cloud-drop distribution effective radius and spectral band, the gray scattering parameters are tabulated and become part of the parameterization.

The remaining errors in the two-band FSCK 8192 and 15 quadrature-point results, when using the nongray treatment of absorption by cloud particles, may be the result of a breakdown of correlation with height, as we observed in the full-spectrum clear-sky case. Although the heating rate errors with the nongray treatment are typical of, or smaller than, the magnitude of in-cloud heating rate errors of other 1-D models, we could subdivide the spectrum into more bands to

address the possible breakdown of correlation. Such a modification might improve the accuracy of in-cloud heating rates, but would require additional quadrature points and increasing computational costs.

In Chapter 3 we advanced the FSCK method from a model that can be applied to an atmosphere with pre-specified pressures, temperatures, mixing ratios, and cloud properties, as in Chapter 2, to an operational model that calculates fluxes and heating rates given any input atmospheric conditions. We developed a set of pressures, temperatures, and mixing ratios that we used to calculate tabulated absorption coefficients for both the major and minor gas constituents. We tested several different methods for combining constituent absorption coefficients, either during the model development process or on-the-fly during model runtime.

Of the methods for combining gas absorption coefficients that we tested, the method of precombining monochromatic absorption coefficients in spectral space produced the smallest RMS errors in the heating rate profiles. This is not surprising since the precombined gas method does not assume that component species are statistically uncorrelated. Furthermore, in order to combine gases on-the-fly, the absorption coefficients for each constituent are stored in tables of quadrature values. The  $k$ -values are retrieved from the tables and interpolated to the atmospheric state of interest before being combined, and the process of combining on-the-fly requires additional interpolations. Each of these processes, i.e., quadrature prior to combining constituents and interpolations before and during the combination

procedure, introduces errors not present in the precombined absorption coefficient method.

The serial method of combining gas absorption coefficients on-the-fly is promising, especially regarding its flexibility for easily combining an arbitrary number of gas constituents. Since absorption coefficients are tabulated for each individual gas, whenever the individual gas absorption coefficients are not affected by self-broadening, as in the case of ozone and carbon dioxide, they only need to be calculated as a function of pressure and temperature, not mixing ratio. The absorption coefficients of these gases can then simply be scaled by absorber amount. By reducing the number of dimensions in the table of stored  $k$ -values, the number of interpolations required to retrieve them is reduced. However, in order for the method to be effective operationally, the number of interpolations must be reduced further and the accuracy of those interpolations improved. One possible way of improving the quality of interpolations from  $k_{\text{mix}}(g_{\text{mix}})$  to  $k(g)$  at our chosen quadrature values would be to use cubic spline interpolations, although such an approach would reduce efficiency.

We reexamined the treatment of absorption by cloud particles as either gray or nongray in the context of the two-band FSCK approach. We were not able to find a single two-band set of gray parameters, i.e., extinction cross section, single-scattering albedo, and asymmetry parameter, that could accurately reproduce both the CLOUD A and CLOUD B LBL results. We were able to tune the

gray parameters to model accurately either of the clouds, but parameters tuned for one cloud were inappropriate for the other. This result implies that any operational scheme would minimally have gray cloud parameters that are a function of both cloud-particle size and their vertical location within the atmosphere. Such a scheme is not practical to implement. As a consequence of these results, we did not develop further the use of gray cloud optical properties for the two-band application of the FSCK method.

We determined that precombining nongray cloud absorption coefficients with gas absorption coefficients was not operationally feasible because of the large number of  $k$ -values that must be stored in such an approach. However, combining nongray cloud absorption on-the-fly with precombined gas absorption proved to be accurate and efficient, and this was the approach that we implemented for the comparisons performed in Chapter 4.

Comparing the current implementation of the two-band FSCK approach to the 15 quadrature-point “hardwired” solution, we find that the accuracy of atmospheric  $k$ -values interpolated from tabulated  $k$ -values improves if the tabulated  $k$ -values are calculated for more pressures in the lower troposphere. For applications in NWP, one might offset the additional stored  $k$ -values in the lower troposphere by storing fewer values in the upper atmosphere. However, upper atmospheric radiative transfer may not be insignificant in NWP applications, since incident radiation must be attenuated accurately in a spectrally dependent fashion to the

“model top” in order to obtain accurate atmospheric heating rates and surface fluxes. Regardless, the accuracy of our FSCK 15 quadrature-point solution could be improved by incorporating additional pressures into the absorption coefficient tables, with the only penalty being a table that is larger.

In Chapter 4 we evaluated the performance of the two-band FSCK model relative to LBL calculations and to the performance of other operational and research radiative transfer parameterizations. The evaluation was carried out in two stages. First, we compared the FSCK calculations to the calculations of 24 one-dimensional radiative transfer models that were included in the ICRCCM-III study of Barker et al. (2003). Overall, the two-band FSCK approach had smaller errors relative to the LBL calculations that we used as a benchmark than the median of the 1-D models included in the ICRCCM-III study. In the CLEAR case the FSCK model was closer than the other 1-D models to the benchmark for TOA albedo, surface absorptance, atmospheric absorptance and the majority of the heating rate profile for both bands, i.e., the ultraviolet-visible band and the near infrared, as well as for the broadband shortwave. The median of 24 1-D models had a clear-sky mean bias error of -0.27 K/day relative to LBL benchmark heating rates, while the operational implementation of the FSCK approach had a mean bias error of +0.04 K/day. Barker et al. (2003) attributed the tendency of the 1-D models to underabsorb relative to the ICRCCM-III benchmarks to the fact that many of the 1-D models were developed with older water vapor line and continuum absorption

data. The FSCK model, however, is based on the same spectroscopic data as the LBL calculations that we used as a benchmark, thereby eliminating a source of error present in some of the ICRCM-III 1-D models. Another likely source of improved accuracy in the FSCK approach is that this approach explicitly accounts for spectral variations in solar irradiance.

For the CLOUD A and CLOUD B cases, FSCK broadband in-cloud heating rates were closer to the benchmark than the median of the 1-D models. For CLOUD A the FSCK error was 6.1% versus 16.0% for the 1-D model median, and for CLOUD B the FSCK error was -3.5% versus 15.0% for the 1-D model median. However, although the FSCK-calculated in-cloud heating rate errors were small compared to the other 1-D models, the FSCK-calculated atmospheric absorptance was too low compared to the benchmark and the TOA albedo was too high, indicating less than optimal tuning of our gray cloud scattering properties. Further refinement of the gray cloud scattering parameters will require additional testing on a variety of cloud fields to assess the performance of tabulated values under different atmospheric conditions.

Second, we compared FSCK calculations to those of seven specific state-of-the-art operational and research models. We described, in detail, the methods used by each of the seven models to generate optical properties. In the descriptions of the models we illustrated how several operational scaled  $k$ -distribution and empirical models have their basis in algorithms described by Lacis and Hansen (1974). We

embedded the gas and cloud optical properties from the FSCK model, the LBL model, and most of the six operational and research models into the two-stream solver of Zdunkowski et al. (1982), permitting us to make a direct comparison of treatments of optical properties and the heating rate profiles that result from them.

The model comparisons make clear that there is a trade-off between accuracy and efficiency. The Dudhia (1989) scheme was the fastest of the models included in our comparison, requiring only 7 seconds for 100,000 solutions of the CLEAR case. However, the Dudhia scheme produces a downward flux at the surface that underestimates the benchmark by nearly 6% and atmospheric heating rates that underestimate LBL-calculated values by 50–100% through most of the atmosphere. The clear-sky RMS heating rate errors calculated over all atmospheric layers relative to the LBL benchmark for the three empirically-based models were 0.78–6.28 K/day. The Kato et al. (1999) scheme calculates relatively accurate heating rates through the entire profile, but is computationally expensive because the scheme uses 154 quadrature points. RMS errors for the three correlated  $k$ -distribution models were 0.85–2.83 K/day. Although several models outperformed the others for particular parts of the profile, such as the CAM3 scheme (Collins et al. 2004) and the RRTM SW scheme (Mlawer and Clough 1997; Mlawer and Clough 1998) which both had heating rate errors of less than 5% below 5 km and the GFDL-Eta scheme (Lacis and Hansen 1974) which had heating

rate errors less than 20% above 45 km, none performed as consistently accurate through the depth of the atmosphere as the two-band FSCK approach, which had an RMS heating rate error of 0.57 K/day over the full atmospheric profile.

Explicitly accounting for the spectral variability of the solar source function likely improves the accuracy of the FSCK approach over other models, but the contribution of this effect is difficult to quantify, especially since a number of the models account for spectral variability to a certain extent. Heating rate errors for the FSCK approach were less than 24% for the full atmospheric depth, and less than 7% in the lowest 10 km. The superior accuracy of the FSCK approach also extended to the CLOUD A and CLOUD B cases, where the FSCK treatment of absorption by cloud particles as nongray outperformed the narrow-band gray cloud-absorption treatments of the three correlated  $k$ -distribution schemes. While FSCK-calculated in-cloud heating rate errors were 6.1% and -3.5% for the CLOUD A and CLOUD B cases, respectively, heating rate errors for the correlated  $k$ -distribution schemes ranged from 23.4–32.2 % for the CLOUD A case and 13.8–17.8% for the CLOUD B case. The FSCK approach required 391 seconds for 100,000 solutions of the CLEAR case, while the next fastest correlated  $k$ -distribution scheme took nearly twice as long.

Although the current implementation of the two-band FSCK approach performed well compared to the ICRCCM-III 1-D models and the six state-of-the-art operational and research models, there are still errors that may be eliminated by

further refining the implementation. None of the models included in the study rival the accuracy of the FSCK 8192-point “hardwired” atmosphere solution, which had an RMS heating rate error of only 0.16 K/day. The efficiency of the two-band FSCK approach, with its 15 quadrature points, rivals the efficiency of the CAM3 scheme. Consequently, we will continue to refine the implementation of the FSCK scheme for shortwave atmospheric radiative transfer while the work of coupling the current FSCK scheme with an operational NWP model or GCM proceeds.

## 5.2 Future Work

In Section 4.3 we saw that the CAM3 model had smaller heating rate errors from the surface to about 3 km relative to the LBL benchmark than the FSCK model. We attributed the reduced accuracy of the FSCK model over this range of altitudes to poor resolution in the tabulated  $k$ -values in pressure space for the lower atmosphere. Because the size of the  $k$ -value table is relatively small (approximately 1 megabyte), we can tabulate  $k$ -values for more pressures in the lower atmosphere, bearing in mind that for each pressure we add to the table we are actually adding  $k$ -values calculated for that pressure with every combination of temperature and gas mixing ratio in the table.

An alternate method for providing a table of pre-calculated  $k$ -values might be the use of a table that could adapt dynamically to meteorological conditions for a particular geographic region. With such a table, if  $k$ -values near the atmospheric

state of interest exist in the table, they are used for the solution. If no  $k$ -values exist near the desired atmospheric state, new  $k$ -values are computed on-the-fly from a secondary database of  $k$ -distributions and added to the table. The table size would be managed by removing from the table those  $k$ -values which have not been used over a specified number of model iterations.

Another aspect of the FSCK operational model that may benefit from additional research is the treatment of cloud optical properties. In Section 4.1 we noted that a likely cause of underestimated TOA albedo by the FSCK model was less than optimal tuning of the gray cloud scattering parameters. Since multiple combinations of cloud scattering cross sections and asymmetry parameters can result in the same tuned solution, we must empirically determine the single combination of these parameters that is most robust for a variety of real cloud profiles. Necessary tests of optimally tuned parameters would include variations of water content and cloud physical thickness for both liquid and ice clouds.

Inherent to all radiative transfer parameterizations in NWP models is the approximate representation of clouds, as well as clear sky, in the models by discrete vertical layers. Radiative heating rates are strongly dependent upon the vertical thickness of model layers; that is, thin layers will have significantly higher heating rates than thick layers with the same optical thickness. Future tests of FSCK model treatment of clouds should examine how the FSCK model-calculated heating rates compare to those of other models as the vertical resolution of cloud layers

changes.

We also saw in Section 4.1 that the LBL in-cloud heating rates increased by 1.5–2.5% when the near-infrared spectral interval was extended from 4.6  $\mu\text{m}$  to 5.0  $\mu\text{m}$ . This increase in the heating rate is a result of strong cloud absorption in the spectral range 4.6–5.0  $\mu\text{m}$ , even though this spectral interval contains only 0.1% of the total solar incident irradiance. Consequently, future development of the FSCK method should extend the solar spectral interval farther into the near-infrared.

In addition to the shortwave version of the FSCK approach developed in this work, the full formulation of the FSCK method of Modest (2003) presented in Chapter 2.1.2 describes a model that can be used for longwave atmospheric radiative transfer. Such a longwave model is in the planning stage. Most likely, a longwave implementation of the FSCK method will compare as favorably to operational and research longwave models as the shortwave version has compared to state-of-the-art shortwave models in terms of accuracy and efficiency.

As with the state-of-the-art shortwave models, there are a variety of methods used in longwave models. Fast techniques that rely heavily on empirical methods include, for example, the Dudhia longwave model (Dudhia 1989) and the GFDL-Eta longwave model (Fels and Schwarzkopf 1975; Schwarzkopf and Fels 1991). Implementations of the correlated  $k$ -distribution approach include that of Fu and Liou (1992), which uses 67 quadrature points over 12 spectral intervals, and the longwave version of RRTM (Mlawer et al. 1997; Mlawer and Clough 1997;

Mlawer and Clough 1998), which uses 240 quadrature points over 15 spectral intervals. We anticipate that the FSCK approach can achieve similar or more accurate heating rates across the longwave spectrum with significantly fewer calculations than existing correlated  $k$ -distribution methods, but this remains to be demonstrated.

# Bibliography

- Barker, H. W. and 31 coauthors, 2003: Assessing 1d atmospheric solar radiative transfer models: interpretation and handling of unresolved clouds. *J. Climate*, **16**, 2676–2699.
- Briegleb, B. P., 1992: Delta-Eddington approximation for solar radiation in the NCAR community climate model. *J. Geophys. Res.*, **97**, 7603–7612.
- Burch, D. E., D. Gryvnak, and D. Williams, 1960: The infrared absorption by carbon dioxide. Rept. on Project 778, Ohio State University Research Foundation, 88pp.
- Clough, S. A. and M. J. Iacono, 1995: Line-by-line calculation of atmospheric fluxes and cooling rates, 2, application to carbon dioxide, ozone, methane, nitrous oxide, and the halocarbons. *J. Geophys. Res.*, **100**(10), 16,519–16,535.
- Clough, S. A., M. J. Iacono, and J.-L. Moncet, 1992: Line-by-line calculation of atmospheric fluxes and cooling rates: Application to water vapor. *J. Geophys. Res.*, **97**(15), 15,761–15,785.
- Clough, S. A., F. X. Kneizys, and R. W. Davies, 1989: Line shape and the water vapor continuum. *Atmos. Res.*, **23**, 229–241.
- Collins, W. D., 1998: A global signature of enhanced shortwave absorption by clouds. *J. Geophys. Res.*, **103**(D24), 31,669–31,679.
- Collins, W. D., J. M. Lee-Taylor, D. P. Edwards, and G. L. Francis, 2004: Effects of increased near-infrared absorption by water vapor on the climate system. In preparation.
- Dudhia, J., 1989: Numerical study of convection observed during the winter monsoon experiment using a mesoscale two-dimensional model. *J. Atmos. Sci.*, **46**, 3077–3107.
- Evans, K. F., 1998: The spherical harmonic discrete ordinate method for three-dimensional atmospheric radiative transfer. *J. Atmos. Sci.*, **55**, 429–446.

- Fels, S. B. and M. D. Schwarzkopf, 1975: The simplified exchange approximation: A new method for radiative transfer calculations. *J. Atmos. Sci.*, **32**, 1475–1488.
- Fröhlich, C. and G. E. Shaw, 1980: New determination of Rayleigh scattering in the terrestrial atmosphere. *Appl. Opt.*, **19**, 1773–1775.
- Fu, Q. and K. N. Liou, 1992: On the correlated  $k$ -distribution method for radiative transfer in non-homogeneous atmospheres. *J. Atmos. Sci.*, **49**(22), 2139–2156.
- Goody, R. M. and Y. L. Yung, 1989: *Atmospheric Radiation - Theoretical Basis*. Oxford University Press, New York, 2nd ed edition.
- Grell, G., J. Dudhia, and D. Stauffer, 1994: A description of the Fifth-Generation Penn State/NCAR Mesoscale Model (MM5). Technical Note NCAR/TN-398+STR, NCAR.
- Hottel, H. C. and A. F. Sarofim, 1967: *Radiative Transfer*. McGraw-Hill, New York.
- Howard, J. N., D. E. Burch, and D. Williams, 1956: Infrared transmission of synthetic atmospheres, Parts I-V. *J. Opt. Soc. Amer.*, **46**, 186–190, 237–241, 242–245, 334–338, 452–455.
- Kato, S., T. P. Ackerman, J. H. Mather, and E. E. Clothiaux, 1999: The  $k$ -distribution method and correlated- $k$  approximation for a shortwave radiative transfer model. *JQSRT*, **62**, 109–121.
- Kiehl, J. T., C. Brühl, and T. Yamanouchi, 1985: A parameterization for the absorption due to the near infrared bands of  $\text{CO}_2$ . *Tellus*, **37**(B), 189–196.
- King, J. I. F. and P. R. Gast, 1961: *Handbook of geophysics*. Macmillan, New York. chap. 16, 32 pp.
- Kurucz, R. L., 1992: *Synthetic infrared spectra, in infrared solar physics*. IAU Symp. 154. Kluwer, Acad., Norwell, MA.
- Kurucz, R. L., 1994: The solar irradiance by computation. In *Proceedings of the 17th annual review conference on atmospheric transmission models*, GFDL.
- Labs, D. and H. Neckel, 1968: The radiation of the solar photosphere from 200Å to 100 $\mu$ . *Z. Astrophys.*, **69**, 1–73.
- Lacis, A. A. and J. E. Hansen, 1974: A parameterization for the absorption of solar radiation in the earth's atmosphere. *J. Atmos. Sci.*, **31**, 118–133.

- Lacis, A. A. and V. Oinas, 1991: A description of the correlated  $k$  distribution method for modeling nongray gaseous absorption, thermal emission, and multiple scattering in vertically inhomogeneous atmospheres. *J. Geophys. Res.*, **96**(D5), 9,027–9,063.
- Lenoble, J., 1993: *Atmospheric radiative transfer*. A. Deepak Pub., Hampton VA.
- Liou, K. N., 2002: *An introduction to atmospheric radiation*. International Geophysics Series, Volume 84. Academic Press, 2nd ed. edition. 583 pp.
- McClatchey, R. A., R. W. Fenn, J. E. A. Selby, F. E. Volz, and J. S. Garing, 1972: Optical properties of the atmosphere, 3rd ed. Technical Report AFCRL-72-0497, AFCRL. 108 pp. [NTIS N7318412].
- Michalakes, J., S. Chen, J. Dudhia, L. Hart, J. Klemp, J. Middlecoff, and W. Skamarock, 2001: Development of a next generation regional weather research and forecast model. In *Developments in Teracomputing: Proceedings of the Ninth ECMWF Workshop on the Use of High Performance Computing in Meteorology*, Zwiefelhofer, W. and Kreitz., N., editors, World Scientific, Singapore., 269-276.
- Mlawer, E. J. and S. A. Clough, 1997: On the extension of rapid radiative transfer model to the shortwave region. In *Proceedings of the 6th Atmospheric Radiation Measurement (ARM) Science Team Meeting*, U.S. Department of Energy. CONF-9603149.
- Mlawer, E. J. and S. A. Clough, 1998: Shortwave and longwave enhancements in the rapid radiative transfer model. In *Proceedings of the 7th Atmospheric Radiation Measurement (ARM) Science Team Meeting*, U.S. Department of Energy. CONF-970365.
- Mlawer, E. J., S. J. Taubman, P. D. Brown, M. J. Iacono, and S. A. Clough, 1997: Radiative Transfer for inhomogeneous atmospheres: RRTM, a validated correlated- $k$  model for the longwave. *J. Geophys. Res.*, **102**(D14), 16,663–16,682.
- Modest, M. F., 1991: The weighted-sum-of-gray-gases model for arbitrary solution methods in radiative transfer. *ASME J. Heat Transfer*, **113**(3), 650–656.
- Modest, M. F., 2003: Narrow-band and full-spectrum  $k$ -distributions for radiative heat transfer—correlated- $k$  vs. scaling approximation. *JQSRT*, **76**(1), 69–83.
- Modest, M. F. and R. J. Riazzi, 2004: Assembly of full-spectrum  $k$ -distributions from a narrow-band database; effects of mixing gases, gases and nongray absorbing particles, and mixtures with nongray scatterers in nongray enclosures. *JQSRT*, **88**. In print.

- Modest, M. F. and H. Zhang, 2002: The full-spectrum correlated  $k$ -distribution for thermal radiation from molecular gas-particulate mixtures. *ASME J. Heat Transfer*, **124**(1), 30–38.
- Ramaswamy, V. and S. M. Freidenreich, 1991: Slar radiative line-by-line determination of water vapor absorption and water cloud extinction in inhomogeneous atmospheres. *J. Geophys. Res.*, **96**, 9133–9157.
- Roberts, R. E., J. E. A. Selby, and L. M. Biberman, 1976: Infrared continuum absorption by atmospheric water vapor in the 8-12  $\mu\text{m}$  window. *Appl. Opt.*, **15**, 2085–2090.
- Rothman, L. S. and 31 coauthors, 2003: The HITRAN molecular spectroscopic database: Edition of 2000 including updates of 2001. *JQSRT*. In press.
- Rothman, L. S., C. P. Rinsland, A. Goldman, S. T. Massie, D. P. Edwards, J. M. Flaud, A. Perrin, C. Camy-Peyret, V. Dana, J. Y. Mandin, J. Schroeder, A. McCann, R. R. Gamache, R. B. Watson, K. Yoshino, K. V. Chance, K. W. Jucks, L. R. Brown, V. Nemtchinov, and P. Varanasi, 1998: The HITRAN molecular spectroscopic database and HAWKS (HITRAN Atmospheric Workstation): 1996 edition. *JQSRT*, **60**(5), 665–710.
- Sasamori, T., J. London, and D. V. Hoyt, 1972: Radiation budget of the Southern Hemisphere. *Meteor. Monogr.*, **13**(35), 9–23.
- Schwarzkopf, M. D. and S. B. Fels, 1991: The simplified exchange method revisited: An accurate, rapid method for computation of infrared cooling rates and fluxes. *J. Geophys. Res.*, **96**, No. D5, 9075–9096.
- Slingo, A., 1989: A GCM parameterization for the shortwave radiative properties of water clouds. *J. Atmos. Sci.*, **46**, 1419–1427.
- Stephens, G. L., 1978: Radiation profiles in extended water clouds. II: Parameterization schemes. *J. Atmos. Sci.*, **35**, 2123–2132.
- Taine, J. and A. Soufiani, 1999: *Gas IR radiative properties: From spectroscopic data to approximate models*. Advances in Heat Transfer, 33. Academic Press, New York. 295-414.
- Teillet, P. M., 1990: Rayleigh optical depth comparisons from various sources. *Appl. Opt.*, **29**(13), 1897–1900.
- Toon, O. B. and T. Ackerman, 1981: Algorithms for the calculation of scattering by stratified spheres. *Appl. Opt.*, **20**, 3657–3660.

- Wang, A. and M. F. Modest, 2004: High-accuracy, compact database of narrow-band  $k$ -distributions for water vapor and carbon dioxide. In *Proceedings of the ICHMT 4th International Symposium on Radiative Transfer*, Mengüç, M. P. and Selçuk, N., editors, Istanbul, Turkey.
- World Climate Research Programme, 1984: Scientific Plan: Report of the WMO ICSU Joint Scientific Committee. *WCRP Publication Series 2*, WMO. 95 pp.
- Yamamoto, G., 1962: Direct absorption of solar radiation by atmospheric water vapor, carbon dioxide and molecular oxygen. *J. Atmos. Sci.*, **19**, 182–188.
- Zdunkowski, W. G., W.-G. Panhans, R. M. Welch, and G. J. Korb, 1982: A radiation scheme for circulation and climate models. *Contrib. Atmos. Phys.*, **55**, 215–238.

## Vita Daniel T. Pawlak

Captain Dan Pawlak was born in Buffalo, NY. He graduated from Kenmore West High School in 1984 and enlisted in the U. S. Air Force.

After serving ten years as an enlisted meteorologist, Captain Pawlak was selected for the Airman's Education and Commissioning Program and was commissioned through Officer Training School at Maxwell AFB. As a weather officer he has supported the 2d Armored Cavalry Regiment and the Joint Readiness Training Center at Ft Polk, LA, and expanded the Air Force Weather Agency's ability to support worldwide operations through the enhancement of the MM5 forecast model system.

Prior to his assignment to Penn State, Captain Pawlak was the Commander of Detachment 1, 607th Weather Squadron, and was responsible for weather support for all 2d Infantry Division operations along the Korean Demilitarized Zone.

Captain Pawlak and his wife have two children.

### EDUCATION:

1991 Associate of Applied Science, Weather Technology, Community College of the Air Force

1994 Bachelor of Science degree, Florida State University, Meteorology with Honors in Meteorology (AECF)

1998 Master of Science degree, Pennsylvania State University, Meteorology (Numerical Weather Prediction) (AFIT)

### PUBLICATIONS:

D. R. Stauffer, M. J. Otte, D. T. Pawlak and J. C. Wyngaard, 1998: A new spectral boundarylayer parameterization for the MM5: Coupling methodology and performance evaluations., In Proceedings of the 12th conference on numerical weather prediction, AMS.

Pawlak, D. T., 1998: Development and evaluation of a new spectral planetary boundarylayer architecture for the MM5. M.S. Thesis, The Pennsylvania State University, 102 pp.

Pawlak, D. T., E. E. Clothiaux, M. F. Modest, and J. N. S. Cole, 2004: Full spectrum correlated k distribution for shortwave atmospheric radiative transfer. J. Atmos. Sci., In press.